Thesis [XX/2015]

**Dissertation under joint supervision with European Doctorate
Certificate of the requirements for the degrees of:**

DOCTEUR DE L'UNIVERSITÉ DE LIMOGES

Spécialité: Matériaux Céramiques et Traitements de Surface

and

DOTTORE DI RICERCA IN FISICA

**della Scuola di Dottorato Scienze e Tecnologie per l'Informazione e la
Conoscenza (XXVI ciclo)**

presented and defended by

Aleena Maria LAGANAPAN

November 26, 2015

Rheology and structure of ceramic suspensions under constraints: a computational study

Thesis supervisors:

Arnaud Videcoq, Riccardo Ferrando and Marguerite Bienia

COMMITTEE :

Tapio ALA-NISSILA	Professor, Aalto University	Reviewer
Paul BOWEN	Professor, École Polytechnique Fédérale de Lausanne	Reviewer
Christophe MARTIN	Directeur de Recherche CNRS (HDR), Université de Grenoble Alpes	Examiner
Riccardo FERRANDO	Professor, Universita degli Studi di Genova	Examiner
Arnaud VIDECOQ	Maître de Conférence (HDR), SPCTS	Examiner
Marguerite BIENIA	Maître de Conférence, SPCTS	Examiner

Contents

Nomenclature

Nomenclature

α	Rotation angle
Δt_{BD}	Time step for BD simulations
Δt_{LB}	Time step for LB simulations
Δt_{MD}	Time step for MD simulations
Δt_{SRD}	Time step for SRD simulations
Δv_y	Shear velocity
δ_{ij}	Kronecker delta.
$\dot{\gamma}$	Shear rate
ϵ_{Wall}	Interaction parameter for LJ 9-3 potential
ϵ_{wall}	Interaction parameter between the wall and the fluid particles
ϵ_{cc}	Interaction parameter between the colloids
ϵ_{cf}	Interaction parameter between the colloids and the fluid
η	Viscosity of water ($10^{-3}\,\mathrm{Pa\cdot s}$)
γ	Average number of fluid particles in each cell
$\hat{r}_{ij}$	Unit vector in the direction of $\mathbf{r}_{ij}$
λ	Dimensionless mean free path
$\mathcal{T}$	Instantaneous temperature
ν	Kinematic viscosity
ϕ_c	Percolation threshold
ϕ_{max}	Maximum packing fraction
ρ_f	Mass density of the SRD fluid
σ_{Wall}	Interaction parameter for LJ 9-3 potential
σ_{wall}	Interaction parameter between the wall and the fluid particles
σ_{cc}	Interaction potential between the colloids
σ_{cf}	Interaction potential between the colloids and the fluid
τ	Yield stress
τ_B	Brownian relaxation time
τ_D	Colloid diffusion time

τ_f	Fluid relaxation time
τ_ν	Kinematic time
τ_{FP}	Fokker-Planck time
$\varepsilon_{\text{Wall}}$	Attraction strength between the colloids and the wall
ς	Strength of stochastic forces in DPD simulations
ζ	Friction coefficient of the solvent
ζ_E	Enskog friction coefficient
ζ_S	Stokes friction coefficient
A	Acceptance probability in the Monte-Carlo thermostat
a	Colloid radius
a_0	cell size
B_{ij}	Parameter for the hard-wall potential
c	Thermostat strength
C_{ij}	Parameter for the hard-wall potential
D_0	Diffusion coefficient of an isolated colloid
D_{SRD}	Diffusion coefficient in the SRD simulations
D_{ij}	Parameter for the hard-wall potential
I	Identity tensor
k_B	Boltzmann constant
L	Side length of the simulation box
l	Dimension of the simulation box in terms of the number of cells
M	Mass of the colloid
m_1	Yield stress factor
N_A	Number of aggregates
N_c	Number of embedded colloids
N_f	Number of fluid particles in a simulation box
$n_i(\mathbf{r}, t)$	Represents the fluid density in LB simulations
$n_i^{eq}(\mathbf{r}, t)$	Represents the equilibrium value of the fluid density in LB simulations

P_{2D}	Structural parameter that determines between NaCl and CsCl lattice types
P_{3D}	Structural parameter that determines between NaCl and CsCl lattice types
r_{cc}	Cut-off radius in the colloid-colloid interaction
r_{cf}	Cut-off radius in the colloid-fluid interactions
S	Thermostat scaling factor
T	Average temperature of the system
T_0	Reference temperature
T_{SRD}	Average temperature of the system in SRD simulations
t_{SRD}	SRD time scale
U_{Wall}	Potential describing the attractive wall
U_{cc}	Interaction potential between the colloids
U_{cf}	Interaction potential between the colloids and the fluid
U_{ij}^{HW}	Hard-wall potential
V	Volume of the simulation box
V_f	Free volume accessible to the fluid particles inside the simulation box
V_{wf}	Interaction potential between the wall and the fluid particles
Y_i	Uncorrelated Gaussian variables used in BD simulations.
Z	Colloid charge
$\mathbf{\Gamma}_i(t)$	Represents the random forces received by the colloids from the fluid in a BD simulation
$\mathbf{\Xi}_i(t)$	Represents the frictional forces in a BD simulation
$\mathbf{a}_i$	Acceleration of the ith particle
$\mathbf{c}_i$	Represents the velocity of the lattice sites in LB simulations
$\mathbf{D}_{ij}$	Diffusion tensor used in BD-YRP
$\mathbf{F}_{ij}^c$	Represents interparticle forces in DPD simulations
$\mathbf{F}_{ij}^d$	Represents the velocity-dependent forces in DPD simulations
$\mathbf{F}_{ij}^f$	Represents the stochastic forces in DPD simulations
$\mathbf{F}_i$	Total force between particles i and j
$\mathbf{R}$	Rotation matrix

$\mathbf{r}_i$ Position of the ith particle

$\mathbf{v}_i$ Velocity of the ith particle

$\mathbf{v}_{\text{cm}}$ Center of mass velocity inside the simulation box

U_{ij} Interaction potential between particles i and j

HIs   Hydrodynamic interactions

IP   Inverse power potential

LEBC   Lees Edwards boundary conditions

$\mathbf{r}_i$ Position of the ith particle

$\mathbf{v}_i$ Velocity of the ith particle

U_{ij} Interaction potential between particles i and j

List of Figures

List of Tables

Summary

The numerical study of colloidal suspensions is an integral part of several ceramic and biological processes. The main challenge of this thesis is to understand and predict the structural and rheological behaviours of the colloids when complexities such as (1) hydrodynamic interactions (HIs) and (2) external forces are incorporated in the system. These factors are difficult to model because of the disparity in size between the colloids and the fluid particles. Hence there is a clear separation of length and time scales between the physics of the colloids and the fluid.

A convenient way to address this problem is to average-out the effects of the fluid so that the modeling of the colloidal suspension is more maneagable. In this regard, this thesis employs two of the fastest numerical techniques available in literature: standard Brownian Dynamics (BD), for systems where HIs can be ignored; and hybrid Stochastic Rotation Dynamics - Molecular Dynamics (SRD-MD), for systems where HIs need to be incorporated. The two types of external forces explored in this thesis are shear and attractive walls. Suspensions under shear are simulated using SRD-MD, while the system with attractive walls is simulated using BD. BD and SRD-MD are also simultaneously applied when the effects of HIs need to be isolated and analyzed.

We study three different systems of colloidal suspensions. The first is a system of hard spheres under shear, where we verify that the modeling of HIs in SRD-MD can accurately reproduce the relation between shear viscosity and volume fraction. Since SRD-MD is a relatively recent technique, its potential as a simulation method is not yet fully-explored. We develop SRD-MD by incorporating shear, with a Monte-Carlo thermostat, in MD-coupled sytems. From this model, we can apply the non-equilibrium approach for the calculation of shear and derive a stress tensor for dilute and concentrated systems. The shear viscosity results are in agreement with known analytical, numerical and experimental data. We also show that the shear viscosity of the suspension can be divided into components: one is shear viscosity contributions from the fluid and colloid components; and the other is shear viscosity contributions from the streaming and collisional components. Hence our method of calculation allows for a more in-depth characterization of the viscosity of the suspension. In this study, we establish that SRD-MD fully captures the required hydrodynamic effects in sheared suspensions thus making SRD-MD a valuable tool for modeling an interesting range of systems under shear.

The second system consists of aqueaous alumina suspensions described by the Derjaguin-Landau-Verwey-Overbeek (DLVO) potential. We analyze the percolation behaviour of the system by employing BD and SRD-MD methods. The percolation phenomenon is characterized by the formation of an infinite network of colloidal aggregates that spans through space. The parameters that influence the percolation threshold (ϕ_c)

are colloid-colloid attraction strength and HIs. The simulations show that ϕ_c decreases with increasing colloid-colloid attraction strength since this can lead to more elongated structures. Moreover, we observe that systems with HIs tend to have more elongated structures during the aggregation process than systems without HIs. This results to a sizable decrease in ϕ_c when the colloid-colloid attraction is not too strong. On the other hand, the effects of HIs tend to become negligible with increasing attraction strength. Our ϕ_c values are in good agreement with those estimated by the yield stress model (YODEL) by Flatt and Bowen. This work can be useful, alongside YODEL, in predicting the yield stress magnitude of ceramic materials.

The third sytem consists of binary colloids described by a Yukawa potential. The binary system is placed under the influence of an attractive wall that is described by a Lennard Jones 9-3 potential. We evolve the system using BD and demonstrate that the presence of an attractive wall can modify the expected equilibrium structures of the colloids. In particular, the attractive wall can alter the lattice structure of the aggregates on the surface such that CsCl-type lattices are formed instead of metastable NaCl-type lattices. We also examine the parameters that lead to this kind of lattice transformation: the colloid-wall attraction strength ($\varepsilon_{\text{Wall}}$), the colloid-colloid attraction strength (U_0), and the inverse range of interaction (κa). The variables κ and a denote the inverse of Debye screening length and the radius of the colloids respectively, and the values of κa are restricted in the following range: $\kappa a \in [1, 3]$. The results show that the probability of obtaining a CsCl structure increases when the force of attraction from the wall exceeds the inter-colloid attraction ($\varepsilon_{\text{Wall}} > U_0$). In addition to this, the likelihood of obtaining CsCl increases and when κa is relatively small (longer range of repulsion). Consequently, for systems with $\varepsilon_{\text{Wall}} < U_0$, the aggregates tend to remain as NaCl. The reason why CsCl structure is more favored is because it has a more compact formation at the surface. Moreover, the total energy, between the colloidal structure and the surface, is smaller in the CsCl-cases than in the NaCl-cases. This study can have implications on researches that invlove surface-grown ceramics and protein adsorption.

Finally, we perform preliminary investigations on shaken suspensions by SRD-MD. The system is the same as the percolating alumina system described above. The difference is that the colloidal suspension is now placed under an oscillating shear with a shear rate of 10 s^{-1} and a frequency of 20 s^{-1}. We demonstrate that when the oscillating motion of the suspension occurs simultaneously with the aggregation process of the colloids, more compact structures are formed. Moreover, it seems that the suspensions undergoing oscillatory motion reorganize at a faster rate than suspensions in equilibrium. This technique of agitating the suspensions can be used to artificially manipulate the dissociation and association rates of the colloids thus promoting more ordered structures.

Résumé

L'étude numérique des suspensions colloïdales fait partie intégrante de différents procédés céramiques et biologiques. L'enjeu principal de cette thèse est de comprendre et prédire les propriétés structurales et rhéologiques de suspensions colloïdales en tenant compte d'éléments complexes tels que (1) les interactions hydrodynamiques (IHs) et/ou (2) des forces extérieures. La simulation numérique d'une suspension colloïdale est difficile du fait des tailles très différentes des colloïdes et des molécules de liquide. Il y a par conséquent une séparation importante entre les échelles de longueur et de temps associées à la physique des colloïdes et à la physique du fluide.

Un moyen de parvenir à simuler une suspension colloïdale est de moyenner les effets du fluide. De ce point de vue, nous employons dans cette thèse deux des techniques numériques les plus rapides de la littérature: la dynamique brownienne standart (BD), pour les systèmes où les IHs peuvent être ignorées; et la technique hybride "stochastic rotatoin dynamics - molecular dynamics" (SRD-MD), pour les systèmes où les IHs doivent être incorporées. Les deux types de forces extérieures explorées dans cette thèse sont le cisaillement et la présence d'un mur attractif. Les suspensions soumises au cisaillement sont simulées par SRD-MD, alors que le système avec le mur attractif est simulé par BD. BD et SRD-MD sont aussi employées simultanément lorsqu'il s'agit d'isoler et d'analyser les effets des IHs.

Trois systèmes colloïdaux différents ont été étudiés. Le premier est un système de sphères dures soumis à un cisaillement, où le but a été de vérifier que l'introduction des IHs dans la SRD-MD peut correctement reproduire la relation entre la viscosité et la fraction volumique. Du fait que la SRD-MD est une technique relativement récente, son potentiel en tant que méthode de simulation n'est pas encore totalement exploré. Nous avons développé la SRD-MD en incorporant le cisaillement, avec un thermostat Monte-Carlo. Nous avons appliqué l'approche hors équilibre pour le calcul du cisaillement et dérivé un tenseur des contraintes pour les systèmes dilués et concentrés. Les résultats de viscosité sont en accord avec les résultats connus, qu'ils soient analytiques, numériques et expérimentaux. Nous montrons également que la viscosité de la suspension peut-être décomposée en différentes contributions: celles du fluide et des colloïdes; puis celles des étapes d'écoulement et des collisions. Cette étude permet donc une caractérisation détaillée de la viscosité des suspensions, où nous montrons que la SRD-MD décrit bien les effets hydrodynamiques dans les suspensions cisaillées, ce qui en fait un outil intéressant pour simuler les systèmes sous cisaillement.

Le second système consiste en une suspension d'alumine, pour laquelle les interactions sont décrites par la théorie DLVO (Derjaguin-Landau-Verwey-Overbeek). Une étude de la percolation a été réalisée par les méthodes BD et SRD-MD. La percolation est caractérisée

par la formation d'un réseau d'agrégats qui traverse la boîte de simulation d'un bout à l'autre. Les paramètres dont nous avons étudié les effets sur le seuil de percolation (ϕ_c) sont la profondeur du puits de potentiel caractérisant l'attraction entre les colloïdes et les IHs. Les simulations montrent que ϕ_c diminue lorsque la profondeur du puits de potentiel augmente, car les agrégats formés sont plus allongées. De plus, nous observons que la prise en compte des IHs tend à former des structures plus allongées également, par rapport aux structures obtenues sans les IHs. Ceci se traduit par une diminution de ϕ_c lorsque le puits de potentiel n'est pas trop profond. D'autre part, l'effet des IHs devient négligeable lorsque la profondeur du puits de potentiel augmente. Les valeurs de ϕ_c obtenues dans les simulations sont en bon accord avec celles estimées par le modèle de la contrainte seuil (YODEL) établi par Flatt et Bowen. Ce travail peut être utile, de façon complémentaire à YODEL, pour prédire la contrainte seuil de suspensions céramiques.

Le troisième système comporte deux types de colloïdes qui interagissent par un potentiel de Yukawa. Ce système binaire est soumis à l'influence d'un mur attractif dont l'interaction avec les colloïdes est décrite par un potentiel de Lennard-Jones 9-3. L'agrégation des colloïdes dans ce système est simulée par BD et nous montrons que la présence d'un mur attractif peut modifier les structures d'équilibre attendues. En particulier, le mur attractif peut altérer la structure cristalline des agrégats à la surface telle qu'une structure de type CsCl qui se forme au lieu de la structure métastable de type NaCl. Nous avons étudié les paramètres qui conduisent à ce type de changement de configuration: la profondeur du puits de potentiel colloïde-mur (ϵ_{Wall}), celle du puits de potentiel colloïde-colloïde (U_0), et l'inverse de la portée des interactions colloïde-colloïde (κa). Les variables κ et a sont respectivement l'inverse de la longueur d'écrantage de Debye et le rayon des colloïdes. Le domaine de variation de κa étudié ici est: $\kappa a \in [1, 3]$. Les résultats montrent que la probabilité d'obtenir une structure CsCl augmente quand l'attraction colloïde-mur excède l'attraction colloïde-colloïde ($\epsilon_{Wall} > U_0$). De plus, la tendance à la formation de la structure CsCl augmente lorsque κa est relativement faible (interactions colloïde-colloïde de plus longue portée). En conséquence, pour les systèmes où $\epsilon_{Wall} < U_0$, les agrégats tendent à rester dans la structure NaCl. La raison pour laquelle la structure CsCl est plus favorable vient du fait qu'elle est plus compacte à la surface. L'énergie totale, entre la structure colloïdale et la surface est plus faible dans le cas d'une structure CsCl que dans le cas d'une structure NaCl. Cette étude montre l'importance des interactions avec les parois environnantes sur les structures colloïdales qui peuvent se former.

Finalement, nous avons réalisé une étude préliminaire par SRD-MD de suspensions soumises à un cisaillement oscillant. Le système est le même que celui de l'étude sur la percolation. Le taux de cisaillement est de 10 s^{-1} et la fréquence de 20 s^{-1}. Nous montrons que lorsque la suspension est soumise au cisaillement oscillant en même temps que

l'agrégation se produit, des structures plus compactes se forment. Il semble que dans les suspensions soumises au cisaillement oscillant les colloïdes se réorganisent plus rapidement que dans les suspensions à l'équilibre. Cette technique d'agitation des suspensions pourrait être utilisée pour modifier artificiellement les taux d'association-dissociation des colloïdes pour favoriser la formation de structures plus ordonnées.

Riassunto

Lo studio numerico delle sospensioni colloidali è molto importante in numerosi campi della fisica, della chimica e della scienza dei materiali. In particolare, le sospensioni colloidali hanno un ruolo sempre più importante nei processi relativi alla formazione dei materiali ceramici.

Lo scopo principale di questa tesi è quello di capire e prevedere i comportamenti strutturali e reologici delle sospensioni colloidali tenendo conto di fattori complessi quali gli effetti idrodinamici e/o di campi di forze esterni applicati ai colloidi. Questi fattori sono difficili da studiare dal punto di vista teorico/computazionale, principalmente a causa delle grandi differenze di taglia fra i colloidi e le molecole del solvente, che si riflettono anche in grandi differenze fra le scale di tempi caratteristiche dei loro moti. Questo impedisce la simulazione atomistica delle sospensioni colloidali, in quanto si dovrebbe tenere in conto esplicitamente di un numero enorme di gradi di libertà.

D'altra parte la separazione di scale di lunghezza e di tempi permette lo sviluppo di modelli di tipo "coarse grained", in cui vengono introdotti gradi di libertà efficaci che raggruppano un grande numero di gradi di libertà microscopici. Il modello più semplice di questo tipo è la dinamica Browniana, in cui il solvente diviene un continuo indifferenziato che fornisce una forza viscosa proporzionale alla velocità dei colloidi e un rumore bianco dovuto agli urti delle molecole di solvente sui colloidi. La dinamica Browniana non tiene conto del trasferimento di quantità di moto fra colloidi e solvente e quindi trascura completamente gli effetti idrodinamici. Un vantaggio della dinamica Browniana è costituito dalla semplicità e velocità nel calcolo numerico, che permette di esplorare scale di tempi assai lunghe anche per sistemi contenenti centinaia di colloidi.

In questa Tesi, la dinamica Browniana è usata per simulare l'aggregazione di colloidi binari (che portano cariche opposte) in presenza di una parete attrattiva. Queste simulazioni necessitano di scale di tempi molto lunghe e di un gran numero di colloidi e quindi la dinamica Browniana è l'unica che ne consente uno studio appropriato. In questa tesi si dimostra che la presenza della parete induce la formazione di cristalli colloidali con la struttura del cloruro di cesio in molti casi in cui l'aggregazione lontano dalla parete darebbe strutture del tipo del cloruro di sodio.

In molti casi, l'approssimazione di trascurare gli effetti idrodinamici non è appropriata. Ad esempio, nello studio della dipendenza della viscosità della sospensione al variare della frazione volumica occupata dai colloidi, le interazioni fra collodi e solvente indotte dagli effetti idrodinamici sono molto importanti. Questi effetti idrodinamici sono stati studiati per mezzo di una tecnica simulativa ibrida, la Stochastic Rotation Dynamics - Molecular Dynamics (SRD-MD). In questa tecnica, il solvente è trattato esplicitamente introducendo particelle efficaci che hanno massa molto più grande di quella delle molecole di solvente,

ma massa molto più piccola di quella dei colloidi. Il calcolo della viscosità con la SRD-MD ha richiesto lo sviluppo di una metodologia originale, che ha permesso di calcolare la viscosità di una sospensione contenente colloidi di tipo simile alla sfera dura fino a densità elevate, in ottimo accordo con precedenti risultati analitici e simulativi. Questo lavoro ha dimostrato che la SRD-MD può essere la tecnica più efficiente per il calcolo della viscosità in sistemi con interazioni idrodinamiche.

La SRD-MD è stata usata anche per simulare sospensioni sottoposte a scuotimento, al fine di verificare se questo tipo di procedura può portare alla formazione di aggragati più compatti.

Infine, SRD-MD e dinamica Browniana sono state utilizzate per studiare la percolazione nella aggregazione in sospensioni acquose di allumina. Il confronto delle due tecniche ha permesso di determinare l'influenza dell'idrodinamica sulle soglie di percolazione. Si è dimostrato che gli effetti idrodinamici sono piè importanti quando l'attrazione fra i colloidi è relativamente debole, mentre divengono trascurabili per forti attrazioni che sopprimono i riarrangiamenti interni agli aggregati. Quando le forse attrattive non sono troppo forti, gli effetti idrodinamici velocizzano l'aggregazione e rallentano il riarrangiamento interno agli aggregati, causando la formazione di aggregati meno compatti e l'abbassamento della soglia di percolazione.

Introduction

Significance of this study

Colloidal suspensions are integral to ceramic processing. In fact, most modern ceramic processing techniques follow a colloidal route: from coagulation casting and gel casting [11]; to solid free form fabrication such as fused deposition [12], robocasting [13], stereolithography [14] and 3-D printing [15]. The high potential to yield reliable products through careful control over the evolution process of ceramics is the main motivation for employing a colloid-based approach. Aside from ceramic science, colloidal suspensions are also widely studied because they exhibit the same phase behavior as atoms and molecules with the advantage of the direct space observation [16].

Over the years, significant achievements have been made in this field. Much is owed to the well-known DLVO theory, developed by Derjaguin and Landau [17] and Verwey and Overbeek [18], which have laid the ground work for modern colloidal science [19]. The realization that the interparticle potential can be tailored to achieve the desired stability has been beneficial to an extensive array of technical applications [20]. Material defects are also minimized, if not eliminated, since most detrimental heterogeneities such as inhomogeneous phase distribution, presence of large agglomerates and contaminants, are derived from the properties of the suspension itself and can be corrected correspondingly [21, 22].

However, the fine tuning of the interparticle potential is just the first step. Due to the demand for new and more sophisticated materials, special attention is devoted to the evolution of colloidal suspensions. In particular, the ability to predict the structure and rheology directly from interparticle forces and perturbations is not yet fully developed [19]. For example, the effects of shearing forces on the structure and flow behavior of suspensions still require a profound understanding. Moreover, the study on the physical and chemical mechanisms that dictate phase transformations [16], crystallization and gelation [23] of colloids is still an active field.

Because there are certain limitations in experimental and analytical approaches, especially for sheared and dense suspensions, simulations play an increasingly important role in the study of colloidal suspensions. Numerical methods can be used to isolate and analyze the effects of microstructure, composition, geometry and external perturbation that otherwise cannot be accessed by standard experiments [24]. Simulations can also offer a more viable way to introduce perturbations in systems, an undertaking that can be laborious via analytical approaches [20]. While numerical studies have brought significant contributions to our understanding of flow behavior and dynamics of colloidal suspensions, the quantitative prediction of rheological coefficients from a microscopic standpoint remains an arduous task. Clearly, there is a huge demand for better models and characterization tools that can properly examine the underlying dynamics that dictates

the behavior of colloidal suspensions.

The challenges that need to be addressed are as follows. The first challenge is the separation of time and length scales. A characteristic feature of colloidal suspensions is that they belong to a class of complex fluids where the phenomena of interest occur on a mesoscopic scale but are derived from molecular-level information. This hierarchy of time and length scales introduces mathematical complexities so that analytical models are limited to highly idealized and simplified systems. Moreover, while the typically used temporal (order of milliseconds) and spatial (micrometers) observables can be measured, probing other smaller, yet equally relevant time and length scales is seldom experimentally feasible.

The second challenge is the many-body nature of these interactions. A unifying theory on the collective many-body effects induced by the interaction between the particles is still lacking. Specifically, one needs a more in-depth understanding of the influence of *hydrodynamic interactions* (HIs) on the rheological properties of colloidal suspensions.

Finally, confining geometries and outside forces have to be factored in. In this work, these are represented by attractive walls and mechanical shear. In reality, colloidal suspensions are always exposed to environmental constraints. In fact, the presence of external perturbations in nature is so pervasive that it is not an exception but a rule. A working knowledge of their effects can serve as foundations for new theories and can be used to design the properties of new materials.

Due to the complexity of the system and the problem, it is not surprising that colloidal suspensions have been extensively analyzed by numerical models. The contribution of numerical methods to the understanding of complex sytems is substantial. Simulations have answered problems in statistical mechanics that does not have an exact analytical solution. The Navier-Stokes equation is a typical example of an equation where the solution is obtained numerically. Moreover, in contrast to experiments where a limited control over environmental factors is always present, simulations can also provide an artificial system that is easier to monitor; where the variables are simpler, more defined and easily isolated. The role of numerical methods have also gone beyond the tests of theories and complementing experimental results. They are also used as independent and predictive tools for material science research. The rapid growth of computer technology has also jolted the role of simulations in the field of complex systems. However, computational power is just one aspect. Of equal importance is the development of optimized programs that can tackle the problem we have today with the technology that is currently available.

Overview and Main Objectives

The general goal of this thesis is to provide advanced numerical models that can be used to understand the effects of external forces in colloidal suspensions. Two simulation techniques are used: Brownian Dynamics (BD) and the hybrid Stochastic Rotation Dynamics - Molecular Dynamics (SRD-MD). BD is a traditional method used in the study of colloidal systems that does not account for HIs. On the other hand, SRD-MD is one of the well-known techniques that can be used to reproduce short and long-range HIs successfully [25].

In Chapter 1, the objective is to familiarize the reader with the different mesoscale techniques available in literature. Since SRD-MD is relatively new in comparison with other simulation methods, and because a considerable part of this thesis is focused on developing this technique, most of the chapter is dedicated to introducing SRD-MD.

In Chapter 2, the first type of perturbation in the form of shear is introduced. Since shear is synonymous to HIs, it is imperative to properly account for hydrodynamic effects and hence SRD-MD is employed. The dependence of the shear viscosity of hard spheres on volume fraction has never been quantitatively verified for dense cases. Moreover, the calculation of shear viscosity can serve as a model problem, not only for verifying the proper modeling of HIs, but also for the inclusion of shear forces. Hence the objective of Chapter 2 is to develop SRD-MD so that it can be used as a tool to calculate and characterize the shear viscosity of both dilute and concentrated systems.

The calculation of shear viscosity in Chapter 2 serves as a framework that gives way to the study of other rheological properties of more sophisticated systems. Chapter 3 focuses on the percolation behavior of alumina suspensions by computer simulations. There are no external forces introduced in this chapter. However, the determination of the percolation threshold of real systems (with HIs) can be useful for the prediction of the yield stress magnitude. This study is performed to identify the key factors that affect the magnitude of percolation threshold: the strength of colloid-colloid attractions and the presence of HIs. BD and SRD-MD simulations are used to isolate the effects of HIs. The results are also compared with the yield stress study presented in Refs. [21, 26]

Finally, Chapter 4 explores the possible alterations to the structures of the colloids when an attractive surface or an oscillating shear is introduced. For the case of the attractive wall, a binary colloidal suspension described by a Yukawa potential is used. The potential applications of this work can range from surface deposition of colloids, to polymer and protein adsorption. For now, the effects of HIs are ignored. Hence this part of the thesis is studied by BD simulations only. The goal of this chapter is to see how an attractive wall can alter the predicted equilibrium structure of an aggregate. The parameters that influence the modifications in the structure are also analyzed. For

the case of an oscillating shear, the same system used in Chapter 3 is employed. This method of agitating the suspension can induce some reorganization, which is otherwise difficult to achieve when the system remains in equilibrium or by merely changing its static properties. The main objective is to determine if the ordering of colloidal structures can improve when the aggregation process is hindered, to some extent, by an oscillatory force.

Chapter 1 :

Simulation Techniques

1.1   Scale separation

The motion of colloids in a suspension is rather a complex phenomenon. Its stochastic aspects can be captured by a Brownian motion description [27] but this in itself is often insufficient. Hydrodynamic interactions (HIs), which describe the momentum transfer through the fluid [24], is another aspect of the motion of colloids in a suspension that is usually more computationally intensive. For dilute suspensions, the HIs decay fast with the distance between the colloids hence HIs can be ignored in many dilute Brownian systems. However, HIs are enhanced as the concentration of the suspension increases and must be incorporated accordingly [28]. Moreover, in cases where external shearing is present, HIs also lead to a non-Newtonian behavior. Clearly, the inclusion of HIs in simulations is a crucial tool in the study of colloidal science.

The main challenge in modeling HIs in colloidal suspensions lies in addressing the issue of *scale separation*, a characteristic feature of mesoscopic systems which is also present in systems such as polymers, liquid crystals, vesicles, viscoelastic fluids, red blood cells and fluid mixtures [29]. To illustrate, a typical colloid with diameter of 10^{-6} m can displace up to 10^{10} water molecules. And since the length scale of the colloid is coupled to its time scales, there exists a spectrum of time scales that governs the physics of a colloid that is embedded in the fluid. For example, the time it takes for Brownian motion to emerge is different from the time it takes for hydrodynamic effects to set in, and both are different from the time scale of interest.

The response to the problem of huge size difference between the colloids and the solvent molecules: a coarse-grained representation of the system. The first step is a model, which treats the collisions between the colloids and the solvent molecules as completely random. This is the Brownian description, in which the interaction is described by white noise and the frictional coefficients. The two terms are related to each other at thermal equilibrium by the fluctuation-dissipation theorem. Then, to account for the momentum exchange with the fluid and all subsequent correlations, the HIs must also be represented.

To deal with the complications caused by scale separation, it is important to understand the different time scales of the system under study. The relevant time scales used in this work, together with their brief descriptions, are listed below.

The largest among them is the *Diffusion time scale*, which is the time it takes for a colloid to diffuse over its diameter. This is also the time scale implemented in this thesis since the properties of interest are best observed in the diffusion regime. Mathematically, this is defined as:

$$\tau_D = \frac{2a^2}{D_0},\tag{1.1}$$

where $D_0 = k_B T/\zeta$ is the diffusion coefficient of an isolated colloid, a is the radius of the colloid, $\zeta = 6\pi\eta a$ is the friction coefficient, and η is the viscosity of the fluid.

Following the diffusion time is the *Brownian time scale* τ_B, which is a measure of the time needed for a colloid to lose memory of its velocity. From Ref. [30, 31], this is given by

$$\tau_B = \frac{M}{\zeta}, \tag{1.2}$$

where M is the mass of the colloid. To reproduce the correct diffusive properties of the fluid, the velocity correlation should decay to zero before it has diffused or convected over its own radius so that $\tau_B << \tau_D$ [30].

The time scale for Brownian motion is known as the *Fokker-Planck time scale* given by τ_{FP}, above which, the kicks coming from the interaction with the fluid become randomly distributed. On the other hand, the time scale needed for hydrodynamic effects to emerge is known as the *Kinematic time scale*. This is the time required for the fluid momentum to diffuse one colloidal diameter:

$$\tau_\nu = 2\frac{a^2}{\nu}, \tag{1.3}$$

where $\nu = \eta/\rho_f$ is the kinematic viscosity and ρ_f is the density of the fluid. Among the smallest fluid time scale is the *Fluid relaxation time scale* τ_f, with typical values of 10^{-14} s to 10^{-13} s for water. This is the time it takes for the velocity correlations of the fluid to decay. This should be smaller than the other colloid relaxation times. Moreover, to properly model Brownian motion and HIs, they should be ordered so that $\tau_f, \tau_{FP} << \tau_\nu << \tau_D$ [30].

Table 1.1 shows an example hierarchy of the relevant time scales for a colloid with a radius 255 nm in water. In this example, the time scales can differ by up to 13 orders of magnitude. Even the two most relevant time scales for the calculation of transport coefficients, i.e. diffusion time scale for diffusivity and kinematic time scale for viscosity [30], are separated by 6 orders of magnitude. The goal of mesoscale modeling is to overcome these vastly separated scales by "averaging-out" less important effects and retaining only those that are essential to the problem under study. A shortlist of desirable qualities of a successful simulation technique are provided by Allen and Tildesely [27]: (1) it has to be fast and requires a little memory; (2) it has to permit the use of a long time step in order to measure experimental values; (3) it has to duplicate classical trajectory as close as possible; (4) it should satisfy known conservation laws for energy and momentum; (5) and it has to be simple in form and easy to program.

At present, there is a wide selection of numerical models to choose from. As a starting point, the interested reader is referred to Ref. [32]. Some of the models mentioned in this work includes Brownian Dynamics (BD), Brownian Dynamics with Yamakawa-Rotne-Prager Tensors (BD-YRP), Dissipative Particle Dynamics (DPD), Lattice Boltzmann (LB) technique and Stochastic Rotations Dynamics (SRD). These models can be classified into continuum-based (BD and BD-YRP), lattice-based (LB) and particle-based (DPD

Table 1.1:   Hierarchy of time scales for a 255-nm alumina colloid suspended in water

Diffusion time	τ_D	1.5×10^{-1} s
Kinematic time	τ_ν	1.3×10^{-7} s
Brownian time	τ_B	5.7×10^{-8} s
Fluid relaxation time	τ_f	$10^{-14} - 10^{-13}$ s

and SRD) approaches. With a proper understanding of the capabilities and limitations of the models, one can decide the approach that is most effective for the intended application.

The remainder of the chapter is therefore dedicated to understanding how some mesoscale models work. Sec. 1.2 is about Molecular Dynamics (MD) since it is the foundation of most particle-based techniques. Secs. 1.3 and 1.4 describe BD, BD-YRP, DPD and LB methods respectively. Finally, Secs. 1.5 and 1.6 are devoted to understanding how SRD-MD is developed and implemented in this thesis.

1.2   Molecular Dynamics

Molecular Dynamics (MD) is among the pioneers in the numerical study of fluids and solids [33, 34, 35]. The implementation of MD is rather straight-forward. In its standard formulation, the Newtonian equations of motion of the particles in a fixed simulation box of volume V, are solved numerically:

$$\frac{d\mathbf{r}_i}{dt} = \mathbf{v}_i \ \text{ and } \ m_i \frac{d\mathbf{v}_i}{dt} = \mathbf{F}_i. \tag{1.4}$$

where m_i, $\mathbf{r}_i$ and $\mathbf{v}_i$ are the mass, position and velocity of the ith particle respectively and $\mathbf{F}_{ij} = \sum_{i \neq j} \mathbf{F}_{ij}$ is the total interaction force between particles i and j. $\mathbf{F}_{ij}$ can be evaluated from the interaction potential U_{ij} using:

$$\mathbf{F}_{ij} = -\nabla U_{ij}. \tag{1.5}$$

The trajectories of the particles are obtained by allowing the Eq. (1.4) to evolve at discrete time intervals Δt_{MD}. To integrate the equations of motion, one can employ the Velocity Verlet algorithm. In this method, the position and velocity of each of the particles are updated according to [27]:

$$\mathbf{r}_i(t + \Delta t_{\text{MD}}) = \mathbf{r}_i(t) + \mathbf{v}_i(t)\Delta t_{\text{MD}} + \frac{1}{2}\mathbf{a}_i(t)(\Delta t_{\text{MD}})^2; \text{ and} \tag{1.6}$$

$$\mathbf{v}_i(t + \Delta t_{\text{MD}}) = \mathbf{v}_i(t) + \frac{1}{2}\left[\mathbf{a}_i(t) + \mathbf{a}_i(t + \Delta t_{\text{MD}})\right](\Delta t_{\text{MD}}); \tag{1.7}$$

where $\mathbf{a}_i = \mathbf{F}_i/m_i$ is the acceleration of the ith particle.

The main limitation of MD is the number of particles it can handle. Both the colloid and fluid particles have to be simultaneously evaluated for MD to work. Moreover, one phenomenon of interest happens faster than the others and employing a very small time step means that longer simulation times cannot be reached. Hence, even with the speed and memory capacity of computers today, a full MD simulation is impractical, if not impossible.

MD however is not completely out of the picture since the central idea of most mesoscale simulations is to apply a two-level simulation approach. The colloids, being relatively smaller in number, are allowed to evolve with MD; while the fluid is defined in a simpler manner, e.g. by random and frictional forces as in BD or by other mesoscale methods like DPD, LB or SRD.

1.3 Brownian Dynamics

In the Brownian Dynamics (BD) technique, the fluid particles are omitted in the simulation. Instead, the fluid has a continuum description and its effects are approximated by frictional forces and random forces [27]. The velocities and positions for N_c colloids can be obtained by successive integration of the Langevin equation at a time interval Δt_{BD}:

$$M\frac{d\mathbf{v}_i(t)}{dt} = \boldsymbol{\Gamma}_i(t) + \sum_j \mathbf{F}_{ij}\{\mathbf{r}_{ij}(t)\} + \boldsymbol{\Xi}_i(t). \qquad (1.8)$$

In this formulation, $\boldsymbol{\Gamma}_i(t)$ represents the random forces received by the colloids from the interaction with the fluid and are assumed to be independent of the velocity of the colloids [36]. $\mathbf{F}_{ij}\{\mathbf{r}_{ij}(t)\}$ represents the interparticle forces from the other colloids present in the suspension. The forces can be evaluated from the potential energy $U(r_{ij}) = U_{ij}$. The final term represents the frictional forces and is given by $\boldsymbol{\Xi}_i(t) = -\zeta\mathbf{v}_i(t)$, where $\zeta = 6\pi\eta a$ is the friction coefficient.

If we look for a solution to Eq. (1.8) at a time scale larger than the velocity relaxation time, then the inertial term, i.e. the last term at the right hand side of Eq. (1.8), can be neglected. To achieve this, a time scale that is greater than the velocity relaxation time can be imposed: $\Delta t_{\mathrm{BD}} >> \tau_B$. With this restriction, the solution to Eq. (1.8) simplifies to:

$$r_i(t + \Delta t_{\mathrm{BD}}) = r_i(t) + \sqrt{\frac{2k_BT}{\zeta}}(\Delta t_{\mathrm{BD}})^{1/2}Y_i + \frac{1}{\zeta}\sum_j F_{ij}\{r_{ij}(t)\}\Delta t_{\mathrm{BD}}, \qquad (1.9)$$

where Y_i are uncorrelated Gaussian variables with average of zero and standard deviation of one. At this time scale, the diffusive regime (τ_D) of the colloids is properly

reproduced. Moreover, since the velocity correlations decay more rapidly than the time scale considered, only the positions of the colloids are followed [36].

Among the major consequences of removing the fluid in BD is that HIs are ignored. On one hand, the elimination of HIs greatly simplifies the computation. This is also the main reason why the standard BD presented above is extensively utilized and have been very successful in problems where hydrodynamic effects are negligible [37, 38, 39]. On the other hand, HIs are omnipresent in nature so that there is also wide range of problems that require models that correctly account for hydrodynamic effects.

Therefore, it comes as no surprise that BD has been extended to incorporate HIs [40, 41, 36]. In general this is achieved by making the diffusion coefficient dependent on the position of the colloids. The incorporation of HIs is usually carried out by employing diffusion tensors, which represent both the diffusive and frictional effects occuring in the system. One of the widely used formulation is the Yamakawa-Rotne-Prager (YRP) diffusion tensor:

$$\mathbf{D}_{ij} = \delta_{ij}\frac{k_BT}{6\pi\eta a}\mathbf{I} + \frac{k_BT}{8\pi\eta r_{ij}}\left(\mathbf{I} + \frac{\mathbf{r}_{ij}\mathbf{r}_{ij}^T}{r_{ij}^2}\right) - \frac{k_BT}{8\pi\eta r_{ij}^3}(2a^2)\left(\frac{\mathbf{r}_{ij}\mathbf{r}_{ij}^T}{r_{ij}^2} - \frac{1}{3}\mathbf{I}\right), \qquad (1.10)$$

when $r_{ij} > 2a$; and

$$\mathbf{D}_{ij} = \frac{k_BT}{8\pi\eta a^2}\left[\left(\frac{4a}{3} - \frac{3r_{ij}}{8}\right)\mathbf{I} + \frac{r_{ij}}{8}\frac{\mathbf{r}_{ij}\mathbf{r}_{ij}^T}{r_{ij}^2}\right], \qquad (1.11)$$

when $r_{ij} \leq 2a$. The term $\mathbf{I}$ is the identity tensor while δij is the Kronecker delta. While BD-YRP is an improvement from standard BD, this approach is still computationally intensive and imposes serious limitations on the size of the system that can be studied. First, one of the most important approximations used to derive this tensor is to consider that HIs are pairwise additive. This means that the total potential of the system must be represented as the sum of all two-body interactions, which can be memory consuming. In addition to this, it does not model short range HIs but only long range HIs. Therefore, this tensor is generally appropriate for systems with relatively low colloid volume fractions. Second, from the point of view of computation efficiency, the computational cost increases drastically with increasing number of Brownian particles N_c since BD-YRP requires tensor evaluation that scales as $\mathcal{O}(N_c^2)$ and diagonalization that scales as $\mathcal{O}(N_c^3)$.

1.4   Other Mesoscale Methods

1.4.1   Dissipative Particle Dynamics

Dissipative Particle Dynamics (DPD) is developed by Hoogerbrugge and Koelman in 1992 [5, 4] to address the computational limitations of MD and BD. Moreover, they showed that DPD mimics the behavior of a Navier-Stokes flow [5]. The DPD particles can be viewed as static "clumps" of fluid molecules interacting with very soft interparticle potentials [24, 30]. Since it is an extension of standard MD, the dynamical variables are evolved similar to Eq. (1.4) where the forces are defined by particle pairs. In general, the total force is given by[24, 42]:

$$\mathbf{F}_{ij} = \mathbf{F}_{ij}^c + \mathbf{F}_{ij}^d + \mathbf{F}_{ij}^f. \tag{1.12}$$

The term $\mathbf{F}_{ij}^c$ represents the interparticle forces and $\mathbf{F}_{ij}^d$ represents the velocity-dependent frictional forces given by

$$\mathbf{F}_{ij}^d = -\sum_j \zeta(r_{ij}) \left[(\mathbf{v}_i - \mathbf{v}_j) \cdot \hat{r}_{ij} \right] \hat{r}_{ij} \tag{1.13}$$

where $\zeta(r_{ij})$ is the relative friction coefficient for particle pairs and $\hat{r}_{ij}$ is the unit vector in the direction of $\mathbf{r}_{ij}$. The stochastic forces also act along the line of centers:

$$\mathbf{F}_{ij}^f = \sum_j \varsigma(r_{ij}) \eta_{ij} \hat{r}_{ij}, \tag{1.14}$$

where η_{ij} is the noise term and $\varsigma(r_{ij})$ determines the strength of the stochastic force applied to the particle pair [24]. The advantages of DPD over standard MD and BD are: (a) it allows a longer time step because of the larger size of DPD particles and the softer interactions between them; and (b) the DPD particles also interact by velocity dependent frictional forces which automatically accounts for HIs [24]. There are also several proposed refinements to the original formulation, which include a mechanism where the solvent can transfer shear forces to the solute [43, 42]. Similar to BD-YRP however, DPD is still computationally demanding due to the pairwise forces that require evaluation every time step.

1.4.2   Lattice-Boltzmann

The Lattice Boltzmann (LB) method is another prominently featured simulation technique for soft matter systems. LB originated from lattice gas automata, a discrete particle kinetics utilizing discrete lattices and discrete times. LB has a huge and rich

background starting from the Broadwell model in 1964 [44], which can be viewed as a one-dimensional lattice Boltzmann equation [45]. In LB, the fluid density at a lattice site $\mathbf{r}$ with velocity $\mathbf{c}_i$ just prior to the collision is represented by $n_i(\mathbf{r}, t)$. The discrete time interval is given by Δt_{LB}. The system is evolved by using a linearized and preaveraged Boltzmann equation that is discretized and solved on a lattice:

$$n_i(\mathbf{r} + \Delta t_{\mathrm{LB}}\mathbf{c}_i, t + \Delta t_{\mathrm{LB}}) = n_i(\mathbf{r}_i, t) - \frac{\Delta t_{\mathrm{LB}}}{\tau_{\mathrm{LB}}}\left[n_i(\mathbf{r}_i, t) - n_i^{eq}(\mathbf{r}, t)\right] \tag{1.15}$$

where $n_i^{eq}(\mathbf{r}, t)$ is the local equilibrium value with a time scale τ_{LB} that is related to the fluid viscosity [46]. From the moments of $n_i(\mathbf{r}, t)$, relevant quantities such as hydrodynamic field, mass density, momentum density and momentum flux can be obtained. Through the appropriate constraining of the equilibrium distribution function and using a Chapman-Enskog expansion, the Navier-Stokes equation is obtained from the linearized Boltzmann equation.

This described implementation of LB is computationally efficient. While the thermal fluctuations are not included in its original formulation [47] and the incorporation of thermal fluctuations was relatively recent and is coined as the Fluctuating Lattice Boltzmann (FLB) [46] approach, this new development in LB made it a versatile simulation tool that can be used when thermal fluctuations need to be isolated or added.

1.5 Stochastic Rotation Dynamics

Stochastic Rotation Dynamics (SRD), also known as Multiparticle Collision Dynamics (MPCD) is first developed by Malevanets and Kapral in 1999 [25, 48, 49]. SRD is a particle-based approach, where the fluid is represented by N_f point particles. The number of fluid particles is significantly smaller compared to the number of particles that MD requires. Moreover, it has a larger length scale than real fluid molecules hence allowing simulation of longer time scales. SRD can be interpreted as a Navier-Stokes solver that includes thermal noise [30], where the SRD fluid serves as a convenient way to coarse-grain the properties of the real fluid. The algorithm is a two-step process: the streaming step and the collision step that are implemented at regular time intervals Δt_{SRD}. During each streaming step, the positions are updated according to the equation:

$$\mathbf{r}_i(t + \Delta t_{\mathrm{SRD}}) = \mathbf{r}_i(t) + \mathbf{v}_i(t)\Delta t_{\mathrm{SRD}}, \tag{1.16}$$

where $\mathbf{r}_i$ and $\mathbf{v}_i$ are the ith particle's position and velocity respectively.

Unlike the previous mesoscale simulations, the SRD fluid particles are sorted in even more manageable groups before the collision rule is implemented. This approach of

coarse-graining the fluid significantly simplifies the process. The particles are placed into "collision cells" of side length a_0, where random rotation of velocities takes place. The choice of a_0 is based on colloid size and is set to $a/2$ in this work. The volume of the simulation box can be defined such that $V = L_x \times L_y \times L_z = (l_x \times l_y \times l_z) \times a_0^3$, where l_x, l_y and l_z are integers and a_0^3 is the cell volume. Each cell contains an average of $\gamma = 5$ fluid particles. This is the typical value applied in most simulation studies [1, 2, 50] mainly because it balances computational efficiency and resolution. Particle exchanges between cells are allowed but the number of fluid particles in the simulation box is conserved and kept at N_f. The collision per cell is performed by rotating the velocities of the particles relative to the center of mass velocity $\mathbf{v}_{\mathrm{cm}}$ according to the equation:

$$\mathbf{v}_i(t + \Delta t_{\mathrm{SRD}}) = \mathbf{v}_{\mathrm{cm}} + \mathbf{R}(\alpha) \left[\mathbf{v}_i(t) - \mathbf{v}_{\mathrm{cm}}\right], \tag{1.17}$$

where $\mathbf{R}$ is a rotation matrix [51]. In three dimensions, the rotation is fixed at an angle α about a randomly chosen axis. The value of α can range from $0°$ to $180°$. The rotations by $-\alpha$ need not be considered since this is equivalent to a rotation by α about an axis with the opposite direction. However, the simplest rotation algorithm is when α is set to $90°$.

The dimensionless mean free path λ is the average fraction of a cell travelled by a fluid particle during a streaming step. This is given by

$$\lambda = \frac{\Delta t_{\mathrm{SRD}}}{a_0} \sqrt{\frac{k_B T}{m_f}}, \tag{1.18}$$

where m_f is the mass of the fluid,

$$m_f = \frac{a_0^3 \rho_f}{\gamma}, \tag{1.19}$$

and ρ_f is the mass density. If between each collisions, the particles travel a distance that is smaller that the cell size i.e. $\lambda/a_0 << 1$, then even after several time steps, the same particles remain in a given cell and their motion become correlated. This leads to a breakdown in molecular chaos assumption and Galilean invariance is destroyed. One way to go around this problem is to choose $\lambda/a_0 > 0.5$. However this choice of λ would model a fluid that is "gas-like" rather than "liquid-like" [30]. For a gas, the momentum transport is dominated by mass diffusion through the streaming of particles; while for a liquid, momentum transport is governed by interparticle collisions. Hence simulating a liquid-like behavior would require $\lambda/a_0 << 0.5$. Following previous studies by Refs. [1, 2, 30], λ is set to a value of 0.1, which should suffice for the representation of the hydrodynamics of a liquid.

To restore Galilean invariance assumptions, a grid-shift procedure is employed [1].
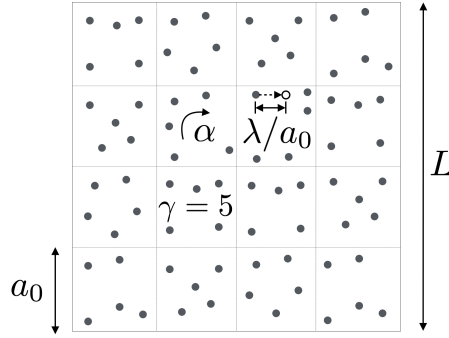
Figure 1.1: Schematic diagram of a sample 2-D SRD system with cell size a_0, $\gamma = 5$ and simulation box length of $L = 4 \times a_0$.

This is done by constructing a new cell-grid that is randomly translated at a certain distance before each collision step. Collisions are performed in the shifted cells thus allowing exchange of particles. Particles are then reverted back to the original cells and the SRD process is continued.

The described process conserves linear momentum and mass and is sufficient to ensure that in the macrsocopic limit, the SRD process recovers the continuity and Navier-Stokes equations. A schematic diagram of a sample SRD system is shown in Fig. 1.1. By carefully choosing the values of the SRD parameters ($\alpha, a_0\gamma, \lambda, m_f$ and T), one can adjust the properties of the fluid to fit the system being modeled.

1.5.1   Sheared SRD fluid

In this section, the method of implementing shear on particles is discussed. As a starting point, the shearing of a pure SRD fluid, i.e. without embedded colloids, is illustrated. In fact, the original formulation of SRD by Malevanets and Kapral [25, 48] used an equilibrium system so that the introduction of shear by Kikuchi et al. [2] served as a development of the previous model. This is because shear provides a new numerical approach for studying the flow behavior of a fluid that can be extended over different shear magnitudes [2]. A more useful application of shear modeling is geared towards the understanding of the effects of shearing on the behavior of the embedded particles in the fluid. From here, one can extend the range of applications of SRD-MD in the study of rheology of colloidal suspensions. Example cases include shear thinning [31, 52] and other flow-induced properties [53, 28]. Moreover there are different possibilities of extending the study of sheared suspensions since the presence of an external force such as shear is already very common in nature [54].

One of the common approaches used to introduce shear is to confine the fluid particles in a channel by placing a wall at the top and bottom surfaces of the simulation box and exposing the SRD-fluid to a constant external force that yields a parabolic flow profile

[53, 55, 56]. In Ref. [53] for example, the walls are considered as consisting of an immobile monolayer of interaction sites with homogeneous density. The walls are placed at $r_x = 0$ and $r_x = L_x$ and are defined by an effective interaction potential given by:

$$V_{wf} = \begin{cases} \frac{2}{3}\pi\epsilon_{\text{wall}} \left[\frac{2}{15} \left(\frac{\sigma_{\text{wall}}}{r_x} \right)^9 - \left(\frac{\sigma_{\text{wall}}}{r_x} \right)^3 + \frac{\sqrt{10}}{3} \right] & r_x \leq (2/5)^{\frac{1}{6}} \sigma_{\text{wall}} \\ 0 & r_x > (2/5)^{\frac{1}{6}} \sigma_{\text{wall}}, \end{cases} \tag{1.20}$$

where σ_{wall} is the interaction parameter between the fluid particles and the wall particles, $\frac{2}{3}\pi\epsilon_{\text{wall}}$ is the effective potential well depth and r_x is the distance of the fluid particle from the wall. Eq. (1.20) is repulsive and only varies perpendicular to the plane defining the wall. The external force applied is given by:

$$v_z(r_x) = \frac{g}{2\nu}(L_x - r_x)r_x, \tag{1.21}$$

where g is the acceleration constant of the flow, $\nu = \eta/\rho$ is the kinematic viscosity of the fluid. Hence the shear rate is given by:

$$\dot{\gamma}(r_x) = \frac{g}{2\nu}(L_x - 2r_x). \tag{1.22}$$

However, this kind of wall representation can lead to wall effects [57] like solid-fluid boundary conditions and the introduction of pseudo-particles [50]. As an alternate approach, shear can be introduced by simply modifying the periodic boundary conditions. This method was proposed by Lees and Edwards [58] for molecular fluids in 1972 and can easily be adapted for SRD fluids. Unlike the representation of actual walls, Lees-Edwards boundary conditions (LEBC) do not have these kinds of numerical instabilities since the simulation of shear is done by merely shifting the simulation boxes. The LEBC work by updating the positions and velocities of the particles with the usual periodic boundary conditions for y and z directions. However, when a particle crosses the upper or lower boundaries of the simulation box i.e. at $r_x = 0$ and $r_x = L_x$, its position and velocity are updated with a different rule to sustain the shear. Particles crossing the upper boundary will have an additional velocity of $+\dot{\gamma}L_x$ and a position shift of $+\dot{\gamma}L_x t$, where t is the total elapsed time. In contrast, particles crossing the lower boundary will have an additional velocity of $-\dot{\gamma}L_x$ and a position shift of $-\dot{\gamma}L_x t$. A planar Couette flow profile is set-up with a shear rate of

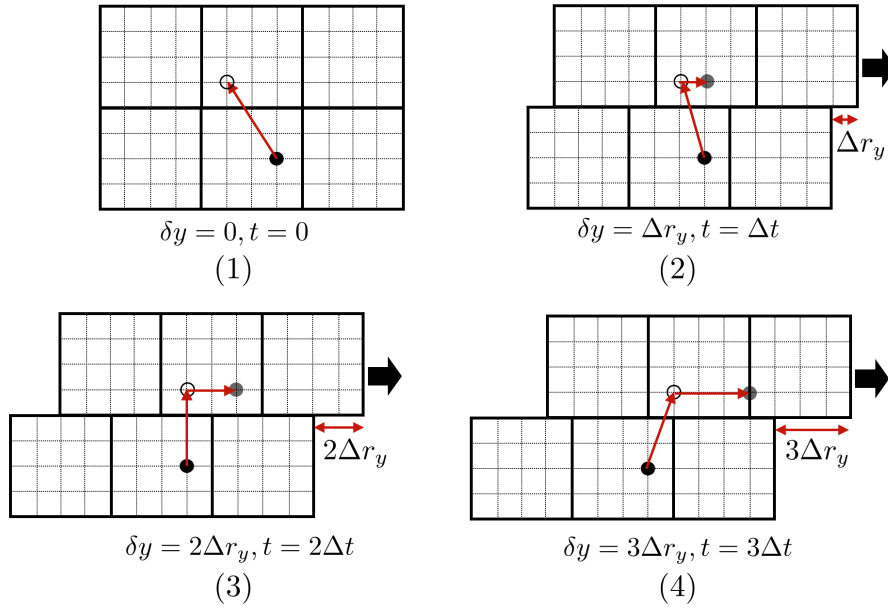$$\dot{\gamma} = \frac{\Delta v_y}{\Delta r_x} \tag{1.23}$$

Figure 1.2: Schematic diagram on how LEBC is implemented. Please refer to the text for more details.

where Δv_y is the shear velocity given by

$$\Delta v_y = \frac{\Delta r_y}{\Delta t} \tag{1.24}$$

Fig. 1.2 shows how LEBC is implemented step by step. At time $t = 0$, the simulation boxes are aligned obeying the usual periodic boundary conditions. When there is no shear, the simulation boxes are stationary and the evolution of the particle position is only dictated by the inter-particle dynamics. This is illustrated in Fig. 1.2a, where the change of position only goes from the black circle to the open circle. However when the shear is applied, aside from the displacement defined by the inter-particle dynamics, there is also the displacement due to shear. In the example shown in Fig. 1.2b, the top simulation boxes will move to the right at a distance of Δr_y after the first time step $t = \Delta t$. Hence the particle will first move from the black circle to the open circle due to the interparticle dynamics; then the particle will move from the open circle to the gray circle by a distance Δr_y due to the shear. The gray circle represents the final r_y coordinate of the particle. The shifted distance of the particle depends on the total time elapsed $t = n\Delta t$, where n is an integer, and the shear velocity Δv_y (see Figs. 1.2c and 1.2d). The same algorithm is applied on the simulation boxes at the bottom, only that the boxes move in the opposite direction. For reference, a sample fortran code is shown below.

The value `DELVY` corresponds to the shear velocity Δv_y while `totaltime` and

```
ashift = DELVY * totaltime
dely = ashift - anint(INVLENGY * ashift) * LENGY
corx = anint(INVLENGX * x - 0.5)
y = y - corx * dely
vy = vy - corx * DELVY
y = y - LENGY * anint(INVLENGY * y - 0.5)
x = x - LENGX * anint(INVLENGX * x - 0.5)
z = z - LENGZ * anint(INVLENGZ * z - 0.5)
```

`dely` store the total time and distance traveled by the simulation boxes respectively. Moreover since LEBC can maintain a linear velocity profile, the shear vicosity can be measured once the system reached a steady-state condition.

Further probing of rheological behavior can be obtained by changing the motion of the walls. Oscillatory walls for example can be used to measure the zero-shear viscosity limit or in the case employed in this thesis, to determine the self-assembly of the colloids within the aggregate. To simulate an oscillating motion for the walls, one simply needs to replace `DELVY` by a time-dependent velocity `dvy` given by:

```
dvy = DELVY * cos ( 2 * pi * totaltime * FREQ )
```

In this formulation, `DELVY` now describes the amplitude of oscillation while `FREQ` dictates the frequency of oscillation of the system. With this algorithm of introducing shear, the modulation of shear forces can easily be achieved.

1.5.2 Thermostats

Following the introduction of shear in the system is the use of a thermostat. The SRD fluid used in this work samples a microcanonical ensemble i.e. the energy of the system must be constant in time. A thermostat is a modification of the original simulation algorithm with the motivation of generating a microcanonical ensemble. Thermostats are usually employed to match the experimental conditions, to study temperature-dependent processes, to avoid energy drifts caused by the accumulation of numerical instabilities and for the purposes of this work, to dissipate heat in non-equilibrium conditions and ensure a steady-state condition [59]. Over the years, most of the thermostats developed are for MD [60, 61, 62]. However, since SRD is also a particle-based technique, some of these thermostats can be adapted to suit the SRD fluid [52].

To begin the understanding of the thermostat algorithm, there are several temperatures to be defined. First is the reference temperature T_0, to which the temperature of the sytem is driven. This value is set to $T_0 = 293\,\mathrm{K}$ in this work so that the systems studied are at room temperature. Next is the instantaneous temperature

given by

$$\mathcal{T} = \frac{2}{3k_B N} \mathcal{K}, \tag{1.25}$$

where $\mathcal{K}$ is the kinetic energy:

$$\mathcal{K} = \frac{1}{2} \sum_i^N m_i (v_i^2 - v_{cm}^2). \tag{1.26}$$

According to Hünenberger [59], temperature fluctuations characterize the rate of energy transfer from the heat bath to the system. The spread of this fluctuations is given by

$$\sigma_T = \sqrt{\langle \mathcal{T}^2 \rangle_{NVT} - \langle \mathcal{T} \rangle_{NVT}^2} = 2NT. \tag{1.27}$$

Finally, T is the average temperature of the system that is checked every time step.

1.5.2.1   Simple Scaling Thermostat

One of the commonly used thermostats is the simple scaling thermostat. In this method, the scaling factor S is chosen such that

$$S = \sqrt{\frac{3N_f k_B T_0}{2 \sum_i^{N_f} m_i (v_i^2 - v_{cm}^2)}}. \tag{1.28}$$

This kind of thermostat can be used for fluids in equilibrium and was employed in Ref. [63] for the calculation of diffusion coefficient. However, it tends to show instabilities for fluids under external shear. In most equilibrium systems, the simple scaling of temperature should suffice. However, one needs to note that the energy fluctuations are incompatible with an isothermal ensemble so that the distribution of velocities in a collision cell is no longer Maxwellian [52]. The smearing of velocity distribution profiles can have a huge effect in the calculation of viscosity, hence a good thermostat is an integral part of modeling suspensions under shear.

1.5.2.2   Monte-Carlo Thermostat

Thermostats permitting fluctuations are more likely to represent the correct dynamics of the systems than the simple scaling thermostat. To answer the requirements of the system at hand, an alternative cell-level thermostat is used. The Monte-Carlo thermostat is a computationally efficient thermostat for SRD that accounts for the coarse-graining by collision cells. The original formulation was by Heyes [64] for molecular fluids and was adapted in Ref. [31, 65] for SRD-MD. This method also conserves the linear momentum and temperature of the system without smearing out the velocity profile, or changing the
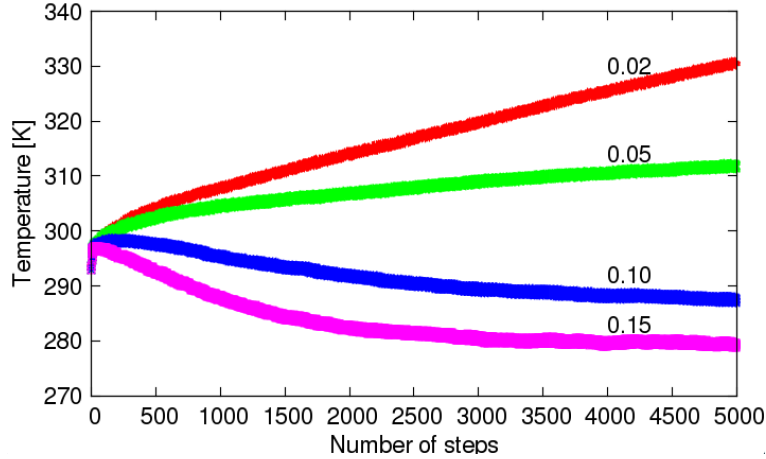
Figure 1.3: The effect of varying the thermostat strength c on the system temperature.

viscosity of the fluid [29]. Ref. [29] outlined the algorithm as follows.

First, the strength c of the thermostat is dictated. A higher c corresponds to a stronger thermostat. Second, a number is randomly chosen in the range $\psi \in [1, 1 + c]$ and the scaling factor is given a value of either $S = \psi$ or $S = \psi^{-1}$, each having a probability of $1/2$. Third, another random number is chosen in the range $\xi \in [0, 1]$. If ξ is less than the acceptance probability that is given by $p_A = min(1, A)$, where

$$A = S^{3(\gamma - 1)} \exp\left[-\frac{m_f}{2k_B T_0} \sum_{i=1} (\mathbf{v}_i - \mathbf{v}_{cm})^2 \left\{S^2 - 1\right\}\right], \tag{1.29}$$

then the velocities are rescaled by scaling the rotation matrix $S\mathbf{R}$ in Eq. (1.17). Otherwise, the rotation matrix is kept at $\mathbf{R}$. This thermostat produces a Maxwellian velocity distribution and does not change the viscosity of the fluid. Moreover, the collision rule can be varied as long as the correct macroscopic conservation laws, such as mass, number density and momentum are conserved [66]. The use of the thermostat means that the energy is not conserved in the original implementation of SRD, however it is retained in the statistical sense. To demonstrate how the the thermostat works, Fig. 1.3 shows how thermalization occurs in a system for various thermostat strengths. A high magnitude of c can drive the temperature to a lower value faster than a c with a relatively smaller magnitude. The value of c can be adjusted until the correct system temperature is achieved. Therefore, several time steps are required before proceeding with the actual measurements to ensure that the temperature is at the desired value.

1.5.3   Coupling SRD with MD

After treating SRD and MD separately (Secs. 1.2 and 1.5), one can proceed with the SRD-MD model wherein the fluid-fluid interactions are treated using SRD as described

above and the colloid-colloid interactions are treated by MD. For the MD part, the choice of interaction potential in Eq. 1.5 depends on the system in question. In the simplest case, one can use the inverse-power (IP) potential of the form:

$$U_{cc} = \begin{cases} \varepsilon_{cc} \left(\frac{\sigma_{cc}}{r} \right)^{12} & (r < r_{cc}) \\ \\ 0 & (r > r_{cc}), \end{cases} \tag{1.30}$$

where $\varepsilon_{cc} = 2.5 k_B T$ and $r_{cc} = 2.5 \sigma_{cc}$. The variable σ_{cc} is the colloid interaction parameter set to $\sigma_{cc} = d = 2a$.

On the other hand, the colloid-fluid dynamics can be described either by SRD as in Refs. [31, 65, 67], where the colloids are treated as point particles from the point of view of the fluid particles; or by MD, where the colloids have a non-vanishing size. A schematic diagram is shown in Fig. 1.4. Ref. [68] explored the differences between the two coupling schemes and found that the effects of HI's on diffusion coefficient and conductivity are more pronounced when MD is used. Since shear viscosity is more sensitive to hydrodynamic effects than diffusion and conductivity, an MD coupling scheme is more suitable for its calculation.

The MD coupling proceeds by summing the three different types of interactions present in the colloidal suspension: interactions between colloids that occur at MD time-scale (Δt_{MD}), interactions between fluid particles that occur at SRD time-scale $(\Delta t_{\mathrm{SRD}})$, and interactions between colloids and fluid particles that occur at MD time-scale. The fluid-fluid interaction potential V_{ff} is set to zero. Hence the interactions among fluid particles are solely described by SRD. For the dynamics between colloids and fluids we use an IP potential which is similar in form as in Eq. 1.30 but with the parameters corresponding to colloid-fluid interactions:

$$U_{cf} = \begin{cases} \varepsilon_{cf} \left(\frac{\sigma_{cf}}{r} \right)^{12} & (r < r_{cf}) \\ 0 & (r > r_{cf}), \end{cases} \tag{1.31}$$

where $\varepsilon_{cf} = 2.5 k_B T$ and $r_{cf} = 2.5 \sigma_{cf}$. Unlike σ_{cc}, the choice of σ_{cf} is not as straightforward since the colloids are viewed as solid interfaces moving with respect to the fluid. To determine the appropriate value for σ_{cf}, the following considerations must be made.

The colloid-fluid boundary can be categorized to *stick, slip* or *mixed* boundary conditions [69]. The stick boundary condition is also known as no-slip boundary condition. This is the case where the tangential component of the fluid velocity vanishes at the interface. The corresponding frictional coefficient is $\zeta = 6\pi\eta a$. Both the linear and angular momentum are conserved in this set-up. On the other hand, in the slip boundary conditions, the tangential component of the fluid is unaffected by the presence of the
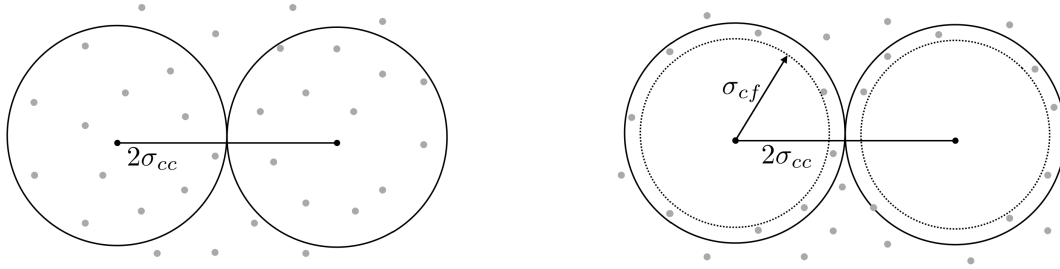
Figure 1.4: The two kinds of coupling for SRD-MD. On the left is by SRD where the colloids are treated as point particles from the point of view of the fluid and on the right is by MD where the colloids are treated as spheres with volume $4\pi\sigma_{cf}^3/3$

interface. This set-up conserves the linear momentum but does not transfer angular momentum. The corresponding frictional coefficient is $\zeta = 4\pi\eta a$. Despite the absence of angular momentum conservation however, the shear viscosity of the pure fluids can still be accurately obtained [69]. Note however that physical systems resembles partial slip boundary conditions that lies in between the stick and slip definitions. In the mixed boundary conditions, the relative tangential velocity of the fluid is diminished near the surface but remains zero [69].

The MD-coupling scheme that is employed in this work leads to an effective slip boundary conditions, hence the friction coeffcient $\zeta = 4\pi\eta a$ is used. The consequences of this manner of coupling are as follows. First, it is important to choose σ_{cf} to be slightly less than the colloid radius a to avoid unphysical depletion attraction between colloids. Depletion forces are due to spurious interactions that arise from the coarse-grained nature of the fluid when colloids approach each other at short distances [30, 70]. In this work, $\sigma_{cf} = 0.8a$ is implemented. Subsequently, the fluid particles can slightly penetrate the surface of the colloids. Even when the colloids are in contact, the fluid particles can slide between the colloids thus adding lubrication to colloid-colloid interactions. Second, the free volume accessible to the fluid particles is now dictated by σ_{cf} rather than a. This is defined by

$$V_f = (32a_0)^3 - N_c\frac{4}{3}\pi\sigma_{cf}^3 \tag{1.32}$$

where N_c is the number of embedded colloids. In addition, we know from Ref. [63] that the Schmidt number (Sc) of the fluid increases with increasing number of colloids. To keep Sc constant with increasing volume fraction, the number of fluid particles is decreased according to V_f i.e.

$$N_f = 32^3\gamma - N_c\frac{4}{3}\pi\left(\frac{\sigma_{cf}}{a_0}\right)^3\gamma. \tag{1.33}$$

Finally, if the SRD-coupling is used, the colloids directly undergo the thermostat algorithm with the fluid particles during the rotation steps. For the MD-coupling on the

other hand, there is no actual thermostat algorithm that is applied to the colloids but the interactions between the colloids and the fluid during the MD steps allow both colloid and fluid particles to be thermally coupled.

1.6 Mapping between physical and SRD-MD time scales

We have seen that the system consisting of colloids embedded in the fluid has several parameters that can be adjusted to provide the desired properties for the model. This section focuses on determing the values of these parameters in order to map the simulation scales to physical scales.

As mentioned in Sec. 1.1, the mesoscopic nature of colloidal suspensions results to a wide range of time scales. SRD-MD compresses this hierarchy of times scales so that only one time scale can be accurately reproduced. There are two significant time scales to which the mapping is usually done: the diffusion time scale τ_D and the kinematic time scale τ_ν. SRD-MD gives the liberty of selecting the fastest time scale to optimize the simulation. This contraction has the consequence that some physical quantities take values that are far from the actual experimental values. For example, a system mapped to the diffusion time scale will give the wrong magnitude of shear viscosity but the correct magnitude of the diffusion coefficient. However, a system mapped in kinematic time scale will give a wrong magnitude for diffusion coefficient but a correct magnitude for shear viscosity. As mentioned in Ref. [30], the quantitative value is not important as long as the correct regime of the hydrodynamic numbers is obtained and the different time scales are well separated. The diffusion time scale is used in this study because it significantly reduces the computation time by allowing the use of bigger time steps. Hence longer times scales can be reached at faster rates. Nevertheless, it is important to account for these changes in magnitude and determine the appropriate time scale for a specific system.

To map to the diffusion time scale, one first needs to calculate the physical diffusivity of a colloid in water. This is given by

$$D_0 = \frac{k_B T}{(6\pi \eta_{\mathrm{H_2O}} a)}. \tag{1.34}$$

Notice that in Eq. 1.34, the friction coefficient is the one that correponds to stick boundary conditions. Since slip boundary conditions are applied in the simulated systems, the friction coefficient used in Eq. (1.34) is equated to the simulated friction coefficient.

To solve for the corresponding diffusion coefficient in the SRD-MD simulations (D_{SRD}), it is important to note that the friction coefficient of the SRD fluid in the simulations

has two components [30]. The first one comes from the Brownian collisions and can be calculated by a simplified Enskog-Boltzmann-type kinetic theory that is adapted for slip boundary conditions. This is given by

$$\zeta_E = \frac{8}{3} \left(\frac{2\pi k_B T M_c m_f}{M_c + m_f} \right)^{1/2} n_f \sigma_{cf}^2, \tag{1.35}$$

where $n_f = \gamma/a_0^3$. Since $a_0 \lambda/(\Delta t_{\mathrm{SRD}}) = \sqrt{k_B T/m_f}$, Eq. (1.35) can be written as

$$\zeta_E = \frac{8}{3} \left(2\pi \frac{M_c}{M_c + m_f} \right)^{1/2} \gamma \left(\frac{\sigma_{cf}}{a_0} \right)^2 \frac{m_f \lambda}{\Delta t_{\mathrm{SRD}}} = \xi_E \frac{m_f \lambda}{\Delta t_{\mathrm{SRD}}}, \tag{1.36}$$

where

$$\xi_E = \frac{8}{3} \left(2\pi \frac{M_c}{M_c + m_f} \right)^{1/2} \gamma \left(\frac{\sigma_{cf}}{a_0} \right)^2. \tag{1.37}$$

The other contribution comes from Stokes friction that derives from integrating the Stokes solution to the hydrodynamic field over the surface of the particle at $r = \sigma_{cf}$ [30]. The Stokes friction can be written as

$$\zeta_S = \frac{4\pi \eta \sigma_{cf}}{f(\sigma_{cf}/L)}, \tag{1.38}$$

where f is the correction factor that accounts for finite size effects. The factor f scales as

$$f(\sigma_{cf}/L) \approx 1 - 2.837 \frac{\sigma_{cf}}{L}. \tag{1.39}$$

Another way to express the Stokes friction coefficient is to use the analytical definition of viscosity given by $\eta = \nu \gamma m_f/a_0^3$ and to neglect the correction factor. This gives

$$\zeta_S = 4\pi \left(\frac{\nu_{kin} + \nu_{col}}{\nu_0} \right) \gamma \frac{\sigma_{cf}}{a_0} \frac{m_f \lambda}{\Delta t_{\mathrm{SRD}}} = \xi_S \frac{m_f \lambda}{\Delta t_{\mathrm{SRD}}}, \tag{1.40}$$

where

$$\xi_S = 4\pi \left(\frac{\nu_{kin} + \nu_{col}}{\nu_0} \right) \gamma \frac{\sigma_{cf}}{a_0}. \tag{1.41}$$

From Eqs. 1.37 and 1.41, the friction coefficient of the SRD fluid can be written as

$$\zeta_{\mathrm{SRD}} = \left(\frac{1}{\xi_S} + \frac{1}{\xi_E} \right)^{-1} \frac{m_f \lambda}{\Delta t_{\mathrm{SRD}}}. \tag{1.42}$$

Thus, the diffusion coefficient for a single colloid can now be written as

$$D_{\mathrm{SRD}} = \frac{k_B T}{\zeta} = \frac{1}{\xi} \frac{a_0^2}{t_0}, \tag{1.43}$$

where $\xi = (1/\xi_S + 1/\xi_E)^{-1}$. From the expression of diffusion, one has

$$\tau_D = \frac{a^2}{D_{\text{SRD}}} \approx \frac{\sigma_{cf}^2}{D_{\text{SRD}}} = \xi \left(\frac{\sigma_{cf}}{a_0} \right)^2 \frac{\Delta t_{\text{SRD}}}{\lambda}. \tag{1.44}$$

Finally, from τ_D, the corresponding Δt_{SRD} time step can be obtained using the equation:

$$\Delta t_{\text{SRD}} = \frac{\lambda \tau_D}{\xi} \left(\frac{a_0}{\sigma_{cf}} \right)^2. \tag{1.45}$$

A similar technique can be applied to map to other time scales. An example mapping to kinematic time scale is discussed in Ref. [30].

Since the length and times scales are rescaled in SRD-MD, other variables such as the temperature and energy are also rescaled. Similar to the transport coefficients, the actual temperature is mapped from experimental scale to SRD scale and vice versa. A system temperature of $T_0 = 293$ K is equivalent to an SRD temperature of

$$T_{\text{SRD}} = \frac{a_0^2 m_f}{k_B t_0^2}. \tag{1.46}$$

Consequently, the unit of energy is given by $k_B T_{\text{SRD}}$.

1.7   Summary

A brief summary of the different methods discussed in this chapter is given in Table 1.2. While each of these techniques have their own merits, the efficiency of a simulation method greatly depends on the problem in question. In most of the colloidal systems studied numerically, the two most relevant suspension properties that need proper modeling are Brownian motion and HIs. In this regard, it is important to note that BD is the fastest numerical tool available for systems where HIs can be ignored. In the same manner, SRD-MD remains as the simplest simulation technique for systems where HIs are significant. Moreover, the two methods can be simultaneously used to isolate the effects of HIs.

The next chapter deals with the calculation of the viscosity of sheared colloidal suspensions, which will serve as a validation of the effectiveness of the SRD-MD model described in this chapter.

Table 1.2:   Brief summary of mesoscopic simulation techniques

Model	Brownian motion	HIs	Type
standard BD	✓	✗	continuum-based
BD-YRP	✓	✓	continuum-based
DPD	✓	✓	particle-based
standard LB	✗	✓	lattice-based
FLB	✓	✓	lattice-based
SRD	✓	✓	particle-based

Chapter 2 :

Shear Viscosity

Calculating the shear viscosity of a suspension is a model problem for studying the rheological behaviour of mesoscopic systems [71, 72]. Specifically, there have been plenty of studies of suspension viscosity as a function of the particle concentration. It is a key parameter for investigating several experimental phenomena such as phase transitions and yield stress. Moreover, theoretical models for the behaviour of shear viscosity as a function of concentration are relatively well-known [9, 10, 73, 74] so that it can be used as a benchmark to validate an evolving numerical model. Once validated, one can easily shift to analyze the dependence of shear viscosity on other relevant variables such as shear rate, particle structure, Peclet number (Pe) and Reynolds number (Re).

The system used in the calculation of shear viscosity is based on hard-sphere colloids mainly because their properties are theoretically and numerically well-known as compared to systems with more complex interactions. While it has been shown in Ref. [31] that SRD-MD can be used to calculate viscosity using a DLVO description for colloid-colloid interactions, it is important to justify that the computation of shear viscosity using SRD-MD agrees with existing theoretical predictions and can reproduce results that are comparable with other simulation techniques. Every good numerical method should correctly reproduce the behaviour of the shear viscosity as a function of volume fraction. To do this, employing a hard-sphere description of the colloids is sufficient and more practical.

The objective of this chapter is to provide a quantitative test on the ability of SRD-MD to model HI's on colloidal suspensions by calculating its shear viscosity. Specifically, this chapter will demonstrate that SRD-MD can be used for both dilute and concentrated cases. The first step in doing this is to understand that there are two ways to calculate shear viscosity: the equilibrium approach and the non-equilbrium approach. From the name itself, the equilibrium approach is suited for liquids in equilibrium while the non-equilibrium approach is for liquids under shear. Both approaches require an expression for the *stress tensor* of the liquid, the main ingredient for the calculation of shear viscosity. The stress tensors and shear viscosities of pure fluids in equilibrium and non-equilibrium are presented first. The idea is then developed to accommodate the calculation of viscosity when there are embedded colloids. The calculated results are compared with known numerical results, theoretical predictions and experimental data.

2.1 System

The colloids to be modeled are silica particles with radius of $a = 300$ nm, density of $\rho_c = 2200$ kg·m^{-3} and mass of $M = 2.49 \times 10^{-16}$ kg. From these given colloidal properties and from the information provided in Secs. 1.5 and 1.6, the corresponding parameters of the SRD fluid are derived. The SRD parameters used in this chapter are listed in Table

Table 2.1: Parameters used in the calculation of shear viscosity for the pure fluid case

a	300 nm	m_f	6.75×10^{-19} kg
a_0	150 nm	Δt_{SRD}	7.37×10^{-5} s
α	90°	T_{SRD}	2.02×10^{-3} K
λ	0.1	L	$32a_0$
γ	5	$\dot{\gamma}$	100 s^{-1}

2.1.

The mass and size of alumina colloids are used here only to set the scale of these quantities. However, since the objective is to compare the calculated results with known results for hard spheres, the colloids will not interact by the DLVO potential for alumina in water, but by a potential which resembles a hard-sphere interaction. For a purely repulsive system, the inverse power potential (IP-12) that appears in Eqs. 1.30 and 1.31 is utilized:

$$U_{ij}(r) = \begin{cases} \varepsilon \left(\frac{\sigma}{r}\right)^{12} & \text{for } r \leq 2.5\sigma; \\ 0 & \text{for } r > 2.5\sigma, \end{cases} \tag{2.1}$$

where $\varepsilon = \varepsilon_{cc} = \varepsilon_{cf} = 2.5k_BT$, $\sigma_{cc} = 2a$ and $\sigma_{cf} = 0.8a$.

Note that the diffusion time $\tau_D = a^2/D_0 = 0.12$ s is used. The corresponding time step is $\Delta t_{\text{SRD}} = 7.37 \times 10^{-5}$ s. This is obtained by using the viscosity of water $\eta_{\text{H}_2\text{O}} = 0.001$ Pa·s and the diffusion coefficient of a colloid in water $D_0 = k_BT/(6\pi\eta_{\text{H}_2\text{O}}a) = 7.15 \times 10^{-13}$ m^2 s^{-1}. If instead the kinetic time scale is used, the resulting unit of time is $\Delta t_{\text{SRD}} = 1.12 \times 10^{-9}$ s. Hence the option to map in diffusion time significantly reduces the computation time by up to 10^4.

The initial velocities of the particles obey a Maxwell-Boltzmann distribution and are allowed to evolve using SRD and MD algorithms. When shear is applied however, the infinite periodic system is subjected to a uniform shear in the xy plane using LEBC. Shear is applied in the y direction and the gradient is along the x direction. The shear rate is defined as

$$\dot{\gamma} = \frac{\Delta v_y}{\Delta x}, \tag{2.2}$$

where Δv_y is the shear velocity.

For the molecular dynamics part, the value of Δt_{MD} is smaller than Δt_{SRD} and generally depends on the steepness of the potential. It was found that $\Delta t_{\text{MD}} = \Delta t_{\text{SRD}}/8$ is sufficient to resolve the correct Newtonian dynamics for the IP potential used in this chapter. Moreover, similar Δt_{MD} is used in Refs. [63, 75].

2.2 Shear viscosity of pure fluids

Before calculating the shear viscosity of colloidal suspensions, it is first important to understand the calculation of the shear viscosity of pure fluids. The pure fluid case can serve as a testing ground and the principles applied in this simpler case can be extended once the colloids are embedded in the suspension. To perform the equilibrium approach, the Green-Kubo [76, 77] relation must be employed [25]. On the other hand, to perform the non-equilibrium approach, linear response theory must be used [2]. Both approaches require an expression for the stress tensor of the liquid.

The stress tensor contains the information on how momentum transport occurs in the liquid. Momentum transfer can be imparted in two ways, which correspond to the two steps of the SRD algorithm. During the streaming step, momentum is carried by the individual particles in its direction of motion. This corresponds to the *kinetic contribution* to the stress tensor. On the other hand, during the collision step, momentum is redistributed among the particles in the collision cell and this corresponds to the *collisional contribution* to the stress tensor. Mathematically, this can be expressed as

$$\sigma_{xy}^{\text{tot}} = \sigma_{xy}^{\text{kin}} + \sigma_{xy}^{\text{col}}. \tag{2.3}$$

Note that the stress tensors presented in this work can always be divided in this manner.

2.2.1 Equilibrium approach

Green [76] and Kubo [77] showed that the flow of mass, momentum and energy can be expressed in terms of the decay of equilibrium fluctuations of velocity, momentum and heat flux respectively [62]. In other words, the transport coefficients, which include mass, diffusivity, viscosity and conductivity can be obtained from autocorrelation coefficients of certain phase functions. Mori and Zwanzig [78, 79, 80] developed the projection operator formalism for deriving the Green-Kubo relations for transport coefficients for MD fluids, from which the Green-Kubo relations for SRD fluids can be derived. For viscosity, the corresponding phase function is the stress tensor. Following the derivation by Malevanets and Kapral, this is given by [25, 29]:

$$\sigma_{xy}^{\text{tot}} = \sum_i \left(m_f v_{ix} v_{iy} + \frac{m_f}{\Delta t_{\text{SRD}}} v_{ix} B_{iy} \right), \tag{2.4}$$

where

$$B_{iy} = [\xi_{iy}^s(t + \Delta t_{\text{SRD}}) - \xi_{iy}^s(t)] - \Delta t_{\text{SRD}} v_{iy}(t), \tag{2.5}$$

and ξ_{iy}^s is the shifted cell coordinate due to the grid-shift procedure. Eq. (2.5) represents the difference between the shifted cell coordinate of particle i from $\xi_{iy}^s(t)$ to $\xi_{iy}^s(t + \Delta t_{\text{SRD}})$ during one streaming step and the actual distance traveled by the particle $\Delta t_{\text{SRD}} v_{jy}(t)$. The Green-Kubo relations for SRD are different from the MD versions because of the underlying cell structure and multiparticle interactions. For comparison, the corresponding stress tensor for molecular fluids is given by [27, 29]

$$\sigma_{xy}^{\text{tot}} = \sum_i \delta(\mathbf{r} - \mathbf{r}_i) \left(m v_{ix} v_{iy} + \frac{1}{2} \sum_{j \neq i} r_{ijx} F_{ijy}(\mathbf{r}_{ij}) \right). \tag{2.6}$$

For both Eqs. 2.4 and 2.6, the first terms are the kinetic contributions while the second terms are the collisional contributions. It can be noticed that the kinetic part is the same but the collisional part is different. This is because unlike the force definition of molecular fluid i.e. $F_{ijy}(\mathbf{r}_{ij})$, the force in the SRD fluid is $m v_{ix}/\Delta t_{\text{SRD}}$, which corresponds to a non-local force at the cellular-level that only acts at discrete time intervals Δt_{SRD}.

The numerical calculation of shear viscosity can therefore be obtained by integrating the autocorrelation function of Eq. (2.4). An example formulation is given in Ref. [27]:

$$\eta_0 = \lim_{t \to \infty} \frac{V}{k_B T} \int_0^t dt' \langle \sigma_{xy}^{\text{tot}}(t') \sigma_{xy}^{\text{tot}}(0) \rangle. \tag{2.7}$$

Malevanets and Kapral also calculated an analytical expression for the shear viscosity of a pure fluid. This was achieved by using Chapman-Enskog expansion to map the simulation equations onto the Navier-Stokes equation. By using the following values $\alpha = 90°$, $\lambda = 1$ and $\Delta t_{\text{SRD}} = 1$ for the rotation angle, dimensionless mean-free path and time step respectively, the resulting equation presented in Ref. [25] has the form:

$$\eta_0 = \frac{\gamma k_B T}{6} \frac{3(1 - e^{-\gamma}) + 2\gamma}{[e^{-\gamma} - (1 - \gamma)]}, \tag{2.8}$$

where η_0 is the shear viscosity of the SRD fluid. This equation shows the dependence of shear viscosity on the density of fluid particles per cell γ. Note that in general, the shear viscosity of the SRD fluid depends on the SRD parameters, which will be more apparent in the succeeding sections.

2.2.2   Non-equilibrium approach

While the use of Green-Kubo relation is more common for pure fluids and is the original approach used by Malevanets and Kapral [25], the non-equilibrium approach by Kikuchi et al. [2] is an alternative method that allows the study over a wide parameter range of shear magnitudes. Moreover, the equilibrium approach is prone to fluctuations and

has poor statistics so that long simulation times and averaging over several independent simulations are required for accurate shear viscosity calculations [27]. It is important to note these fluctuation effects since they could lead to even longer computation times once colloids are embedded in the fluid. The stress autocorrelation function can be defined as:

$$\sigma_{xy} = \eta_0 \dot{\gamma}. \tag{2.9}$$

So that obtaining η_0 is straight-forward once an expression for σ_{xy} is known. The applied shear $\dot{\gamma}$ results to a shear gradient of $\partial u_x / \partial y$. Kikuchi et al. have shown that the stress tensor can be derived and has the form:

$$\sigma_{xy} = \frac{m_f \gamma}{a_0^3} \left(\frac{\dot{\gamma} \Delta t_{\text{SRD}}}{2} \langle v_y^2 \rangle - \langle v_x v_y \rangle \right), \tag{2.10}$$

where the averaging is done over the steady-state velocity probability distribution function of the fluid particles $P(v_x, v_y)$. It is also important to emphasize that P is not Maxwellian since in the non-equilibrium steady state, shear induces correlations between v_x and v_y [29]. Hence the autocorrelation function does not decay to zero.

Eq. (2.10) can be evaluated by separating the effects of the kinetic and collision part. For the kinetic part, it can be shown that after the streaming step, the second term reduces to

$$\langle v_x v_y \rangle^{after} = \langle v_x v_y \rangle - \dot{\gamma} \Delta t_{\text{SRD}} \langle v_y^2 \rangle. \tag{2.11}$$

For the collision part, the momentum is redistributed among the particles and the averaging is done over the rotation matrix. The corresponding term is

$$\langle v_x v_y \rangle^{after} = f \langle v_x v_y \rangle^{before}, \tag{2.12}$$

where f is given by

$$f = \left\{ 1 - \frac{\gamma - 1 + e^{-\gamma}}{\gamma} [1 - \cos(2\alpha)] \right\}. \tag{2.13}$$

Combining Eqs. 2.12 and 2.13 yields:

$$\left(\langle v_x v_y \rangle - \dot{\gamma} \Delta t_{\text{SRD}} \langle v_y^2 \rangle \right) f = \langle v_x v_y \rangle \tag{2.14}$$

$$\langle v_x v_y \rangle = \dot{\gamma} \Delta t_{\text{SRD}} \langle v_y \rangle^2 \frac{f}{1 - f}. \tag{2.15}$$

Using Eq. (2.10) and assuming equipartition of energy $\langle v_y \rangle^2 = k_B T / m_f$, the total stress tensor can be expressed as:

$$\sigma_{xy}^{\text{tot}} = \frac{\dot{\gamma} \gamma \Delta t_{\text{SRD}} k_B T}{m_f} \left(\frac{1}{2} + \frac{f}{1 - f} \right). \tag{2.16}$$

In 2D, the kinetic component of the shear viscosity from Eq. (2.16) reduces to Eq. (2.8) for $\alpha = 90°$ and $\Delta t_{\text{SRD}} = 1$. Hence the analytical results of both the equilibrium [25] and non-equilibrium [2] approach are consistent.

Since these results are for the pure fluid case, the measured viscosity is independent of the shear rate. However, for very low shear rates, there can be some deviations due to statistical errors since the applied perturbation is small. On the other end, high shear rates can lead to finite size effects. This happens when the distance traveled by the walls in the LEBC approach the size of the system [2].

For "gas-like" systems i.e. $\lambda > a_0/2$, the collisional contribution of the viscosity is negligible and the shear viscosity is dominated by the kinetic contribution. Inversely, for "liquid-like" systems i.e. $\lambda << a_0/2$, the shear viscosity is dominated by the collisional contribution and the kinetic part is very small.

2.2.3 Winkler's formulation

2.2.3.1 Equilibrium case

Winkler and Huang in Ref. [50] have independently derived the stress tensor for SRD-MD, both for the equilibrium and non-equilibrium cases. This is briefly described in this section. Starting with Newton's equation of motion:

$$m_f \frac{\partial^2 r_i}{\partial t^2} = F_i, \tag{2.17}$$

where r_i is the position of the particle in an infinite system without accounting for the mirror images. If a shear velocity along the y axis and a gradient along the x axis are used, multiplying Eq. (2.17) by r_i and summing over all fluid particles N_f yields,

$$\frac{d}{dt} \sum_{i=1}^{N_f} m_f v_{iy} r_{ix} = \sum_{i=1}^{N_f} m_f v_{iy} v_{ix} + \sum_{i=1}^{N_f} F_{iy} r_{ix}. \tag{2.18}$$

When averaged over time, Eq. (2.18) leads to

$$\left\langle \sum_{i=1}^{N_f} m_f v_{iy} v_{ix} \right\rangle + \left\langle \sum_{i=1}^{N_f} F_{iy} r_{ix} \right\rangle = 0. \tag{2.19}$$

Expanding the second term in Eq. (2.19),

$$\langle F_{iy} r_{ix} \rangle = \lim_{t \to \infty} \frac{1}{t} \int_0^t F_{iy}(t') r_{ix}(t') dt'. \tag{2.20}$$

where t is the total elapsed time. As mentioned in Sec 2.2.1, the collision algorithm results to a pseudo-force, which is obtained from the change in the momentum during the collision step at discrete time intervals. This can be rewritten as

$$F_i(t) = \sum_{q=0}^{\infty} m_f \Delta v_{iy}(t) \delta(t - t_q). \tag{2.21}$$

Using the definition for the time average:

$$\langle ... \rangle_T = \lim_{N \to \infty} \langle ... \rangle_N = \lim_{N \to \infty} \frac{1}{N} \sum_{q=1}^{N}, \tag{2.22}$$

Eq. (2.20) can now be written as

$$
\begin{aligned}
\langle F_{iy} r_{ix} \rangle & = \lim_{N \to \infty} \frac{1}{N} \sum_{q=1}^{N} \frac{1}{\Delta t_{\text{SRD}}} \int_{t_q - \Delta t_{\text{SRD}}}^{t_q} m_f \Delta v_{iy}(t') r_{ix}(t') \delta(t' - t_q) dt' \\
& = \lim_{N \to \infty} \frac{m_f}{N \Delta t_{\text{SRD}}} \sum_{q=1}^{N} \Delta v_{iy}(t_q) r_{ix}(t_q),
\end{aligned}
\tag{2.23}
$$

where N is the total number of time steps. When periodic boundary conditions are taken into account, the positions r_i is written as

$$r_i(t) = r_i'(t) + R_i(t), \tag{2.24}$$

where r_i' is the mirror image of r_i and R_i is the lattice vector at time t. Incorporating this expansion in Eq. (2.23), one obtains:

$$
\begin{aligned}
\langle F_{iy} r_{ix} \rangle & = \lim_{N \to \infty} \frac{m_f}{N \Delta t_{\text{SRD}}} \sum_{q=1}^{N} [\Delta v_{iy}(t_q) r_{ix}'(t_q) + \Delta v_{iy}(t_q) R_{ix}(t_q)] \\
& = \frac{m_f}{\Delta t_{\text{SRD}}} \langle \Delta v_{iy}(t_q) r_{ix}'(t_q) + \Delta v_{iy}(t_q) R_{ix}(t_q) \rangle_T.
\end{aligned}
\tag{2.25}
$$
$$\tag{2.26}$$

Now that the forces of the system are properly represented, the stress tensor can be obtained by using the mechanical definition of stress

$$\sigma_{xy} = \frac{F_y}{A_x} \tag{2.27}$$

where F_y is the total force in the direction y across a surface A_x that is normal to the x direction. Notice that Eq. (2.25) has two parts. The first term is the instantaneous internal stress tensor and the second term is the instantaneous external stress tensor. The

derivation provided in Ref. [50] showed that these two terms can be reduced to:

$$\sigma_{xy}^{int} = -\frac{m_f}{V} \sum_{i=1}^{N_f} \hat{v}_{ix}\hat{v}_{iy} - \frac{m_f}{V\Delta t_{\text{SRD}}} \sum_{i=1}^{N_f} \Delta v_{iy} r'_{ix}, \qquad (2.28)$$

and

$$\sigma_{xy}^{ext} = \frac{m_f}{V\Delta t_{\text{SRD}}} \sum_{i=1}^{N_f} \Delta v_{ix} R_{ix}, \qquad (2.29)$$

respectively. Moreover, the time averages of Eqs. 2.28 and 2.29 are shown to be equal: $\sigma_{xy}^{ext} = \sigma_{xy}^{int}$ in Ref. [50]. In this work, the internal stress tensor is used for the system since its expression is more complete i.e. it consists of both the kinetic and collisional parts [50].

2.2.3.2 Non-equilibrium case

The derivation of the stress tensor for systems in equilibrium can be extended to incorporate LEBC. When shear is imposed, an additional term $d(\dot{\gamma} r_{ix})/dt = \dot{\gamma} v_{ix}$ is added on both sides of Eq. (2.18). Hence

$$\frac{d}{dt} \sum_{i=1}^{N_f} m_f(v_{iy} - \dot{\gamma} r_{ix})r_{ix} = \sum_{i=1}^{N_f} m_f(v_{iy} - \dot{\gamma} r_{ix})v_{ix} + \sum_{i=1}^{N_f} F_{iy}r_{ix} - \dot{\gamma}\sum_{i=1}^{N_f} m_f v_{ix}r_{ix}. \qquad (2.30)$$

Similar to the periodic boundary conditions, the time average of the derivative on the left hand side reduces to zero. Following the same procedures as above, the time average of the remaining terms can be written as

$$\langle (v_{iy} - \dot{\gamma} r_{ix})v_{ix}\rangle_T = \langle \hat{v}_{ix}\hat{v}'_{iy}\rangle_T + \frac{\dot{\gamma}\Delta t_{\text{SRD}}}{2} \langle \hat{v}_{ix}\rangle_T. \qquad (2.31)$$

The internal stress tensor is given by

$$\sigma_{xy}^{int} = -\frac{m_f}{V} \sum_{i=1}^{N_f} \hat{v}'_{ix}\hat{v}_{iy} - \frac{m_f}{V\Delta t_{\text{SRD}}} \sum_{i=1}^{N_f} \Delta v_{iy} r'_{ix} - \frac{\dot{\gamma} m_f \Delta t_{\text{SRD}}}{2V} \sum_{i=1}^{N_f} v_{ix}^2 \qquad (2.32)$$

where the ($'$) symbol correponds to quantities that are measured after LEBC are imposed, $\hat{v}_\alpha = v_\alpha(t - \Delta t)$ and $\Delta v_{iy} = (v_{iy} - \hat{v}_{iy})$ are also used. By separating the kinetic and
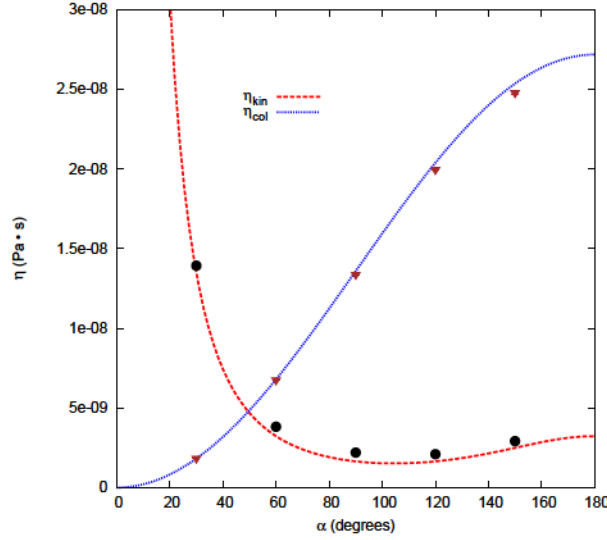
Figure 2.1: Simulated kinetic (η_{kin}) and collisional (η_{col}) viscosities for the pure-fluid case as a function of the SRD angle α superimposed against Eqs. (2.35) and (2.36).

collisional contributions, one obtains:

$$
\sigma_{\text{kin},yx} = -\frac{m_f}{V}\sum_{i=1}^{N_f}\hat{v}'_{iy}\hat{v}_{ix} - \frac{m_f\dot{\gamma}\Delta t_{\text{SRD}}}{2V}\sum_{i=1}^{N_f}v_{ix}^2 \text{ and} \tag{2.33}
$$

$$
\sigma_{\text{col},yx} = -\frac{m_f}{V\Delta t_{\text{SRD}}}\sum_{i=1}^{N_f}\Delta v_{iy}r'_{ix}, \tag{2.34}
$$

Note that r'_{ix} is measured after the grid-shifting algorithm is imposed. From Eq. (2.34), numerical values of shear viscosity can therefore be obtained by simply using $\eta_0 = \langle\sigma_{xy}^{\text{tot}}\rangle/\dot{\gamma}$.

The results presented by Winkler and Huang were also shown to agree with Kikuchi's previous results [50]. A more detailed derivation of the analytical results is shown in the paper. The shear viscosity for pure fluid is defined as a function of SRD parameters and is given by:

$$
\eta_{\text{kin}} = \frac{5\gamma^2 k_1}{(\gamma - 1 + e^{-\gamma})(4 - 2\cos\alpha - 2\cos 2\alpha)} - \frac{1}{2}\gamma k_1 \quad, \tag{2.35}
$$

$$
\eta_{\text{col}} = k_2(1 - \cos\alpha)(\gamma - 1 + e^{-\gamma}), \tag{2.36}
$$

where $k_1 = k_B T\Delta t_{\text{SRD}}/a_0^3$, $k_2 = m/(12a\Delta t_{\text{SRD}})$ and $\eta_0 = \eta_{\text{kin}} + \eta_{\text{col}}$.

The results obtained using Winkler's formulation are shown in Fig. 2.1. Since a small value for $\lambda = 0.1$ is used, the viscosity is dominated by the momentum transfer from particle collisions and not from the streaming of the fluid. This is similar to Malevanets and Kikuchi's results. Fig. 2.1 also validates the use of diffusion time scale for mapping since the same agreement should be obtained for any time scale used. At $\alpha = 90°$, the

viscosity is 1.5×10^{-8} Pa $\cdot$ s. The same value of shear viscosity is obtained using the approaches of Malevanets and Kapral [25] and Kikuchi and Huang [2]. The viscosity remains constant between 50 s^{-1} and 100 s^{-1}. Note that if the SRD parameters are mapped to the kinematic time scale τ_ν instead of the diffusion time scale τ_D, then the actual viscosity of water $\eta = 0.001$ Pa $\cdot$ s will be reproduced.

A small deviation from the theoretical values is seen at higher angles (120°-150°). A similar observation is also found when the method proposed in Ref. [2] is used. This small deviation may be due to (1) the increase in the number of degrees of freedom and (2) the small effect of the coarse-grained temperature (2.02×10^{-3} K). This may lead to a small loss of molecular chaos at low temperatures (see Ref. [2]).

2.3 Embedded colloids

2.3.1 Analytical method

The volume fraction of the colloids can be divided into three different regimes [81].

- **Dilute regime** that is below $\phi \approx 0.10$ [82, 83, 84]. In this regime HIs are negligible and the shear viscosity is linear. For this regime, Einstein's equation [9, 10] given by

$$\eta_r = 1 + 2.5\phi \ \text{ for } \phi \to 0, \tag{2.37}$$

is used to describe the shear viscosity.

- **Semi-dilute regime** that is below $\phi \approx 0.25$ where the shear viscosity is still approximately linear but starts to exhibit a higher dependence on ϕ. For this regime, a polynomial expansion is used to approximate the shear viscosity:

$$\eta_r = 1 + 2.5\phi + B_1\phi^2 \tag{2.38}$$

where B_1 is between 7.35 and 14.1 [85, 86, 87]. In this regime, the fitting with experimental results are often poor because Eq. (2.38) predicts a finite value of shear viscosity as $\phi \to 1$, while in actual systems, the viscosity becomes infinite when approaching the maximum packing fraction of $\phi_m = 0.74$ [81].

- **Concentrated regime** usually starts at $\phi > 0.25$ and a rapid power law deviation from the the linear expression (Eq. (2.37)) is observed. For this regime, Krieger's semi-empirical equation is used.

$$\eta_r = \left(1 - \frac{\phi}{\phi_m}\right)^{-p} \ \text{ for } \phi \to \phi_m, \tag{2.39}$$

where p is a parameter that depends on ϕ_m and the shear. The deviation from the linear approximation is due to the increase of the probability of collisions and because HIs become more significant at higher volume fractions [72].

2.3.2 Numerical method

When a shear rate of $\dot{\gamma} = 100$ s^{-1} is introduced, the Peclet number of the sytem becomes Pe $= 12.6$. Viscosity is measured when the velocity profile is already linear. Fig. 2.2 shows the velocity profile inside a simulation box for a suspension with $\dot{\gamma} = 100$ s^{-1} and $\phi = 0.1534$. It can be observed that the system starts with a flat velocity profile that corresponds to the initial Maxwell-Boltzmann distribution and then it gradually increases until a planar Couette flow is modeled.

An equilibration part consisting of $2000 - 6000$ SRD steps is first carried out. This is the part where $\mathcal{T}$ is slowly driven to the desired T_{SRD}. This approach is needed to ensure that the viscosities are measured with the correct linear velocity profile and at the correct system temperature.

When colloids are embedded in the the fluid, the volume fraction occupied by the colloid can be defined as

$$\phi = \frac{N_c}{L^3} \frac{4}{3} \pi r_H{}^3 \tag{2.40}$$

where N_c is the number of embedded colloids and r_H is the hydrodynamic radius. This is equal to the hard-sphere radius a_{hs} only in the ideal case when there is no explicit fluid present. Table 2.2 summarizes the number of colloids and fluid particles used for each volume fraction. Analytical approaches to calculate viscosity often deal with ideal
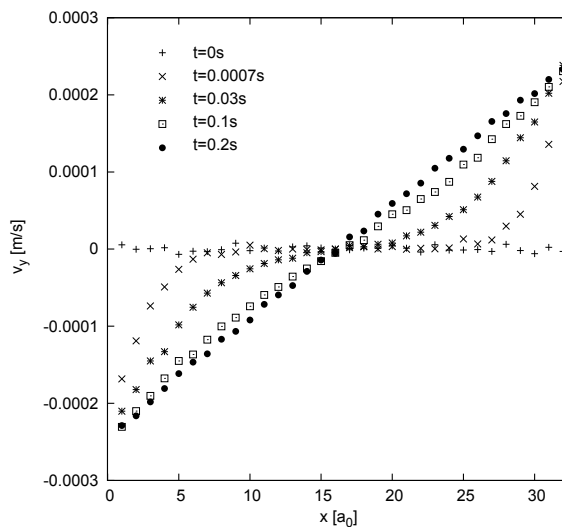

Figure 2.2: Velocity profile for $\phi = 0.1534$ and a shear rate of $\dot{\gamma} = 100$ s^{-1}. A linear profile is observed at 0.2 s.

Table 2.2: Number of colloids N_c and fluid particles N_f corresponding to each volume fractions used in the simulation. These are obtained with $L = 32a_0$ and $a_{hs} = \sigma_{cf} = 0.8a$ in Eq.(2.40).

ϕ	N_c	N_f	ϕ	N_c	N_f
0.0513	98	155433	0.2356	450	125236
0.1026	196	147026	0.2618	500	120947
0.1534	293	138705	0.2880	550	116657
0.1791	342	134501	0.3142	600	112368
0.2053	392	130212	0.3388	647	108336

systems, where a_{hs} is well defined. However, defining r_H is difficult in simulations and experiments. A hard-sphere approximation requires an inverse-power potential with $n \to \infty$ in Eq. (1.31) instead of $n = 12$. Hence a larger n will require a smaller Δt_{SRD}, which will result to a more expensive calculation. Moreover, the effective r_H for SRD-MD is dependent on several factors including length scale and shear. This is discussed in Refs. [30, 88] for slip boundary conditions at the colloid-fluid interface. Experimental measurements of ϕ are not simple either. Ref. [89] provides an extensive review on the difficulties encountered when measuring ϕ in hard-sphere colloids and the unavoidable uncertainties associated with its reported value. To this point, there are two defined radii in the implementation of SRD-MD: $\sigma_{cc}/2 = a$ for the colloid-colloid interaction and $\sigma_{cf} = 0.8a$ for the colloid-fluid interaction. In this study, Eq. (2.40) is evaluated using σ_{cf} because it is the best r_H approximation for the simulations [30]. The treatment of volume
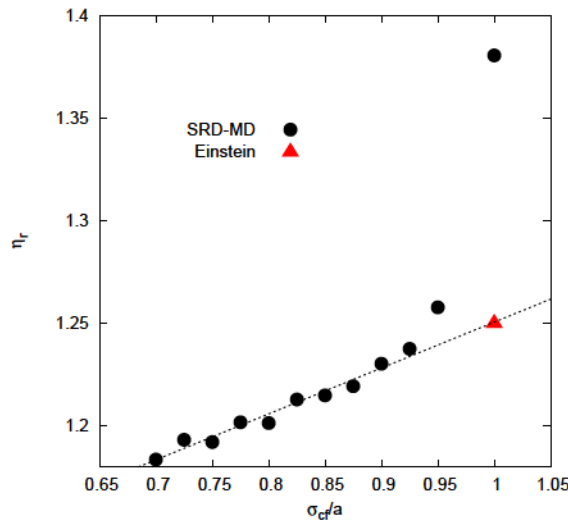

Figure 2.3: Dependence of shear viscosity η_r on the interaction parameter σ_{cf} for $N_c = 98$. As $\sigma_{cf} \to a$, the viscosity approaches the theoretical value predicted by the Einstein equation ($\eta_r = 1.25$), except very close to a, where depletion attraction causes an increasing deviation. The line is a guide to the eyes.

fraction is similar to the definition used in Ref. [88] for colloid sedimentation viscosity, where the volume fraction is defined using r_H instead of σ_{cc}. This is equivalent to viewing the volume fraction from the fluid particle's point of view instead of the colloid's point of view. Fig. 2.3 shows how shear viscosity increases with increasing value of σ_{cf}. The predicted value using Eq. (2.37) is also shown for comparison. As σ_{cf} approaches a_c, the calculated shear viscosity moves closer to the analytical result. However, in the limit $\sigma_{cf} \to a$ depletion attraction starts to occur and the calculated viscosity in this region ($\backsim 0.95a$) is no longer valid. Cluster formation caused by the depletion attraction is observed when $\sigma_{cf} = a$ but are eliminated when $\sigma_{cf} = 0.8a$. The result of Fig. 2.3 justifies the choice of using σ_{cf} as the hydrodynamic radius in Eq. (2.40).

2.3.3 Stress Tensors

Since the simulations of the pure fluid case are in good agreement with analytical equations, the above approach can be generalized to obtain the shear viscosity of colloidal suspensions. The equivalent stress tensor for the embedded colloids is given by [90]

$$
\begin{aligned}
\sigma_{yx}^{\text{colloid}} &= -\frac{M_c}{V} \sum_{i=1}^{N_c} \hat{v}'_{iy} \hat{v}_{ix} - \frac{M_c \dot{\gamma} \Delta t_{\text{SRD}}}{2V} \sum_{i=1}^{N_c} v_{ix}^2 \\
&\quad - \frac{1}{V} \sum_{i=1}^{N_c} F_{iy} r'_{ix}.
\end{aligned}
\tag{2.41}
$$

Since the coupling method used in this paper is MD, the colloid forces are explicitly defined. Using Eq. (1.31), F_{iy} is obtained directly from $\partial (V_{cc,i} + V_{cf,i}) / \partial r_y$ instead of the pseudo force $\Delta v_{i,y}$ used in Eq.(2.34). The total stress tensor of the suspension is calculated from the sum of the contributions from the embedded colloids and suspending fluid:

$$
\sigma_{yx}^s = \sigma_{yx}^{\text{fluid}} + \sigma_{yx}^{\text{colloid}},
\tag{2.42}
$$

which is also individually divided into the kinetic and collisional contributions. For the contribution of the embedded colloids, the stress tensor is divided as follows.

$$
\sigma_{yx}^{\text{kin}} = -\frac{M_c}{V} \sum_{i=1}^{N_c} \hat{v}'_{iy} \hat{v}_{ix} - \frac{M_c \dot{\gamma} \Delta t_{\text{SRD}}}{2V} \sum_{i=1}^{N_c} v_{ix}^2
\tag{2.43}
$$

$$
\sigma_{yx}^{\text{col}} = -\frac{1}{V} \sum_{i=1}^{N_c} F_{iy} r'_{ix}.
\tag{2.44}
$$

An example stress tensor is provided in Figs. 2.4 and 2.5. The behavior is similar to the one presented by Winkler and Huang i.e. huge fluctuations occur at the beginning

until steady-state is achieved. Similar to the stress tensors derived by Kikuchi [2], the steady state values of the stress tensors derived in this section do not decay to zero.

2.4 Shear Viscosity

An advantage of the stress tensor utilized in this work is that it can be divided into components thus allowing better characterization. The total viscosity is given by

$$\eta^{\text{total}} = \eta^{\text{colloid}} + \eta^{\text{fluid}}, \tag{2.45}$$

where each component has a virial form i.e. they are divided into kinetic and collisional parts. The shear viscosity of the colloids (η^{colloid}) can also be divided into components owing to the different contributions to the stress tensor. The collisional part, described by Eq. (2.44) and represented by blue diamonds in Fig. 2.6, increases because of the increase in the probability of collisions among other colloids when the volume fraction increases. It is also the most dominant contribution to the overall viscosity. The kinetic contribution, described by Eq. (2.43), is represented by red squares in Fig. 2.6. It represents the pressure exerted by the colloids on a surface. As expected, it increases with increasing volume fraction. However, it is smaller in comparison to the contribution from the colloid-colloid interactions. The shear viscosity from the colloid is therefore dominated by the momentum exchanges from inter-particle interactions rather than from streaming.

The same treatment is used to analyze what is happening to the shear viscosity of the SRD fluid (η^{fluid}) as the volume fraction increases (see Fig. 2.7). The total shear viscosity (black circles) is comprised of the kinetic part (red squares) and collisional part (blue diamonds). For the collisional contribution, which describes the collisions among fluid particles, no significant change can be observed. In contrast, the kinetic contribution, which describes the streaming of the fluid particles, increases by $\Delta = 2.7 \times 10^{-9}$ Pa·s when colloids are present. This is due to the additional momentum imparted by the fluid-colloid interactions when streaming.

Finally, by summing all the shear viscosity components, a comparison of the suspension viscosity with other known results is produced. The SRD-MD data points are represented by the blue circles in Fig. 2.8. For the experimental part, we compared with the data by Segré [6] and van der Werff [7], where they used undeformable, sterically stabilized spheres. The volume fraction is approximated using the maximum packing fraction of the system, $\phi_m = 0.494$ for Segré [6] and $\phi_m = 0.63$ for van der Werff [7]. It can be observed that our numerical results lie a little below the experimental data of Refs. [6, 7], which are represented by pink triangles and asterisks respectively. This can be due to finite
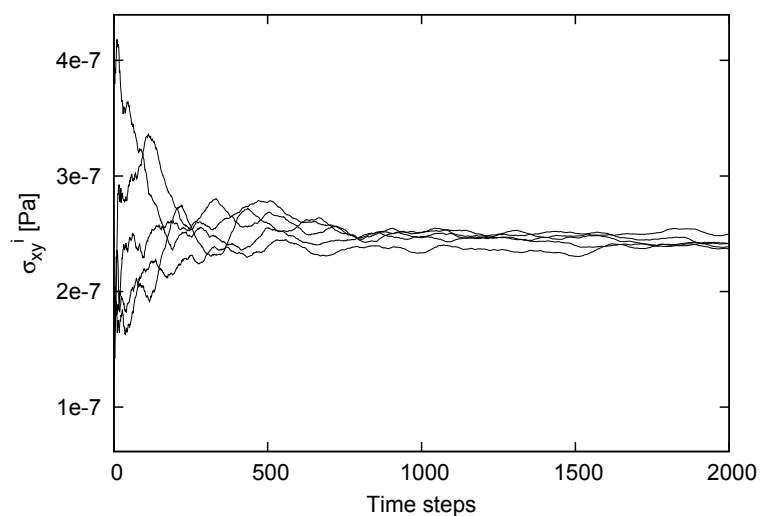
Figure 2.4: $\frac{m_f}{V}\hat{v}'_{iy}\hat{v}_{ix}$ component of the internal stress tensor for $\phi = 3.14\%$ and $\dot{\gamma} = 100\text{s}^{-1}$ from five different initial configurations.

Figure 2.5: $\frac{M_c}{V}\hat{v}'_{iy}\hat{v}_{ix}$ component of the internal stress tensor for $\phi = 3.14\%$ and $\dot{\gamma} = 100\text{s}^{-1}$ from five different initial configurations.
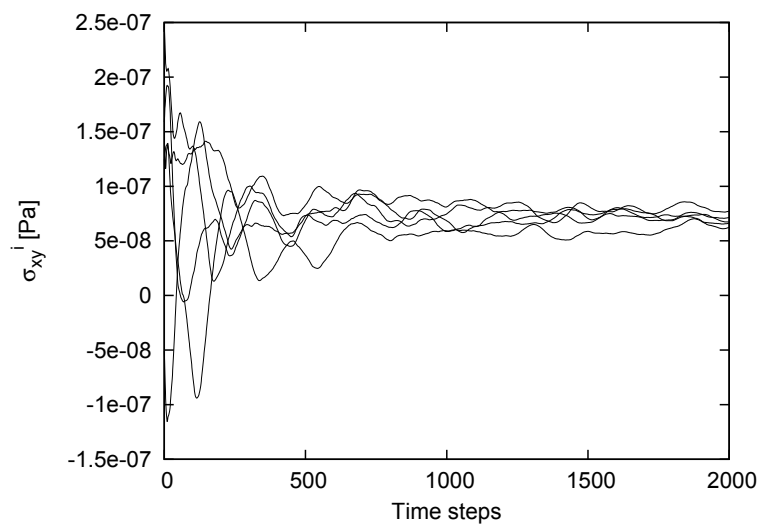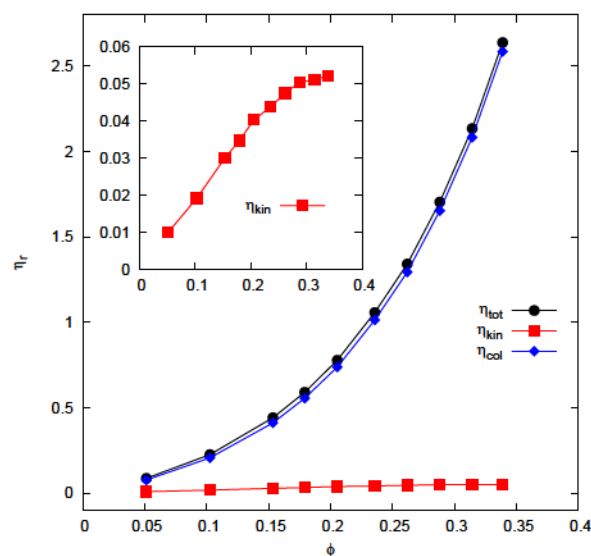
Figure 2.6: The shear viscosity contribution from the colloids η^{colloid} (black circles) is comprised of the kinetic part (red squares) and the collisional part (blue diamonds).
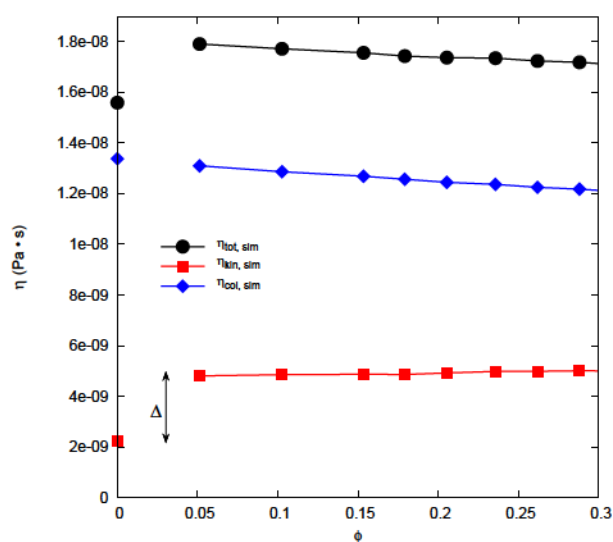

Figure 2.7: The shear viscosity contribution of the SRD fluid η^{fluid} is comprised of the kinetic viscosity (red squares) and collisional viscosity (blue diamonds). The viscosity of the SRD fluid ($\eta^{\text{fluid}}(\phi)$) with the predicted shear viscosity for the pure fluid case ($\eta^{\text{fluid}}(\phi = 0)$) given by Eq.(2.35) and (2.36) from Refs. [1, 2] are also compared. An average difference of $\Delta = 2.7 \times 10^{-9}$ Pa·s is measured.

size effects that make the shear rate higher than the expected value, thus decreasing the magnitude of viscosity [31].

The results shown are comparable with those of Koelman and Hoogerbrugge [4, 5], where they simulated hard-sphere suspensions under shear flow using DPD. These are represented by the hollow triangles. The hard-sphere case is imposed by using the moment of inertia and Euler's equation of motion for rigid bodies [5].

The behaviour of hard-sphere suspensions in the absence of HIs was analyzed using BD in Ref. [3]. The BD data points are represented by the green diamonds. In order to remove Pe and volume fraction dependencies of the shear viscosity, Ref. [3] employed an algorithm, in which after the Brownian position updates, the overlaps are checked and successively removed [91]. By comparing the behaviour of the two systems, HI's increase the viscosity of the suspension. In contrast to the BD simulations, where the effects of fluid particles are represented by the frictional and stochastic terms, the fluid description in SRD-MD is more explicit. It is observed that the overall contribution of the fluid decreases with increasing volume fraction since the number of fluid particles decreases with increasing concentration to maintain a constant Sc for the fluid. Even so, the treatment of the fluid by SRD-MD provides lubrication between colloid particles because the fluid can slide between them. This increases the chances of collisions among colloids and the overall friction of the system.

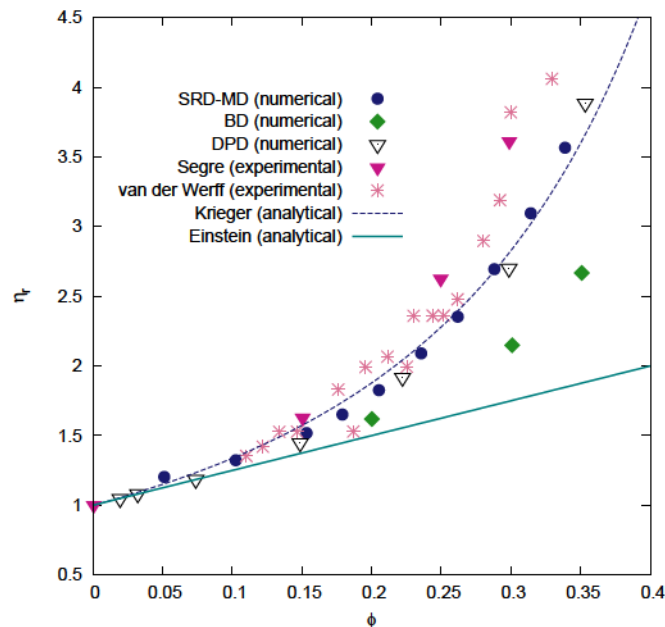From the theoretical standpoint, the results follow Eq. (2.37) (green solid line) for low

Figure 2.8: Relative shear viscosity of the colloidal suspension as a function of volume fraction compared with other numerical [3, 4, 5], experimental [6, 7] and analytical studies [8, 9, 10].

volume fractions and start to diverge near $\phi = 0.15$. For Eq. (2.39) (blue dashed line), a fitting parameter of $\phi_m \sim 0.74$ is used because the highest packing achievable in our simulation box is hexagonal close packing. Previous theoretical works have shown that $p = 2$ for a variety of situations [92, 93] so that Eq. (2.39) reduces to $\eta_r = (1 - \phi/0.74)^{-2}$.

2.5 Conclusions

This chapter has demonstrated that SRD-MD can be used to simulate the shear viscosity of colloidal suspensions. The mapping between physical and simulated values can be done by SRD-MD without loosing relevant information. The use of the diffusion time scale for computation significantly decreases the simulation time. Shear can also be applied to systems that use MD as a coupling scheme. A Monte Carlo scaling thermostat is necessary to maintain the correct thermodynamic properties of the fluid.

The choice of $\sigma_{cf} = 0.8a$ in defining the volume fraction also gives the correct viscosity values because a small σ_{cf} allows more fluid particles to perturb the flow field surrounding the colloid.

The use of stress tensors for viscosity evaluation provides a better characterization tool than what was previously available as in Ref. [31]. It was observed that the main contribution to the shear viscosity of the suspension comes from the inter-particle collisions rather than streaming. The contribution of the fluid particles to the stress tensor decreases with increasing concentration. This is a consequence of the coupling scheme used and is necessary in order to preserve the Sc of the fluid. However, their role in facilitating lubrication between colloidal particles aids in the increase of kinetic and collisional viscosities of the colloidal suspension, which is not seen in simulations where hydrodynamics are ignored. The presented results are also comparable with other experimental and theoretical studies. While results for hard-sphere suspensions employing other methods, like DPD, have been compared to Eq. (2.37) and (2.39), this is the first time that the relation between shear viscosity and volume fraction is reproduced with SRD-MD. Hence this work serves as a final test on the ability of SRD-MD to predict transport coefficients and rheological parameters where HI's are significant. Moreover, in comparison to DPD, the SRD treatment of the system is computationally faster especially at intermediate and high-volume fractions. This is because it does not rely on the computation of pair-wise potentials hence the computational cost associated with additional colloids does not increase significantly. Moreover, since the value of N_f is reduced at higher concentrations, the number of fluid particles needed to be evaluated is lowered. SRD-MD is also a practical tool for studying the rheology of dense suspensions, an important aspect for studying yield-stress and other phenomena that are occurring in the non-Newtonian regime.

This chapter benchmarks SRD-MD in the modeling of HIs in colloidal suspensions. In the next chapter, SRD-MD is used to determine the effects of HIs in real percolating alumina systems.

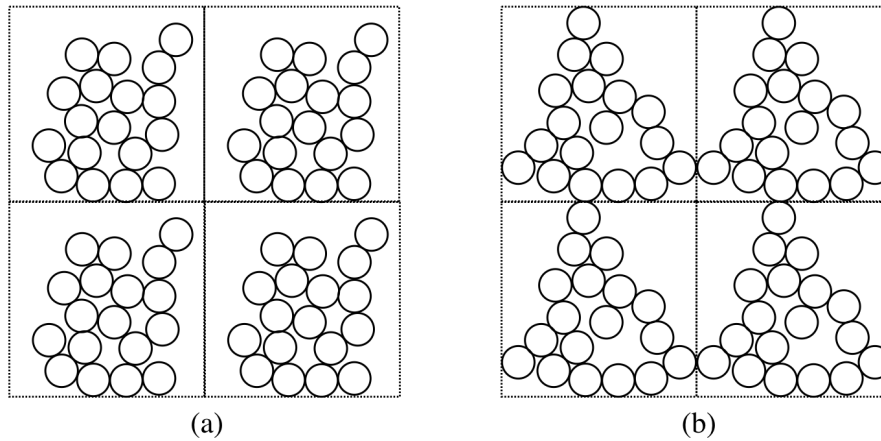# Chapter 3 :

Percolation threshold

Figure 3.1: Schematic diagram of colloidal clusters in representative simulation boxes that are (a) not percolating and (b) percolating in 2D.

In this chapter, the percolation phenomenon is modeled using BD and SRD-MD simulations. Schematic diagrams of non-percolating and percolating systems are shown in Fig. 3.1. In this figure, colloids are placed in a simulation box with mirror images to illustrate how percolation is characterized i.e. when the clusters of colloids form a continuous network that spans through space.

Percolation is a common occurrence in nature and its onset, known as percolation threshold ϕ_c, covers a vast number of fundamental problems in the study of phase behaviour, structural stability and rheology of complex fluids [94, 95]. Percolation threshold appears in models concerning gelation [96], glass and phase transition [97, 98] and conductivity [99] and is therefore of great significance to various industrial and biological systems. The focus of this chapter is the role of percolation threshold on yield stress, which will be introduced in the next section. This study is motivated by the fact that ϕ_c appears as a parameter in the mathematical definition of yield stress [22] and is difficult to evaluate experimentally. To this end, a simulation study can be very helpful.

The range of application of yield stress can start from materials at home like toothpaste and butter spreads to industry such as paper making, the concrete used for construction and biological materials including mucus and other relevant problems in biolocomotion and beyond [98]. Yield stress is also an archetypal rheological property of colloidal suspensions that is of great importance to several ceramic processes. The goals of this chapter are as follows: (1) to offer an alternative approach of measuring ϕ_c, especially for systems where experimental methods are limited or difficult to apply; (2) to investigate the key variables that affect the value of ϕ_c namely, attraction strength and hydrodynamic interactions (HIs); and (3) to compare the results with the yield stress study presented in Refs. [21, 26].

3.1 Yield stress model

For most viscoelastic fluids, yield stress is described as the transition from solid to fluid behavior. For ceramic suspensions, yield stress is the amount of stress needed to deform and induce flow to an otherwise mechanically rigid colloidal network [100]. Hence from the yield stress point of view, one can define the percolation threshold as the point at which a continuous network of colloids is formed leading to a mechanical resistance to deformation. The strength of the network dictates the magnitude of yield stress, hence among the obvious candidates in determining its value are: the density of network of bonds and the strength interparticle attractions. Since the knowledge of yield stress is highly beneficial [101, 102, 103], several models have attempted to provide a quantitative definition of yield stress as a function of these key factors e.g. interparticle forces and microstructural information [104, 105, 100]. However, the limitation in these models is that they are often idealized i.e. they lack a clear representation of other important variables that also contribute to yield stress. This chapter focuses on one important parameter that is often overlooked in these models i.e. percolation threshold ϕ_c.

In their work, Zhou et al. [100] have found that yield stress is dominated by interparticle forces when $\phi > \phi_c$, and by structural effects of weak links when $\phi < \phi_c$. While this observation is only qualitative, it explains the deviation of previous theoretical models from experimental data [100]. This finding clearly indicates that ϕ_c needs to be included in the prediction of yield stress.

Quite recently, a more complete yield stress model (YODEL) that incorporates ϕ_c quantitatively was proposed by Flatt and Bowen [22, 21]. The yield stress τ is given by

$$\tau = m_1 \frac{\phi(\phi - \phi_c)^2}{\phi_{\max}(\phi_{\max} - \phi)}, \tag{3.1}$$

where $\phi_{\max}$ is the maximum packing fraction and m_1 is a factor that accounts for particle size, particle size distribution and interparticle forces. While YODEL shows a good agreement with experiments, it still uses ϕ_c as a fitting parameter.

This drawback mainly stems from the absence of a straightforward experimental approach that can accurately determine ϕ_c. Moreover, the phenomenon itself, despite its common occurrence, is still poorly understood. To this end, numerical methods can serve as convenient tool for determining ϕ_c and can provide a more detailed investigation on the variables that may influence its value.

3.2   On hydrodynamic effects

HIs are omnipresent in nature and additional insights into the role of HIs in the aggregation kinetics of colloids have been observed [106, 107, 108]. Hence, even if the system presented in this chapter is in equilibrium, the presence of HIs can influence the value of ϕ_c. For example, Tanaka and Araki [107] have presented strong indications that HIs influence the transient gel formation of 2D colloidal particles. One of the reasons is that a pair of colloids induces a flow field that can rotate another pair of colloids, which lead to the formation of elongated structures. The other reason is that HIs decrease the approaching speeds of colloids significantly, which again promotes the formation of open and chainlike structures.

In constrast, Yamamoto et al. [109] have demonstrated that hydrodynamic effects have a minor quantitative difference on 3D systems. From their results, hydrodynamic effects are more noticeable on 2D systems due to finite size effects. However, we note that their measurements are performed after quenching the system to zero temperature, where HIs are expected to be negligible [110].

There are other works that supports the preliminary investigations of Tanaka and Araki for 3D systems. Whitmer and Luijten [110] have studied formation of clusters at different attraction strengths and have found that, indeed, more elongated clusters are formed if HIs are considered. However, hydrodynamic effects are outweighed by interparticle forces when the attraction is strong. Their results have also provided an additional insight that the effects of hydrodynamics on ϕ_c should be investigated in different regimes of attraction strength. On the other hand, Tomilov et al. [75] analyzed the aggregation kinetics of colloids by varying the volume fraction and the type of simulation method. The results provided a new role of HIs i.e. they increase the diffusion coefficient for aggregates with respect to the value given by Brownian dynamics. Hence there is a faster cluster-cluster coalescence that impedes the reorganization process within the aggregate and less compact structures are formed.

While the results from these studies suggest that ϕ_c is expected to be lower for a system with HIs than for that without, the results in Refs. [107, 110, 75] concern 2D systems, small systems and simple potentials respectively so that the supposed HIs effects on ϕ_c have never been independently verified.

In this chapter, larger 3D systems are used. Derjaguin-Landau-Verwey-Overbeek (DLVO) theory is also employed and the experimental variables are directly mapped to simulation parameters thus providing the closest representation of the actual system. A summary of the work presented in this chapter is published in Ref. [111].

3.3 Mapping from physical values to simulation parameters

The experimental system presented in Ref. [21, 26], where Stuer and Bowen applied YODEL for doped alumina suspensions, is simulated. The number of spherical colloids that are suspended in water is fixed to $N_c = 500$. The density and viscosity of water is $\rho_f = 1000$ kg·m³ and $\eta = 10^{-3}$ Pa·s respectively. The system is equilibrated at room temperature (293 K) using the Monte Carlo thermostat presented in Section 1.5.2. The colloids have a radius of $a = 255$ nm. The density of alumina 3300 kg·m³ is so that an alumina colloid has corresponding mass of $M = 2.76 \times 10^{-16}$ kg. The suspension is placed in a simulation box of side length L and periodic boundary conditions are imposed to model a large percolating system. The value of L is adjusted depending on the volume fraction ϕ being studied:

$$L = \sqrt[3]{4N_c \pi a^3/(3\phi)}. \tag{3.2}$$

As in the previous chapter, the number of fluid particles used are decreased for every volume fraction according to Eq. (1.33). A summary of the volume fractions and of the corresponding N_f and ϕ values are shown in Table 3.1.

Table 3.1: Corresponding side length of simulation box (L) and number of fluid particles (N_f) in terms of colloid radius a for different volume fractions (ϕ).

$\phi(\%)$	6	7	8	9	10
L/a_0	65	62	59	57	55
N_f	1330232	1148747	984002	883072	788982
$\phi(\%)$	11	12	13	14	15
L/a_0	53	52	51	49	48
N_f	701492	660147	620362	545352	510067

The colloid-fluid is modeled by the IP potential presented in the previous chapter (Eq. 1.31). For the colloid-colloid interaction, the DLVO theory is utilized because it is the closest approximation to real colloidal systems. The DLVO theory, which was developed in the 1940's by Derjaguin and Landau [17] and Verwey and Overbeek [18], has been featured prominently in several studies. Its ability to predict the stability of the colloids suspended in fluid has been crucial for the advancement of colloidal science. In the DLVO theory formulation, the total interaction is the sum of two contributions: the attraction due to van der Waals forces U_{ij}^{vdW}; and electrostatic repulsion U_{ij}^{el} due to the double layers formed by surface charges:

$$U_{ij}^{\mathrm{DLVO}} = U_{ij}^{\mathrm{vdW}} + U_{ij}^{\mathrm{el}}. \tag{3.3}$$

The interaction strength depends on the dielectric properties of both the colloids and the

fluid. The van der Waals term is always attractive and follows a power-law dependence. For particles of the same radius a, this is given by:

$$U_{ij}^{\text{vdW}} = -\frac{A}{6} \left\{ \frac{2a^2}{r_{ij}^2 - (2a)^2} + \frac{2a^2}{r_{ij}^2} + \ln \left[\frac{r_{ij}^2 - (2a)^2}{r_{ij}^2} \right] \right\}. \tag{3.4}$$

Here, r_{ij} is the center-to-center distance between particles i and j and $A = 4.76 \times 10^{-20}$ J is the Hamaker constant for alumina in water [37, 112]. For the electrostatic repulsion part, the Hogg-Healy-Fuerstenau equation is used:

$$U_{ij}^{\text{el}} = \pi \epsilon a \psi^2 \left\{ \ln \left[\frac{1 + e^{-\kappa d}}{1 - e^{-\kappa d}} \right] + \ln \left[1 - e^{-2\kappa d} \right] \right\}, \tag{3.5}$$

where $d = r_{ij} - 2a$, $\epsilon = 81\epsilon_0$ is the dielectric constant of water, ϵ_0 is the permittivity of free space, $\psi = 100$ mV is the surface potential and κ is the inverse of the Debye screening length given by

$$\kappa = \sqrt{\frac{e^2}{\epsilon k_B T} \sum_k n_k z_k^2}, \tag{3.6}$$

where e is the elementary electronic charge; and n_k and z_k are the volume density and valency of ion k respectively. A summary of the parameters used is listed in Table 3.2.

Table 3.2: Parameters used in the study of Percolation.

M	2.76×10^{-16} kg	a	255 nm	ψ	100 mV
A	4.76×10^{-20} J	ϵ	$81\epsilon_0$	T	293 K

One of the points raised in Ref. [21] is the effect of κ on ϕ_c:

$$\kappa = \sqrt{\frac{e^2}{\epsilon k_B T} \sum_k n_k z_k^2}, \tag{3.7}$$

where e is the elementary electronic charge; and n_k and z_k are the volume density and valency of ion k respectively.

The values of κ that are used in this work are shown in Fig. 3.2. Modifying κ effectively changes the attraction strength between the alumina particles. It is important to note that in this system, the aggregation is not caused by the first deep minimum since the colloids would have to overcome a very high potential barrier ($\approx 1200 k_B T$) to reach that first minimum (see Fig. 3.2). Instead, the aggregation is caused by the trapping in the secondary minimum, whose depth can be modulated by varying κ (see inset of Fig. 3.2). BD simulations for different values of κ corresponding to potential well depths of $10 k_B T$, $7 k_B T$, $5 k_B T$ and $4 k_B T$ are performed. In the case of SRD-MD simulations, well depths of $10 k_B T$ and $5 k_B T$ are considered. These well depths of the secondary minima are typical
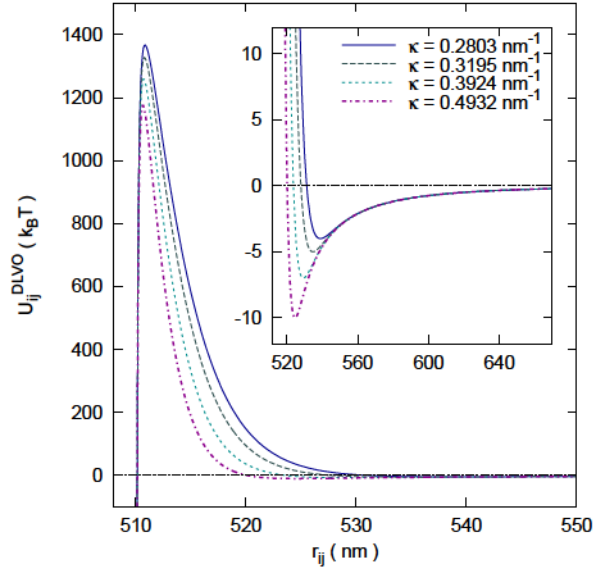
Figure 3.2: The DLVO potential for different values of inverse Debye screening length κ. Inset: the attraction strength between the colloids vary with the well depth of the secondary minimum.

for the alumina system studied in Ref. [21, 26] for ionic concentrations of between 2-5 mM for Mg and Y nitrates. These are typical concentrations for dopant levels of 250 - 500 ppm typically used in the production of polycrystalline aluminas [26].

To get a complete understanding of ϕ_c, an accurate representation of HIs in percolating systems is necessary. The challenge on the computational cost of modeling HIs remains. Since most percolating systems are large systems, computational efficiency is vital. To this end SRD-MD is highly suitable for the study of percolation. Hydrodynamic effects are isolated by comparing the simulation results of SRD-MD with the BD results.

3.4 Time scales

Following the recipes of Ref. [31] in studying colloidal suspensions with DLVO potential, the time scales are checked for 255-nm alumina colloids. The physical time scales and the corresponding coarse grained time scales are shown in Table 3.3. The variable τ_0 corresponds to the oscillation frequency at the bottom of the second minimum [65]. Note that the ordering of the time scales i.e. $\tau_D > \tau_0 > \tau_v > \tau_B$ in the physical regime is the same as the ordering of time scales in the SRD-MD regime. This means that the physical behaviour of the colloids is preserved when observing at the diffusion time scale [31, 30].

The time step used for BD is $\Delta t_{\mathrm{BD}} = 2 \times 10^{-7}$ s. For the SRD-MD simulations, the same framework as discussed in Chapter 3 is used. The time scale for SRD-MD is chosen

Table 3.3:   Hierarchy of time scales for a 255-nm alumina colloid suspended in water and its corresponding coarse grained values for SRD-MD.

	τ_D	τ_0	τ_ν	τ_B
Physical	1.5×10^{-1}	2.5×10^{-4}	1.3×10^{-7}	5.7×10^{-8}
SRD-MD	1.5×10^{-1}	8.9×10^{-2}	9.2×10^{-3}	7.1×10^{-3}

Table 3.4:   SRD parameters used in the study of percolation threshold.

α	$90°$	σ	204 nm
γ	5	T_{SRD}	0.002 K
λ	0.1	Δt_{SRD}	4.53×10^{-5} s
a_0	127.5 nm	m_f	4.145×10^{-19} kg

so that the most relevant time scale for percolation analysis, i.e. the colloid diffusion time τ_D, is accurately reproduced. The experimental value of τ_D is 1.5×10^{-1} s. For the MD part, an MD time step of $\Delta t_{\mathrm{MD}} = \frac{1}{8}\Delta t_{\mathrm{SRD}} = 5.67 \times 10^{-6}$s is chosen. Consequently, the SRD temperature becomes $T_{\mathrm{SRD}} = 0.002$ K and the units of energy and viscosity of the simulation changes to $k_B T_{\mathrm{SRD}} = 2.8 \times 10^{-26}$ and $\eta_{\mathrm{SRD}} = 1.76 \times 10^{-8}$ Pa·s respectively. The value of η_{SRD} is computed using the analytical equation for fluid viscosity that is presented in Sec. 2.2.3. The SRD parameters employed in this study are summarized in Table 3.4.

3.5   Parameters for aggregate analysis

One can describe a percolating system as being made up of aggregated colloids, where the largest aggregate spans an infinitely large space. Hence the first step into quantifying the aggregation kinetics is to provide a definition of an aggregate. In the simulations, an aggregate is an assembly of two or more connected colloids. Two colloids are considered as being connected when their mutual distance $r_{ij} \leq \delta r$, where $\delta r/2 = 1.2a = 306$ nm. The value of δr corresponds to the first-neighbor distance obtained from the radial distribution function of the aggregated system. A schematic diagram is shown in Fig. 3.3

3.5.1   Number of aggregates vs time (N_A vs t)

From Ref. [75], it has been shown that the aggregation process can be divided into three regimes. The first is dimer formation, where solitary colloids pair up with other colloids. The second is aggregate coalescence, where aggregates come together to form larger clusters. The final step, which is reorganization, happens when the attraction strength permits detachment and re-attachment within the aggregate that promotes ordering. These regimes can be observed by monitoring the number of aggregates N_A as a function of time. The result of the time evolution N_A can also determine the appropriate
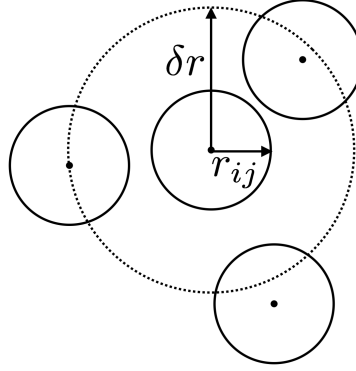
Figure 3.3: The value of δr dictates whether the nearest colloid is a considered as neighbor or not.

time interval for the measurement of ϕ_c.

3.5.2 Parameters P_D and ϕ_c

To numerically pinpoint ϕ_c, the same process used in Ref. [38] is employed. From the original simulation box of side length L, seven other mirror images are produced in the x, y and z directions, resulting to a larger box with size of $2L \times 2L \times 2L$. Once the new box is formed, the largest aggregate traversing the enlarged box is singled out and its linear extensions (D_x, D_y, D_z) along the three directions are measured. If the components of D satisfy the condition:

$$D_i \in [2L - \delta r, 2L], \quad \text{where} \quad i = x, y, z \tag{3.8}$$

then the aggregate is counted as percolating in the ith direction. To characterize the type of percolation in a system i.e. in 1 direction, in 2 directions or in all 3 directions, the number of times Eq. (3.8) is satisfied is recorded for a given volume fraction. This dimensionless parameter is called P_D. The results reported here are averaged over 5 independent simulations so that P_D can have non-integer values between 0 and 3. For example, if for a given volume fraction, 3 simulations percolate in 3 directions and the other two simulations percolate in 1 direction, then the resulting P_D is 2.2. The value of P_D also represents the probability of observing percolation in 3 directions.

To characterize ϕ_c and to account for the statistics of 5 different simulations, a threshold for P_D is set. Specifically, ϕ_c is determined by the conditions that for $\phi = \phi_c, P_D > 2$ and for all $\phi > \phi_c, P_D \geq 2$. If $P_D \geq 2$ the average percolation is in at least 2 directions. This means that at least one of the simulations fully percolates in 3 directions. Choosing a lower threshold for P_D would not change the qualitative trends of the results, while somewhat decreasing the values of ϕ_c, especially for the cases of weaker

attraction. It is also important to note that if $P_D = 1$ is chosen instead of $P_D = 2$, the results would be noisier because they are related on average to system with fewer particles.

3.5.3 Number of nearest neighbors

Systems with elongated aggregates tend to have higher values of P_D. Consequently, the values of ϕ_c for these systems are expected to be low. Hence the values of P_D and ϕ_c can already characterize the systems between having elongated aggregates or compact aggregates. However, a different method of quantifying the ordering of an aggregate can also be performed independently. This is done by counting the percentage of colloids having 12 nearest neighbors [113]. Since compactness is correlated to the degree of organization, it is expected that compact aggregates have higher percentages of nearest neighbors than their elongated counterparts.

3.6 Results

3.6.1 Dissociation times

The reorganization process is a consequence of the dissociation and association of the colloids within an aggregate. The frequencies of dissociation and association of colloids dictate the amount of ordering an aggregate can achieve, which can affect the value of ϕ_c. The challenge in SRD-MD is that only one time scale can be accurately reproduced during the mapping procedure. The rest of the time scales will have values that are different from the experimental values. As mentioned in Ref. [30], the correct physics is still reproduced as long as the ordering of the time scales is preserved (see Table 3.3). However, it still important to check the dissociation time scale of the percolating system presented in this chapter to ensure that the reorganization of the colloids is not affected by the mapping procedure of SRD-MD. Note that a similar problem is not present in the BD simulations.

The dissociation time is tested using the DLVO potential with a well depth of $7k_BT$. This value was chosen because it lies in the middle of $10k_BT$ and $5k_BT$. Moreover, a simulation for a $10k_BT$ potential well depth is time consuming while a simulation for a $5k_BT$ potential well depth is too fast so that it is prone to statistical errors. To determine an average dissociation time, two colloids are placed in a simulation box ($L = 32a_0$) at an equilibrium distance $r_0 = 5.29264 \times 10^{-7}$ m and are allowed to evolve until they dissociate at time τ_{dissoc}. The calculated values are shown in Table 3.5. The reported values are averaged over 200 independent simulations. The results show that the dissociation time for SRD-MD is longer than the dissociation time for BD. This is expected because by

Table 3.5: Dissociation times for BD and SRD-MD.

	BD	SRD-MD
Δt (s)	2.0×10^{-7}	4.53×10^{-5}
τ_{dissoc} (s)	0.22	0.68

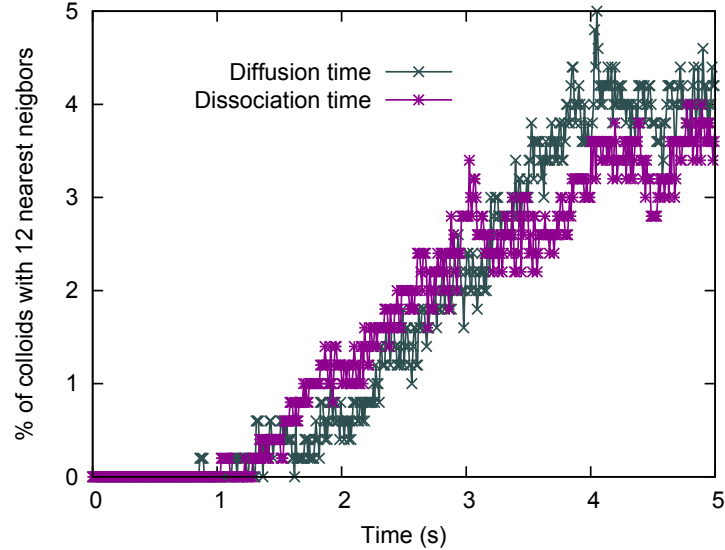

Figure 3.4: The degree of ordering for a $5k_BT$ well, measured by the percentage of colloids having 12 nearest neighbours. This is a comparison between the diffusion time scale ($\Delta t_{\text{SRD}} = 4.53 \times 10^{-5}$ s) and dissociation time scale ($\Delta t_{\text{SRD}} = 2 \times 10^{-5}$ s). The system consists of 200 colloids in a dilute environment of $\phi = 5\%$. The results are averaged over 5 simulations.

mapping to the diffusion time scale, the rest of the time scales, including the dissociation time scale, will have values that are different from the experimental or BD values.

Hence to see if the difference in dissociation times affects the reorganization of the aggregate, two types of simulations are performed: one mapped to the diffusion time scale ($\Delta t_{\text{SRD}} = 4.53 \times 10^{-5}$ s); and the other map to the dissociation time scale ($\Delta t_{\text{SRD}} = 2 \times 10^{-5}$ s). The system used consists of 200 colloids in a dilute environment ($\phi = 5\%$). A well depth of $5k_BT$ is used because the ordering for the $7k_BT$ and $10k_BT$ systems are not recognizable for the simulation time that is achievable (≈ 5 s). The results in Fig 3.4 show that the difference between the reorganization of the clusters is not significant even if the dissociation times are different. Therefore, even with the mapping procedure used in SRD-MD, the ordering of the colloids is properly reproduced.

3.6.2   Influence of the colloid-colloid attraction strength

Before analyzing the simulation results, a preliminary check of the appropriate time interval needed to obtain a stationary state is necessary. This is important because
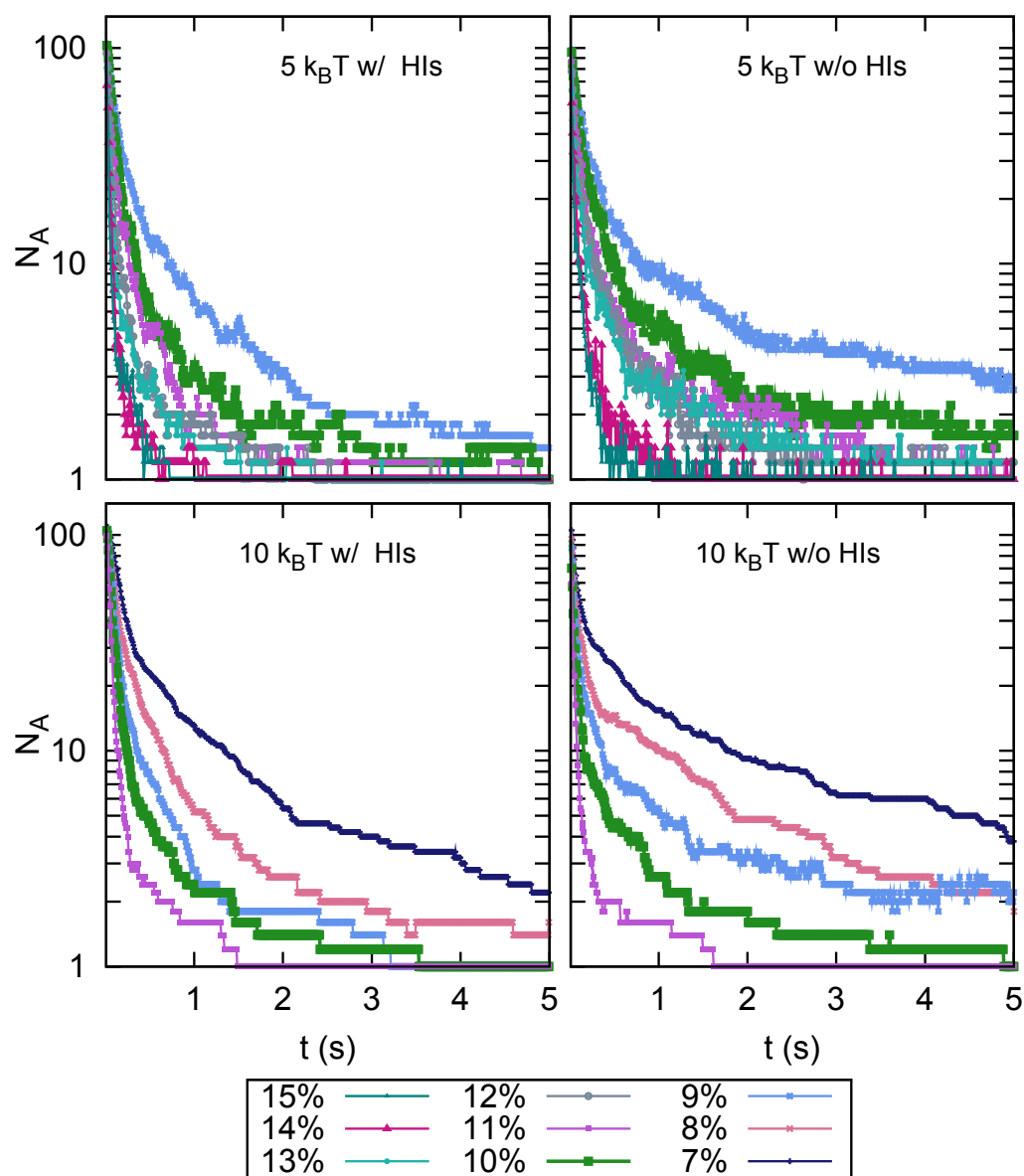
Figure 3.5: Semi-logarithmic plot of the number of aggregates N_A vs time t for potential well depths $5k_BT$ and $10k_BT$ for different volume fractions.

aggregate coalescence is slower in the absence of HIs [75] and it is important to have approximately the same sizes of aggregates when determining ϕ_c. Sample results of the temporal evolution of the number of aggregates N_A for $5k_BT$ and $10k_BT$ cases are shown in Fig. 3.5. Since the formation of a large aggregate, the one responsible for percolation, is faster with HIs, the P_D of the aggregates formed at 5 s when HIs are present are compared to the P_D of the aggregates formed at 5 s and 20 s when HIs are absent. At 20 s, the N_A values are almost the same between the two simulations.

For the systems without HIs, the measured P_D values for different volume fractions are shown in Figs. 3.6. By imposing the limit that the onset of percolation happens when $P_D > 2$, the following ϕ_c for the different well depths are obtained: 15% for $4k_BT$, 12% for $5k_BT$, 9% for $7k_BT$ and 8% for $10k_BT$. Since there are no significant differences between the values of P_D measured at 5 s and 20 s, the ϕ_c values do not change between the two time intervals. It is notable from these results that the percolation threshold is greatly
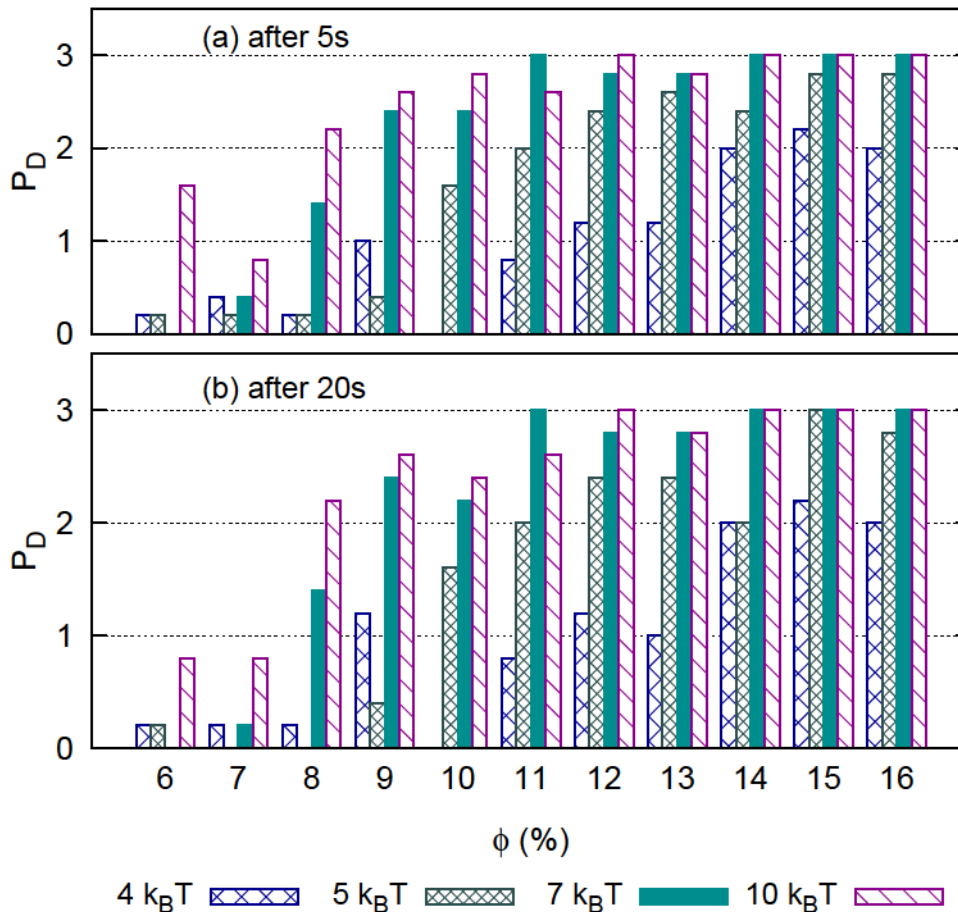

Figure 3.6: The number of directions the system is percolating P_D is plotted against the volume fraction ϕ for sytems without HIs. There are no significant differences between the measurements done after 5 s and 20 s.

influenced by the ionic strength of the suspension, which is represented by varying the well depths in the model. The value ϕ_c increases with decreasing well depth. The reason is because percolation is less favored when an aggregate is compact. This is in agreement with the results of Refs. [113, 114], where compactness is observed at shallower well depths.

3.6.3 Influence of HIs

For the systems with HIs, the P_D for well depths $5k_BT$ and $10k_BT$ are shown in Fig. 3.7. Similar to the systems without HIs, the attraction strength influences the percolation threshold i.e. a higher ϕ_c corresponds to the shallower well depth of $5k_BT$. In comparison to the systems without HIs however, Figs. 3.7 show that P_D is generally higher when HIs are taken into account. This is because the shape of the aggregates results from the competition between aggregate growth kinetics and reorganization kinetics. On one hand, HIs speed up the aggregate growth by cluster-cluster coalescence because HIs increase their diffusivity [75]. On the other hand, HIs slow down the reorganization. Both contribute to the formation of less compact aggregates with HIs. The results in Figs. 3.7 also show that the effects of HIs on P_D are more discernible at smaller volume fractions. This is because the contrast in the number of fluctuations in the N_A vs. t curve is more evident for dilute suspensions (see Fig. 3.5).

Sample illustrations of the systems with and without HIs are shown Fig. 3.8. Both systems have a volume fraction of 10% and a well depth of $10k_BT$. The colored region
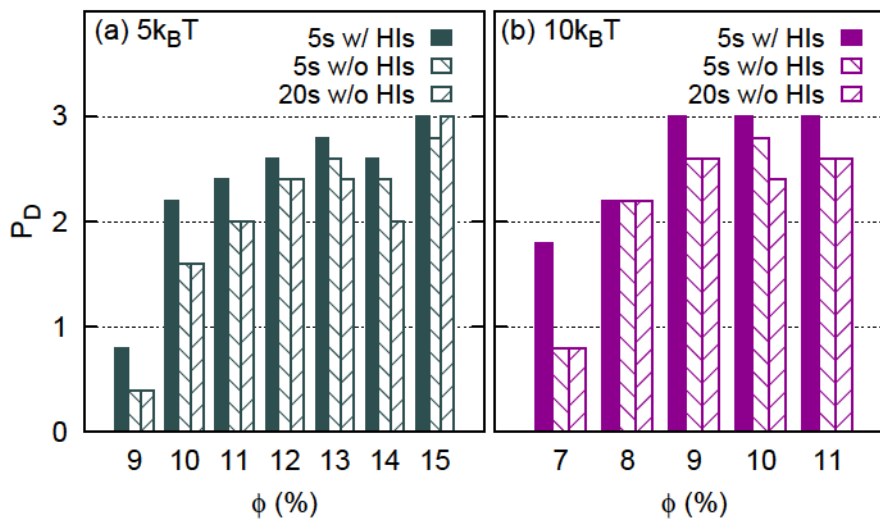

Figure 3.7: The number of directions the system is percolating P_D is plotted against the volume fraction ϕ for (a) $5k_BT$ and (b) $10k_BT$ well depths. The solid bars correspond to systems with HIs and the line-filled bars correspond to systems without HIs.

represents the largest aggregates formed. In the case shown here, it is apparent that the largest aggregate in the system with HIs is more elongated. The biggest aggregate, when there are no HIs present, is percolating in only 1 direction; while the biggest aggregate, when HIs are present, is percolating in all 3 directions.
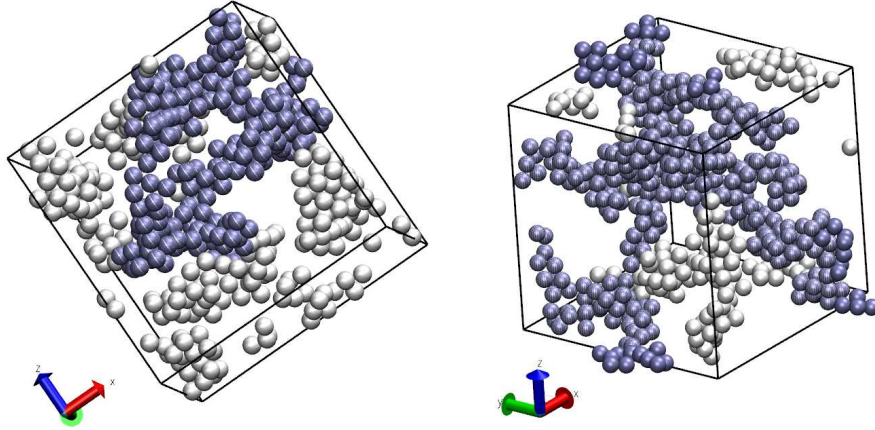

Figure 3.8: A system without HIs simulated using BD (left) vs. a system with HIs simulated using SRD-MD (right). The colored region represents the largest aggregate formed. By comparison, the aggregate simulated with HIs is more elongated and has a higher probability of percolating than the aggregate simulated without HIs.

3.6.4 Percolation threshold measurements

Here, the $P_D > 2$ condition is considered as a criterion to define the onset of percolation. The observed elongation of aggregates induces some decrease in the measured ϕ_c. This decrease is more evident when the potential well is shallow. In fact, $\phi_c = 8\%$ is obtained for the $10k_BT$ potential well, regardless of HIs effects, even though the result for $\phi = 7\%$ with HIs is very close to verify the $P_D > 2$ condition. On the other hand, $\phi_c = 10\%$ with HIs and $\phi_c = 12\%$ without HIs for the $5k_BT$ potential well.

The fluctuations of N_A during the aggregation process help in understanding whether hydrodynamic effects are more important at shallower well depths. The results are presented in Fig. 3.5. The fluctuations in the curve correspond to the association and dissociation of aggregates that promotes reorganization. Indeed the fluctuations are more prevalent without HIs and this difference is more recognizable in the $5k_BT$ case than in the $10k_BT$ case.

To further verify the compactness of the system, the number of neighbors is used as an order parameter. Fig. 3.9 shows the percentage of colloids having 12 nearest neighbors as

a function of time for the $5k_BT$ well. The corresponding plots for the $10k_BT$ systems are essentially zero and are not shown here. Note that the variations of the order parameter as a function of volume fraction are within statistical errors. Hence only the average differences between systems with and without HIs are considered. Since the percentage of colloids having 12 nearest neighbors is lower with HIs, this justifies that the structures obtained after 5 s are more elongated when HIs are accounted for.
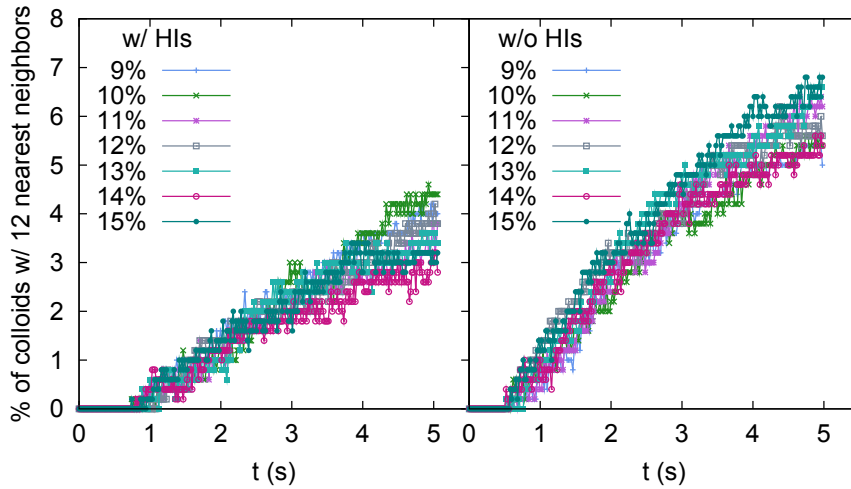

Figure 3.9:   The rate of ordering for $5k_BT$ measured by counting the number of colloids with 12 nearest neighbours. The system without HIs shows a higher degree of ordering in comparison to the system with HIs. For $10k_BT$, this order parameter is essentially zero.

These observations suggest that for high ionic strengths, the attraction strength dictates the value of ϕ_c since it dominates over the effects of HIs. However, for low ionic strengths, HIs influence ϕ_c by lowering its value. The kinetics plays a crucial role in dictating ϕ_c. Aggregation is a three-part process: dimer formation, aggregate coalescence, reorganization. The first two stages are studied in Ref. [75]. However, it is worth noting that there is an overlap in the aggregate coalescence and reorganization stages. The combination of the fast aggregate coalescence with the slow reorganization due to HIs both affect ϕ_c.

The results of the simulations are summarized in Fig. 3.10. The solid line dividing the two regions is an approximate ϕ_c value when HIs are not present. The shaded region corresponds to a higher probability of observing percolation in 3D. The red squares represent ϕ_c values measured when HIs are included. When comparing the simulation results with the results of the yield stress modeling in Refs. [21, 26], a good correspondence with BD simulations is found for the higher ionic strengths of 0.0044 M (Y^{3+}), where the
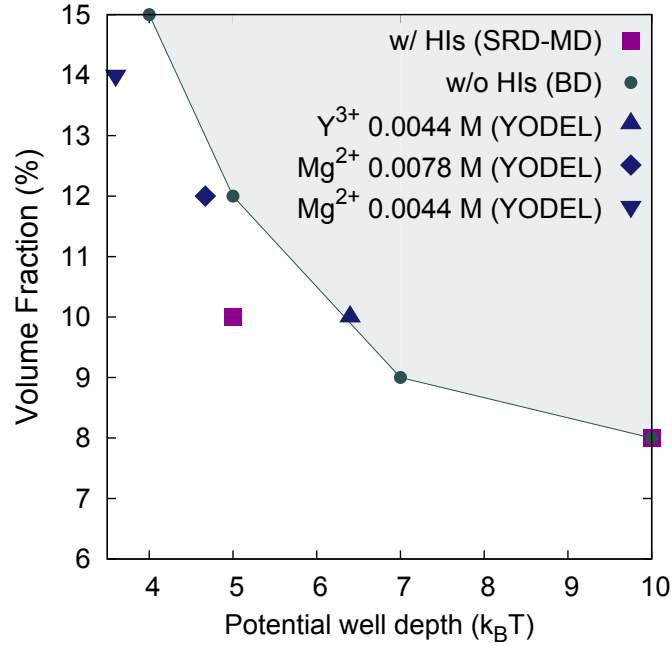
Figure 3.10: The summary of percolation threshold for systems with and without HIs presented as a relation between potential well depth and volume fraction.

well depth was around $6.4k_BT$ and $\phi_c = 10\%$. On the other hand, the estimated ϕ_c are 12% and 14% for the shallower well depths of $4.67k_BT$ and $3.6k_BT$ respectively. These values are lower than the ones predicted by BD. However, this is still in good agreement with the simulation results since a shift to smaller values is expected for shallower well depths as a consequence of introducing HIs. Moreover, in Refs. [21, 26] the estimate of ϕ_c follows from a fitting procedure within the YODEL model.

3.7 Conclusions

In conclusion, the results show that stronger interparticle attractions decrease the magnitude of the percolation threshold ϕ_c. In addition to this, higher P_D values are observed when HIs are present due to the more elongated structures formed. Correspondingly, an effect of HIs on the percolation threshold is seen. This effect is evident for shallow potential wells ($\phi_c = 10\%$ with HIs and $\phi_c = 12\%$ without HIs for a well depth of $5k_BT$), and tends to become smaller and smaller with increasing well depth.

It is important to note that the simulation measurements are performed at specific time intervals. The transient aggregates observed may evolve to stable low-energy structures [109] or arrested structures [115, 23, 116, 117]. But the time scale to which this may occur and the final state of the aggregate is difficult to predict. Despite this, a good qualitative agreement between simulations and experiments is observed.

Finally, the results of this chapter can also be used to determine the most convenient

simulation method for studying percolation in colloidal aggregates. A good indicator for determining the most appropriate method is the attraction strength between the colloids. When the attraction is strong (well depths of $10k_BT$ or more), the rearrangement is very slow due to the high energy barriers hindering the motion of colloids inside the aggregates. This is the dominating factor for determining the percolation threshold, while hydrodynamic effects tend to be negligible. In this case, BD simulations, which are considerably faster than any other method with HIs, should suffice. These general trends are also in good agreement with estimates of the percolation threshold for the deeper well depths from yield stress modeling using YODEL. On the other hand, for weaker colloid-colloid attraction, hydrodynamic effects on percolation can be sizable, so that methods which include HIs should be used. In this case, it is worth noting that SRD-MD is still the fastest technique available that can model HIs in percolating networks.

In the next chapter, BD simulations are performed to investigate the aggregation of colloidal suspensions on attractive walls. BD simulations are used because they are simpler and relatively well-known for the system being modeled. Additionally, an initial study for shaken colloidal suspensions is performed. The same alumina system discussed in this chapter in placed under an oscillating shear force to determine whether it can enhance the ordering of the aggregates.

Chapter 4 :

Attractive Walls and Shaking

The ability to tune the interaction between particles in the presence of external forces is a quintessential problem in colloidal science [118, 119, 120]. The presence of a solid surface and/or external shear are more common in experiments than the occurrence of a perfect system without any external perturbation. From a theoretical point of view, this type of problem is also interesting because it can provide additional insights not just about the actual motion of colloids in the fluid, but also about the mechanisms that rule colloid aggregation with external forces. Moreover, this work can be potentially useful in designing experimental procedures that can be used to obtain crystals with desired structures and properties.

4.1 Attractive Walls

Particular attention has been given to the numerical modeling of the aggregation of colloids [19, 16]. As mentioned, the primary reason is because colloids display the same phase behavior as atoms and molecules, but with the mesoscopic size advantage thus allowing direct obervation in real space [121, 122]. Another reason is because colloids serve as excellent models in the understanding of protein adsorption on surfaces since both systems are subject to the same thermodynamics, but with the colloids having the benefit of simpler length scales [119, 123]. Therefore, whether the problem is on protein adsorption [124] or the efficacy of deposition in implant materials [125], a predictive model that can explain the behavior and properties of colloids can be used to increase our understanding of the aggregation kinetics of the colloidal particles.

In this chapter, binary colloidal suspensions are used. These are systems consisting of two types of particles, which can acquire opposite charges in the suspension and interact mainly through screened electrostatic forces. Binary systems have been prominently
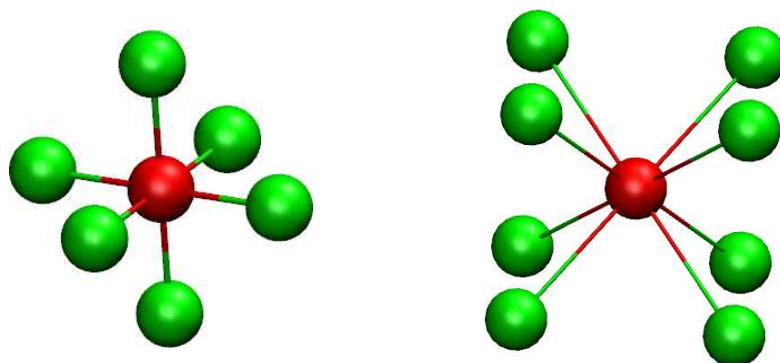

Figure 4.1: Sample primitive cells for NaCl-type lattices (left) and CsCl-type lattices (right). For the NaCl lattice, an atom is surrounded by 6 first nearest neighbors of a different kind. For the CsCl lattice, an atom is surrounded by 8 first nearest neighbors of a different kind.

featured in the recent years due to the heteroaggregation phenomena that can lead to even more diverse types of colloidal crystals [126, 16, 127]. The motivation of this study comes from the previous work by Bochicchio et al. [39, 128] where the aggregation kinetics of binary colloidal crystals in equilibrium is modeled. The crystals formed exhibit NaCl-type or CsCl-type lattices (see Fig. 4.1). Ref. [39] have found that the most stable colloidal crystal depends on the parameter κa, in which κ is the Debye inverse length and a is the colloid radius. For $\kappa a < 2.55$ (long interaction ranges) the NaCl structure is energetically favored, while for $\kappa a > 2.55$ the CsCl structure prevails. However, aggregation simulations show that the NaCl structure is also formed for κa in the interval $2.55 - 3.3$ due to kinetic effects. The study of the aggregation mechanism has shown that a metastable liquid aggregate is obtained. First, solidification occurs when stable nuclei are formed inside this aggregate. If $\kappa a < 3.3$, the interaction range is sufficiently long and hinders the formation of CsCl nuclei, in which a particle of a given type has to be surrounded by 8 particles of the opposite charge. A subsequent metadynamics study by Bochicchio et al. [128] has shown that the transition from the metastable NaCl aggregates formed for $2.55 < \kappa a < 3.3$ to the energetically stable CsCl requires surmounting large energy barriers, so that the metastable NaCl aggregates may have very long lifetimes.

This chapter serves as an extension of Refs. [39, 128]. The goal is to determine further possible alterations to the same binary system when an attractive wall is introduced. In light of the observation described above, this chapter focuses on the modifications in the region where metastable NaCl structures are formed: $\kappa a < 3.3$.

The nature of the aggregation of colloids on the surface of the wall is analyzed and the parameters that affect their conformation on the surface are determined. These parameters include: the bulk properties of the suspension, namely, potential well-depth (U_0) and inverse range of interaction (κa); and the interaction strength between the wall and the colloids ($\varepsilon_{\text{Wall}}$).

4.2 System: suspension with attractive walls

A schematic diagram of the system is illustrated in Fig. 4.2. For the suspension part, the binary colloids used are similar to the ones presented in Refs. [39, 128]. A binary colloidal system is immersed in water ($\rho_{\text{H2O}} = 1000$ kg·m^{-3}) with viscosity 0.001 Pa·s at room temperature 293 K. An equal number for each type of colloid ($N_1 = N_2 = 250$) is used. Both particles have a radius of $a = 300$ nm and carry the same charge magnitude $|Z|$ but with opposite signs $Z_1 = -Z_2$. In these simulations, the colloids interact by a Yukawa potential, which only takes into account the screened electrostatic interactions, without including van der Waals terms. Since electrostatic forces are dominant for the system presented in this chapter, the Yukawa results are very close to that obtained by
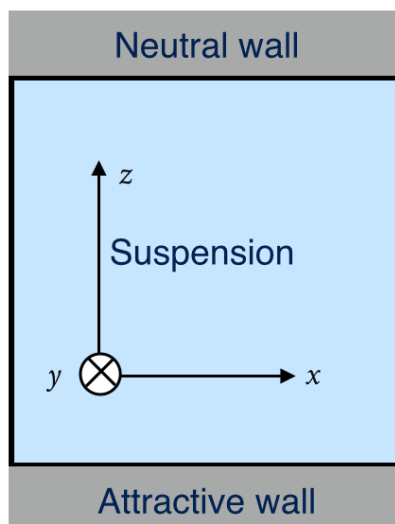
Figure 4.2: Schematic diagram of the walled system. The attractive wall with varying well-depth is placed at $r_z = 0$ and a neutral wall is placed at $r_z = L$ to avoid particles from reaching heights that are very far from the attractive wall.

Table 4.1: Parameters for system with attractive walls

N_c	500
a	300 nm
ϵ	$81\epsilon_0$
Δt_{BD}	2×10^{-7} s
T_{BD}	293 K

the more sophisticated DLVO potential. For particles with equal radii a, the Yukawa potential is given by

$$U_{ij}^Y = \frac{Z_i Z_j}{(1 + \kappa a)^2} \frac{e^2}{4\pi\epsilon} \frac{e^{-\kappa(r_{ij} - d)}}{r_{ij}} \tag{4.1}$$

where Z_i and Z_j are the charges of particles i and j respectively, e is the elementary electron charge, r_{ij} is the center to center distance between particles i and j, and $d = 2a = 600$ nm. The dielectric constant of water is $\epsilon = 81\epsilon_0$, where ϵ_0 is the permittivity of free space. The term κa is an important physical parameter that describes the length scale of electrostatic interactions relative to the particle radius. A lower κa value means a longer range of repulsion while a higher κa value means a shorter range of repulsion. Since it was found in Ref. [39] that NaCl structures are formed when $\kappa a < 3.3$, the focus of this work is in this region of interaction ranges. The following values of $\kappa a = 3, 2.55, 1.5$ and 1 are tested against the strength of interaction with the attractive wall. Fig. 4.3 shows an example of Yukawa potential interaction colloids in the suspension. In this example, the inverse Debye screening length used has a value of $\kappa = 0.00831$ nm^{-1} and the charges used have a magnitude of $|Z| = |251|$.

The interactions between oppositely charged colloids are attractive and diverge as $r_{ij} \to 2a$. To avoid numerical instabilities associated with this asymptotic behavior, the hard-wall potential given by

$$U_{ij}^{HW} = \left(\frac{r_{ij} - 2B_{ij}a}{C_{ij}} \right)^4 - D_{ij} \tag{4.2}$$

is connected to the Yukawa potential. D_{ij} has units of energy and regulates the depth of the well. The parameters B_{ij} and C_{ij} are dimensionless parameters that can be chosen such that:

$$B_{ij} = \frac{1}{2a} \left\{ r' - 4 \left[\frac{U_{ij}(r) + D_{ij}}{dU_{ij}(r)/dr} \right] \right\} \tag{4.3}$$

$$C_{ij} = 4 \frac{[U_{ij}(r) + D_{ij}]^{3/4}}{dU_{ij}(r)/dr} \tag{4.4}$$

where r' is the point of connection. Another alternative is to use a linear function that directly cuts the DLVO or Yukawa potential at a desired distance. However Eq. (4.2) gives a continuous function for the equations of the potential and the force thus allowing smooth transition between the attractive and repulsive part. A continuous first and second derivative means that instabilities in the simulation can also be avoided. For the example shown in Fig. 4.3, the cut-off distance for the attractive interactions is set to $1.072d$ while the cut-off distance for the repulsive interactions is set to $1.02d$ [128].

To describe the attractive surface, a simple potential in the form of the Lennard-Jones
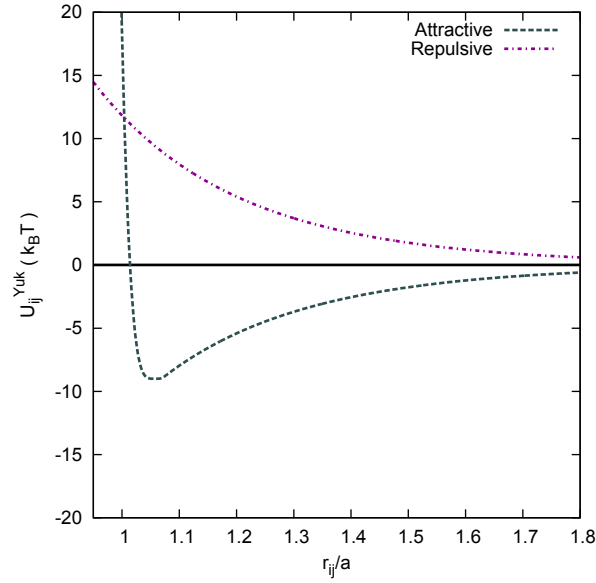
Figure 4.3: The interaction between alumina and silica colloids in the suspension is described by a Yukawa potential with parameters listed in Table 4.1.

Table 4.2: The well-depth values of the LJ 9-3 potential that used to define the interaction of the colloids with the wall. The effective potential well-depth is given by $\varepsilon_{\text{Wall}}$.

$\varepsilon_{\text{Wall}}$ $(k_B T)$	$\epsilon_{\text{Wall}}(k_B T)$
8	0.09950
9	0.11200
10	0.12440
11	0.13680
12	0.14990
15	0.18700

(LJ) 9-3 potential is used:

$$U^{\text{Wall}}(r) = \frac{2}{3}\pi\rho_{\text{Wall}}\sigma_{\text{wall}}^3\epsilon_{\text{Wall}}\left(\frac{2}{5}\frac{\sigma_{\text{Wall}}^9}{r_z^9} - \frac{\sigma_{\text{Wall}}^3}{r_z^3}\right), \tag{4.5}$$

where $\rho_{\text{Wall}} = 5$ and $\sigma_{\text{Wall}} = 4a$. Note that simulations with $\sigma_{\text{Wall}} = 1.2a$ are also checked and similar results to $\sigma_{\text{Wall}} = 4a$ are obtained. The value of ϵ_{Wall} is varied to modulate the strength of attraction between the walls and the colloids. The effective potential well is given by the terms outside the parentheses: $\varepsilon_{\text{Wall}} = \frac{2}{3}\pi\rho\sigma^3\epsilon_{\text{Wall}}$. A list of the values used are shown in Table 4.2.

The surface of the wall is at $r_z = 0$ and the first layer of colloids are formed around $3.1 < r_z < 3.5$. A neutral wall is placed at $r_z = L$ to avoid particles from reaching heights far from the attractive surface. Hence the system is periodic only in the x and y directions.

The suspensions are relatively dilute with a volume fraction of $\phi = 20\%$ so that HIs are expected to be significantly small. The simulations are performed using the Brownian Dynamics algorithm in GROMACS [129] with a time step of $\Delta t_{\mathrm{BD}} = 2 \times 10^{-7}$ s.

4.3 Parameters for Aggregate Analysis

P_{3D} is a parameter that can be used to discriminate the formation of either NaCl-type or CsCl-type lattices. This is defined as follows [39]:

$$P_{\mathrm{3D}} = \frac{1}{N_c} \sum_{i \neq j} \left[\frac{1}{12} \exp\left(\frac{r_{ij} - r_{\mathrm{NaCl}}}{2\sigma_{\mathrm{NaCl}}^2} \right) - \frac{1}{6} \exp\left(\frac{r_{ij} - r_{\mathrm{CsCl}}}{2\sigma_{\mathrm{CsCl}}^2} \right) \right]. \qquad (4.6)$$

The first term corresponds to the probability of finding a particle with 12 second nearest neighbors (SNN) around a cut-off radius of $r_{\mathrm{NaCl}} = 895$ nm. The second term corresponds to the probability of finding a particle with 6 SNN around a cutoff radius of $r_{\mathrm{CsCl}} = 737$ nm. The values of r_{NaCl}, r_{CsCl} and their corresponding standard deviations $\sigma_{\mathrm{NaCl}} = 20$ nm and $\sigma_{\mathrm{CsCl}} = 20$ nm are obtained from the radial distribution function of the colloids [27]. As a further verification step, a two-dimensional version of Eq. (4.6) is used. It was observed that the first layer of CsCl and NaCl attached to the surface of the wall can be differentiated. A CsCl structure will have its (101) plane attached to the surface of the wall while an NaCl structure will have its (100) plane attached to the surface wall. The (101) CsCl-plane leads to a rectangular lattice with one side having r_{CsCl} while the (100) NaCl-plane leads to a square lattice with r_{NaCl}. In 2D, the SNN for CsCl with r_{CsCl} is 2; while the SNN for NaCl with r_{NaCl} is 4. Taking this into consideration, the parameter P_{2D} is defined as follows:

$$P_{\mathrm{2D}} = \frac{1}{N_s} \sum_{i \neq j} \left[\frac{1}{4} \exp\left(\frac{r_{ij} - r_{\mathrm{NaCl}}}{2\sigma_{\mathrm{NaCl}}^2} \right) - \frac{1}{2} \exp\left(\frac{r_{ij} - r_{\mathrm{CsCl}}}{2\sigma_{\mathrm{CsCl}}^2} \right) \right], \qquad (4.7)$$

where N_s is the total number of colloids on the surface.

4.4 Results

4.4.1 NaCl vs CsCl

First, the effect of the wall on a suspension is analyzed. For this part, a system with $U_0 = 9k_BT$ and $\kappa a = 2.55$ is used as an example. In an infinite system, the expected final structure for this suspension is NaCl. Fig. 4.4 shows what happens to the suspension when a wall with $\varepsilon_{\mathrm{Wall}} = 10k_BT$ is introduced. In the beginning of the
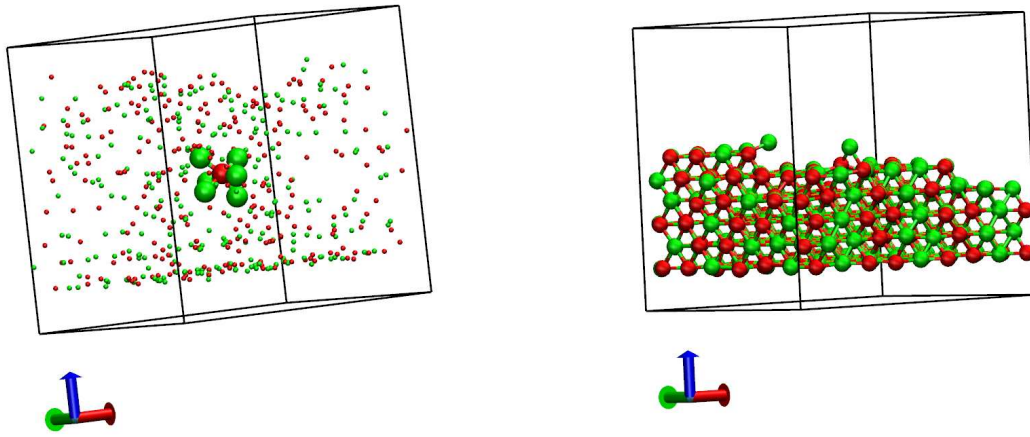
Figure 4.4: Snapshot of the suspension with $U_0 = 9k_BT$, $\kappa a = 2.55$ and $\varepsilon = 10k_BT$ at $t = 1.25$ s (left) and at $t = 80$ s (right). The radii of the colloids are scaled for clarity. In the beginning, a few NaCl seeds are formed at a distance far from the range of attraction of the wall. At the end of the simulation, only CsCl structures are observed.

Table 4.3: Different structures formed on the wall with varying $\varepsilon_{\text{Wall}}$. The suspensions used have $U_0 = 9k_BT$ and $7k_BT$ respectively.

| | $U_0 = 9k_BT$ | | | | $U_0 = 7k_BT$ | | |
| | $\kappa a = 2.55$ | | | | $\kappa a = 3$ | | |
$\varepsilon_{\text{Wall}}$	NaCl	CsCl	Mixed	$\varepsilon_{\text{Wall}}$	NaCl	CsCl	Mixed
$7k_BT$	3	0	2	$5k_BT$	4	1	0
$8k_BT$	2	1	5	$6k_BT$	2	2	1
$9k_BT$	3	2	3	$7k_BT$	3	1	1
$10k_BT$	1	1	3	$8k_BT$	1	3	1
$12k_BT$	0	5	0	$9k_BT$	1	3	1
$15k_BT$	0	3	2	$10k_BT$	2	3	0

simulation ($t = 1.25$ s), NaCl seeds are observed outside the attraction range of the wall ($r_z > 4a$). One representative seed is shown in the left hand side of Fig. 4.4. However, towards the end of the simulation, when all of the colloids are attached to the surface, the NaCl seeds disappeared and only CsCl structures are left. This means that the wall can alter the colloidal structure by forming CsCl lattices instead of metastable NaCl lattices. To measure the extent of this effect, the strength of the colloid-wall interaction ($\varepsilon_{\text{Wall}}$) is varied.

Fig. 4.5 shows a sample P_{3D} measurement when $\varepsilon_{\text{Wall}}$ is varied. The values of $\varepsilon_{\text{Wall}}$ used are $7k_BT, 9k_BT$ and $10k_BT$ while U_0 is kept constant at $9k_BT$. A positive P_{3D} corresponds to a structure with dominant NaCl lattices while a negative P_{3D} corresponds to a structure with dominant CsCl lattices. For $P_{\text{3D}} < |0.05|$, the structure is considered
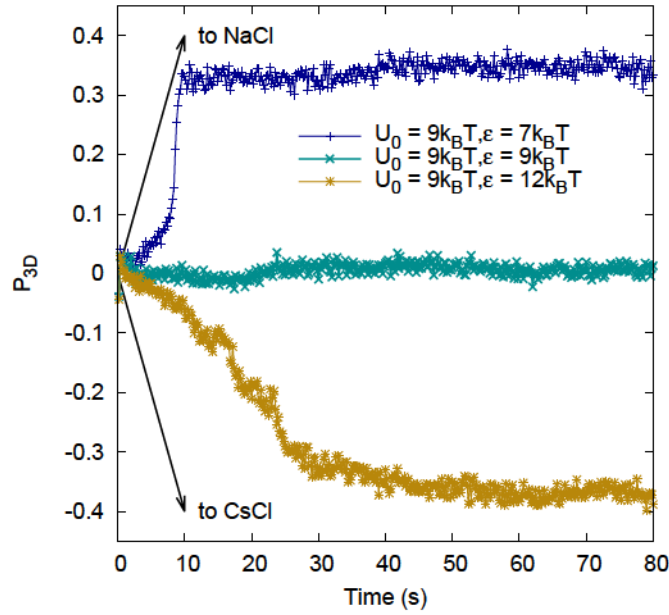
Figure 4.5:   Different structures formed on the wall with varying $\varepsilon_{\text{Wall}}$. The suspension used has $\kappa a = 2.55$ and $U_0 = 9k_BT$.

either as a mixture of both lattice types or remains disordered. It appears from Fig. 4.5 that the transformation to CsCl occurs when $\varepsilon_{\text{Wall}} > U_0$. To check this observation, the range of $\varepsilon_{\text{Wall}}$ is widened and 5-8 simulations are performed for suspensions with $U_0 = 9k_BT, \kappa a = 2.55$ and $U_0 = 7k_BT, \kappa a = 3$. The final structures are tabulated in Table 4.3. The results confirm that there is a higher probability of obtaining CsCl structures when $\varepsilon_{\text{Wall}} > U_0$. On the other hand, when $U_0 < \varepsilon_{\text{Wall}}$, the structures tend to remain as NaCl.

Between the results presented in this chapter and those of Ref. [39], it appears that process of undergoing a metastable NaCl formation can be skipped when an attractive wall is introduced. Additionally, the strength required to overcome the NaCl phase occurs when $\varepsilon_{\text{Wall}}$ is around the value of U_0.

4.4.2   Strength of the wall ($\varepsilon_{\text{Wall}}$) vs. inverse range of interaction (κa)

To see if the inverse range of interaction can also affect the structure of the colloids, an additional system with $\kappa a = 1.5$ and $U_0 = 9k_BT$ is tested against the system with $\kappa a = 2.55$ and $U_0 = 9k_BT$. The results are presented in Table 4.4. First, a similar trend, i.e. the formation of CsCl is higher when $\varepsilon_{\text{Wall}} > U_0$, is observed. However, the probability of obtaining CsCl is even higher in suspensions with $\kappa a = 1.5$ than $\kappa a = 2.55$ (compare Table 4.4 with Table 4.3) . A possible explanation for this is because the aggregation

of a bulk suspension with a longer range of repulsion ($\kappa a = 1.5$) is more difficult than the aggregation of a suspension with $\kappa a = 2.55$. Hence when the wall is introduced, the system with $\kappa a = 1.5$ is more flexible to changes.

To verify this assumption, a repulsion range of $\kappa a = 1$ is also tested and it was observed that only one colloidal layer can be formed on the surface while the remaining colloids remain unattached and behave like a fluid. Moreover, the measured P_{3D} and P_{2D} for $\kappa a = 1$ are always negative (CsCl) regardless of the value of ε_{Wall} used. Therefore the systems, in which aggregation is more difficult, are more susceptible to the restructuring induced by the wall.

Table 4.4: Different structures formed on the wall with varying ε_{Wall}. The suspension used have $U_0 = 9k_BT$ and $\kappa a = 1.5$.

ε_{Wall}	$\kappa a = 1.5$		
	NaCl	CsCl	Mixed
$7k_BT$	1	4	0
$8k_BT$	2	6	0
$9k_BT$	2	4	2
$10k_BT$	0	5	0
$12k_BT$	0	5	0
$15k_BT$	0	5	0

4.4.3 CsCl formation starts from the wall

To establish that the formation of CsCl structures is due to the nucleation occurring at the surface of the wall, the P_{3D} parameter is measured per layer. This is illustrated in Fig. 4.6. First, in the system that forms CsCl, it can be noticed that the first layer goes to the negative direction first, followed by the second layer and so on. This confirms that the nucleation starts at the bottom layers.

On the contrary, in the system that forms NaCl, there are no significant NaCl seeds formed in the first layers since the P_{3D} values simply go to the positive region at the same time. This behavior is expected because the NaCl seeds are presumed to form inside the aggregates without specific prefences for the layer if $r_z > 4a$. This can be analyzed more closely by looking at the process of NaCl formation. For this part, the CsCl component of P_{3D} is plotted and is shown in Fig. 4.7. When the strength of the wall is not sufficiently high ($\varepsilon_{Wall} = 8k_BT$ vs. $U_0 = 9k_BT$), the wall still attempts to form CsCl seeds in the first layers but these are eventually supressed by the predominant NaCl seeds in the suspension. Towards the end of the simulation, the CsCl seeds gradually disappear and the structure becomes NaCl.

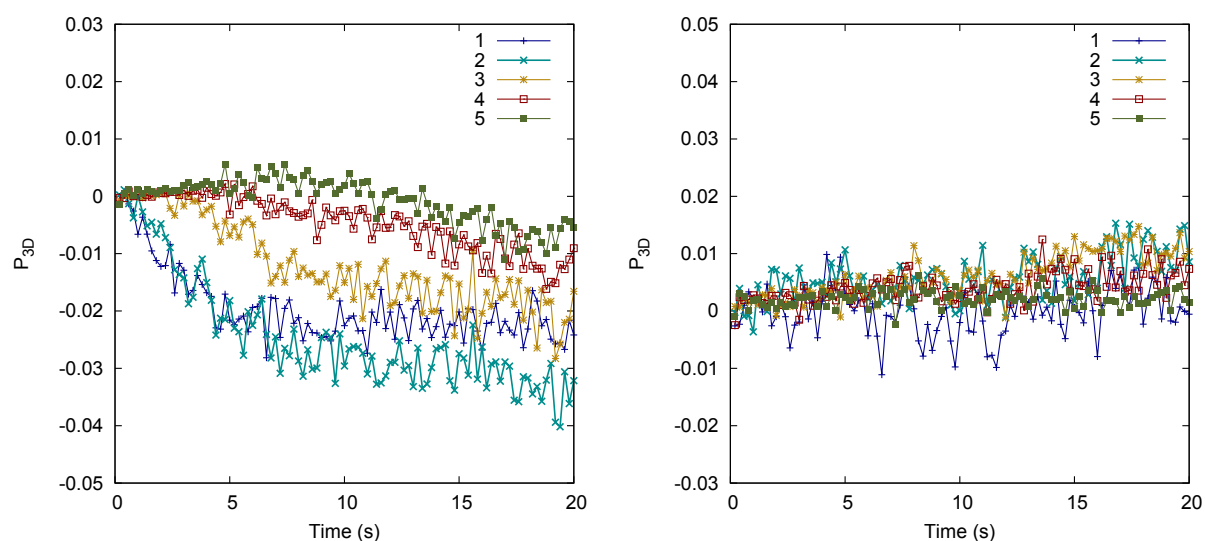Additionally, it was observed that the arrangement of the colloids on the surface of

Figure 4.6: P_{3D} parameter that is measured in the beginning of the simulation for a system that forms CsCl (left) and NaCl(right). P_{3D} is plotted layer-by-layer to show which layers form a CsCl $(-P_{3D})$ structure first.
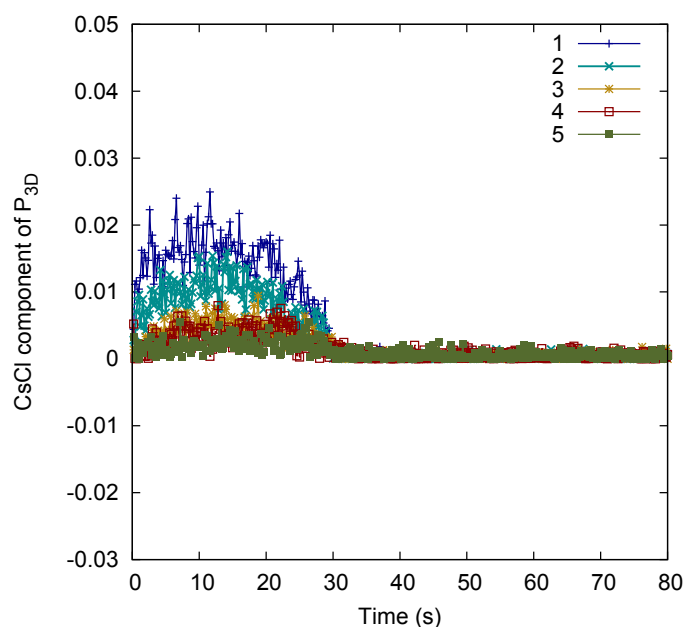

Figure 4.7: CsCl component of the P_{3D} parameter that is measured layer per layer for a system with $\varepsilon_{Wall} = 8k_BT$ and $U_0 = 9k_BT$. The final structure is NaCl. It can be observed that CsCl seeds are formed on the surface of the wall but are eventually supressed by the NaCl lattices as the time progresses.

Figure 4.8: The arrangement of first layer of colloids at the surface of the wall. The CsCl structure (left) has its (101) plane attached at the surface of the wall while the NaCl structure (right) has its (100) plane attached at the surface of the wall. The two kinds of arrangements lead to P_{2D} values of different signs.

the wall is different in the CsCl and NaCl cases. An example is shown in Fig. 4.8. To quantify the difference between the (101) CsCl planes and (100) NaCl planes, the value of P_{2D} for the first layer is calculated (see Fig. 4.9). A general trend that is present among the samples is that in the beginning of the simulation, the value of P_{2D} immediately goes to the negative region. When the structure goes to CsCl, P_{2D} remains negative (CsCl). In contrast, when the structure goes to NaCl, the first layer rearranges and P_{2D} becomes positive (NaCl).

4.4.4 Number of colloids per layer and interaction energy with the wall

After establishing that the CsCl nucleation starts from the wall, the next step is to understand why this type of formation occurs. To answer this, the following parameters are checked: (1) the number of colloids packed in the first layer; and (2) the total interaction energy between the colloids and the wall.

Table 4.5 shows the structures formed (CsCl, NaCl or Mixed) with the final number of colloids (N_s) in the first layer ($3.1 < r_z < 3.5$). It can be observed that for every well-depth, the number of colloids that can be packed in the first layer is generally larger when CsCl structures are formed.

Fig. 4.10 shows the number of colloids that can be found at different distances from the wall. This is measured at the end of the simulation ($t = 80$ s). The peaks of the histogram correspond to each of the colloidal planes parallel to the surface of the wall. From the figure, it can be discerned that the number of colloids packed in the first layer is significantly larger in the CsCl case. This is generally observed in all of the samples. Moreover, the distances between the peaks are smaller for the CsCl case suggesting a more compact and favorable ordering.
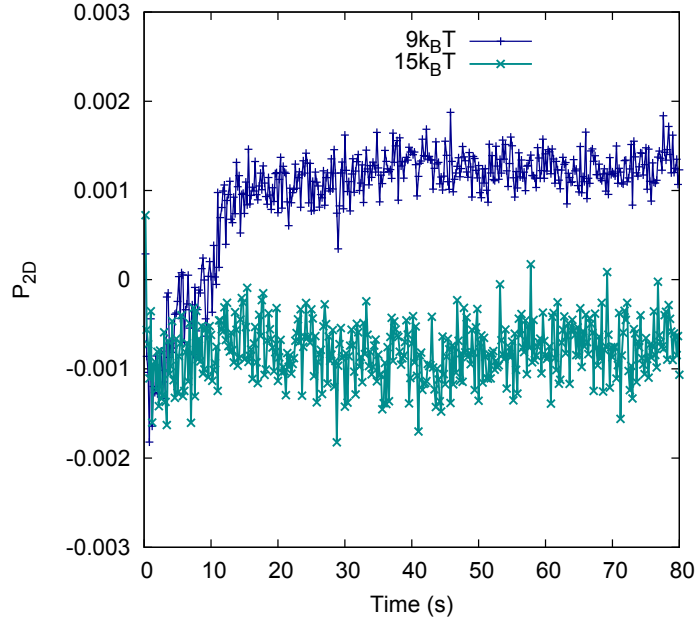
Figure 4.9: P_{2D} parameter for the system with $\kappa a = 1.5$.

Table 4.5: Final number of colloids in the first layer with the corresponding structure.

| $\kappa a = 1.5$	Sample 1	Sample 2	Sample 3	Sample 4	Sample 5
$7k_BT$	101 (CsCl)	89 (CsCl)	87 (CsCl)	89 (CsCl)	88 (CsCl)
$8k_BT$	81 (NaCl)	94 (CsCl)	88 (NaCl)	87 (NaCl)	96 (CsCl)
$9k_BT$	91 (NaCl)	94 (CsCl)	80 (Mixed)	76 (Mixed)	97 (CsCl)
$10k_BT$	90 (CsCl)	91 (CsCl)	91 (CsCl)	104 (CsCl)	99 (CsCl)
$\kappa a = 2.55$	Sample 1	Sample 2	Sample 3	Sample 4	Sample 5
$7k_BT$	93 (NaCl)	74 (NaCl)	76 (Mixed)	56 (Mixed)	76 (NaCl)
$8k_BT$	86 (NaCl)	76 (Mixed)	77 (Mixed)	73 (Mixed)	73 (Mixed)
$9k_BT$	95 (NaCl)	75 (Mixed)	87 (NaCl)	82 (Mixed)	82 (CsCl)
$10k_BT$	79 (Mixed)	96 (NaCl)	105 (CsCl)	84 (Mixed)	86 (Mixed)
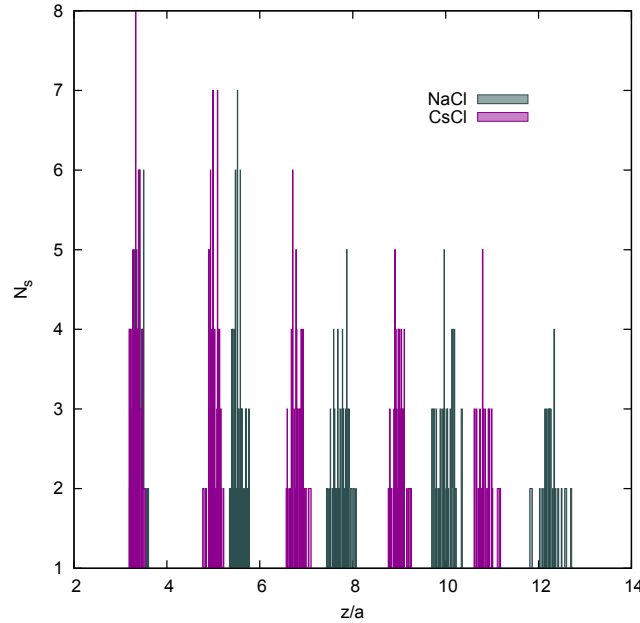
Figure 4.10:   Number of colloids vs. the distance from the wall. The peaks correspond to the planes of colloids that are parallel to the wall's surface.

Next, the total interaction energies between the colloids and the wall are compared using a suspension with $\kappa a = 1.5$ and $\kappa a = 2.55$ placed on a wall with $\varepsilon = 8 k_B T$. The results are shown in Fig. 4.12. For both systems, the simulations that yield CsCl structures have lower energies than the simulations that yield NaCl structures.

The final step is to confirm that the CsCl transformation is not induced by finite size effects. P_{3D} is measured for different lengths L of the simulation box while keeping the volume fraction constant. Fig. 4.11 shows the different side lengths L of the simulation box that are tested. The results show that the CsCl structures obtained are independent of the system size.

4.5   Shaken Aggregates

Management and control over the shape and ordering of the colloids during the aggregation process is important in the production of many chemical and pharmaceutical products [130]. For suspensions in equilibrium, several important material properties are already realized by tuning the interparticle forces between colloids [19]. By subjecting the supension to a flow, these properties can also depend on the strength of the shearing forces applied. The colloid structure under shear is primarily influenced by the balance among the interparticle forces, Brownian motion and hydrodynamics interactions (HIs) [131]. The shearing of colloidal suspensions can lead to reorientation, break-up, densification and spatial reorganization of aggregates [132]. This chapter focuses on colloidal suspensions
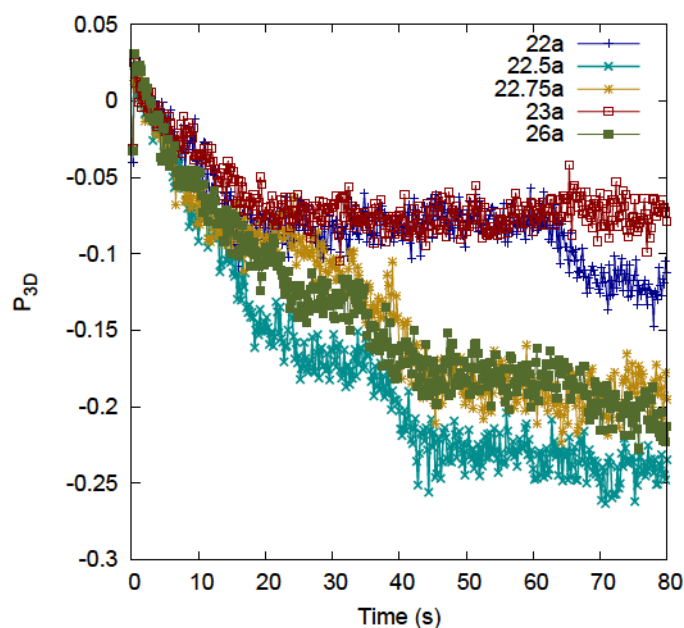
Figure 4.11:   The influence of L on the parameter P_{3D}.   The results prove that the formation of CsCl structures is not induced by finite size effects.
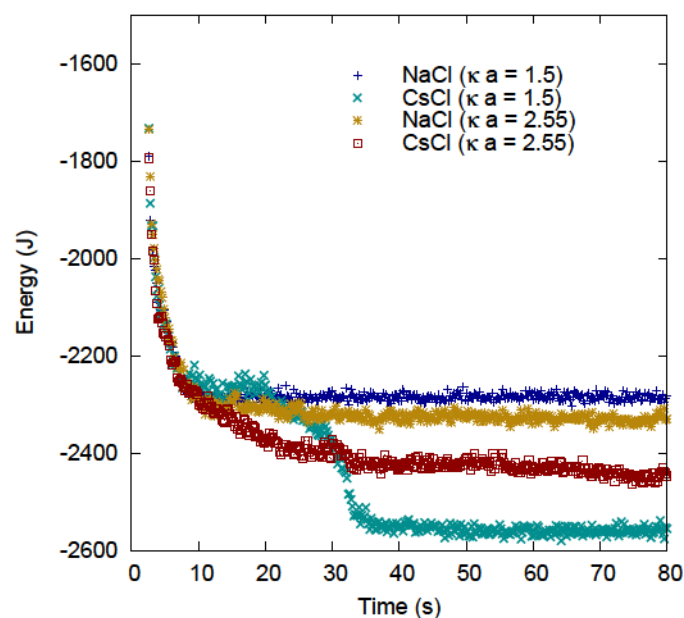

Figure 4.12:   Comparing the colloid-wall interaction energies for NaCl vs. CsCl structures. The strength of the wall used in $8k_BT$ for both $\kappa a = 1.5$ and 2.55 interaction ranges.

subjected to oscillating flow.

In the work by Penkova et al., it was experimentally observed that shear flow may strongly affect the nucleation in suspensions [120]. Morever in some systems, there is an optimal flow velocity that can lead to the fastest nucleation [120, 133]. This rationale is backed-up by Refs. [132, 134] where it was found that a small amount of shear can speed up the crystallization process of colloids and enhances the quality of the growing crystal. They also found that moderate shear rates can prevent or destroy ordering in the sytem.

However, the numerical studies mentioned above do not include a full treatment of HIs. This can be problematic since the modeling of sheared suspensions without proper HIs inclusion are known to induce colloid ordering [135]. The objective of this chapter is to model aggregates under oscillatory flows using SRD-MD. Moreover, it attempts to understand how the microstructure accomodates the applied shearing forces. The results should provide qualitative insights onto the effects of shear and HIs on the crystallization process of colloidal suspensions.

4.6 System: Modeling oscillatory flows

In Sec. 1.5.1, the way in which shear is introduced in the colloidal system is discussed. Oscillatory motion is simulated by using the following line in the LEBC:

```
dvy = DELVY * cos ( 2 * pi * totaltime * FREQ )
```

The factor `dvy` is the shear velocity, `DELVY` describes the amplitude of oscillation, while `FREQ` dictates the oscillation frequency of the system. The thermostat applied is the Monte-Carlo thermostat discussed in Sec. 1.5.2.2.

The system used is the same the system described in Chapter 3 to facilitate comparisons between the systems when the oscillating shear is removed. The colloids have a radius of $a = 255$ nm and mass of 2.76×10^{-16}. They are evolved using a DLVO potential with the secondary minimum having a well-depth of $10k_BT$. $N_c = 500$ colloids are placed in a simulation box of side length $L = 55a_0$, where $a_0 = 127.5$. The resulting volume fraction is 10%.

The shear rate is set to 10 s^{-1} and the frequency of oscillations used is 20 s^{-1}. The equilibration is the part where the system, starting from a Maxwell-Boltzmann distribution, starts receiving shearing forces until it reaches a steady state. Finding the appropriate thermostat strength c for oscillatory flow proves to be more challenging and time consuming than the one-directional flow presented in Chapter 2. It was found that the equilibration part requires a stronger thermostat strength. However it also stabilizes to a temperature lower than the required temperature ($T < 293$ K). Hence for the preliminary investigations made in this chapter, the value of c used during the equilibration part is
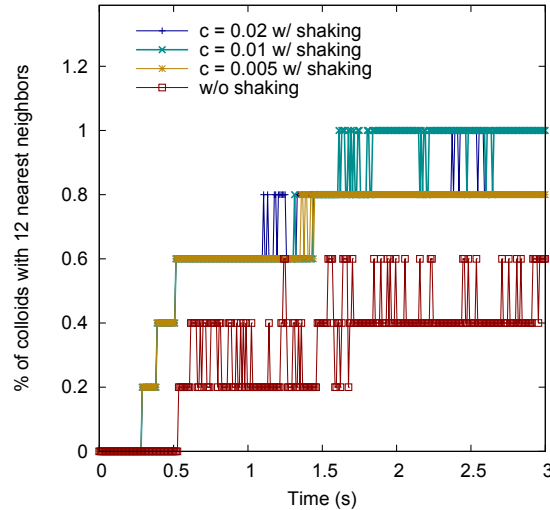
Figure 4.13:   Percentage of colloids with 12 nearest neighbors vs. time. The ordering of the shaken aggregates is generally larger than the ordering of the aggregates in equilibrium.

$c = 0.02$. Values of $c < 0.02$ are too small for the equilibration procedure and lead to anomalous behavior. Once the temperature T stabilizes, the value of c is varied. In this work, $c = 0.02, 0.01$ and 0.005 are used.

4.7   Results for Shaken Aggregates

First, the SRD-MD simulations of shaken aggregates are compared with the SRD simulations in equilibrium. The results are shown in Fig. 4.14. Despite the different temperatures in the three systems, a general trend can be observed. That is, the ordering for the shaken aggregates is larger and faster than the ordering of the aggregates in equilibrium.

Second, the SRD-MD simulations of shaken aggregates with $c = 0.02$ are compared with SRD-MD and BD simulations of aggregates in equilibrium. The results are shown in Fig. 4.13. The shaken aggregates are more ordered than its SRD-MD equilibrium counterpart while also achieving the same ordering as the BD simulations. Overall, the oscillatory flow promotes faster ordering within the aggregate.

The aggregate formation are also checked by plotting N_A vs time. This is shown in Fig. 4.15. It seems that when the aggregates undergo an oscillating shear, the cluster-cluster coalescence is slower. If we follow the same logic as in Chapter 3, i.e. the slow cluster-cluster coalescence promotes ordering within the aggregate, then the shaking may provide the colloids enough time to reorganize within the small clusters.
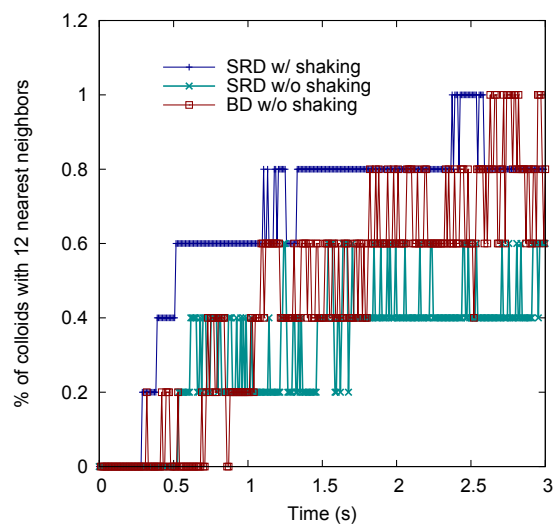
Figure 4.14: Percentage of colloids with 12 nearest neighbors vs. time for SRD and BD simulations.
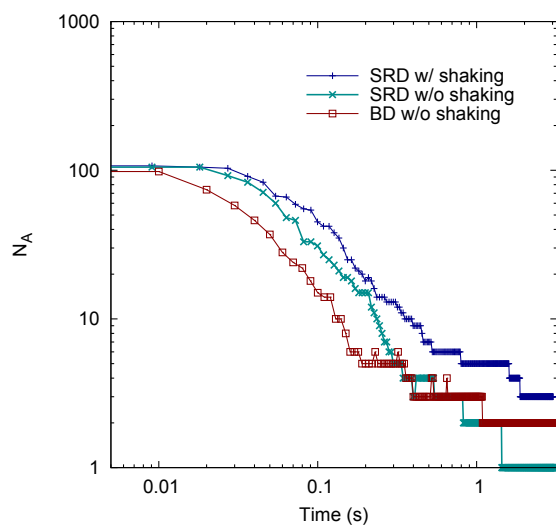

Figure 4.15: Number of Aggregates (N_A) vs time for systems with and without shaking.

4.8 Conclusions

First, this chapter has demonstrated that by using Brownian Dynamics simulations and by introducing an attractive wall to a binary system of colloids, the expected equilibrium lattice structure can be reordered. The extent of lattice transformation depends on the properties of the suspension and the characteristics of the walls. Specifically, when the strength of attraction of the wall supersedes the strength of attraction between the colloids ($\varepsilon_{\text{Wall}} > U_0$), the probability of forming a CsCl structure is higher than its metastable NaCl-counterpart. However, when $\varepsilon_{\text{Wall}} < U_0$, most aggragates are formed with NaCl structures as in the absence of the wall.

Additionally, the suspensions with $\kappa a = 1.5$ are more susceptible to change than suspensions with $\kappa a = 2.55$ and $\kappa a = 3$. This is because aggregation is more difficult for $\kappa a = 1.5$ thus making it more adaptable to the phase transformation caused by the attractive wall.

It was also observed that CsCl-seeds start forming at the bottom of the wall and slowly build up to the top most layers. CsCl formation is more favorable because it allows the colloids to be more closely packed at the surface. In addition to this, it was observed that the interaction energy, between the colloids and the walls, is also lower for CsCl structures than for NaCl structures.

From the results presented, it appears that the process of undergoing metastable NaCl formation can be skipped when a sufficiently strong wall is introduced to the original system. Moreover, for $\kappa a < 2.55$, CsCl structures would be metastable in absence of the wall.

However, it is important to note that hydrodynamic effects are ignored in this chapter for the following reasons: (1) the study serves as a preliminary analysis on the effects of attractive walls on colloids, (2) the suspensions are still relatively dilute, (3) HIs are found to be negligible in the aggregation of the bulk system presented in Ref. [39]. Nevertheless, the incorporation of HIs can serve as a possible extension on the study of colloid adsorption on surfaces.

Finally, this chapter also provides preliminary investigations concerning aggregates under oscillatory flow. It was found that in general, when aggregates are subjected to an oscillating shear, the ordering of the colloids increases. In addition to this, the rate of ordering is faster. While several tests and samplings have to be performed, we argue that the results provided can give a good qualitative insight into the effects of oscillatory flows in shaken aggregates, especially since the system requires proper HIs modeling.

A better thermostat that fits the shaken aggregates is also needed. While the Monte-Carlo thermostat can still be applied in the system presented in this chapter, finding the required c value proves to be time and memory consuming. A good extension of this work

is to generate an SRD-MD-appropriate thermostat that can accomodate different shear forces.

Conclusions

In this thesis, two of the main challenges in the computational study of colloidal suspensions are addressed: incorporation of hydrodynamic interactions (HIs) and the modeling of external constraints in the forms of shear and attractive wall.

First, the hybrid Stochastic Rotation Dynamics - Molecular Dynamics (SRD-MD) method was developed. In contrast to previous works, the method presented in this thesis was able to calculate for the shear viscosity vs. volume fraction relation of a system that resembles a hard-sphere interaction. This was achieved by implementing the Lees-Edwards boundary conditions (LEBC) for a system with an MD-type coupling. Since the addition of shear generates energy drifts, a Monte-Carlo thermostat was also employed. The steady state condition generated by the LEBC and Monte-Carlo algorithms was described by stress tensors, from which the shear viscosity was evaluated. The presented non-equilibrium approach of obtaining the shear viscosity can be applied to both dense and concentrated cases. Moreover, it can be used to analyze the components of shear viscosity and the characterization can be done in two ways: one is by examining the kinetic and collision contributions, and the other is by examining the fluid and colloid contributions. The SRD-MD results are also comparable with known numerical, experimental and theoretical data

At this stage, SRD-MD has been verified and can be used alongside Brownian Dynamics (BD) to determine the percolation threshold (ϕ_c) of alumina suspensions described by the Derjaguin-Landau-Verwey-Overbeek potential. The BD simulations successfully provided a phase-space diagram (volume fraction vs. colloid-colloid attraction strength) that gives an approximation of the region where percolation in 3 directions can be observed. Moreover, the phase-space diagram shows that ϕ_c decreases with increasing colloid-colloid attraction strength. Additional information regarding the effects of HIs on ϕ_c were found using SRD-MD. Specifically, systems with HIs tend to have more elongated structures during the aggregation process than systems without HIs. There is a significant decrease in ϕ_c when the colloid-colloid attraction is not too strong (for a well depth of $5k_BT$, $\phi_c = 10\%$ with HIs and $\phi_c = 12\%$ without HIs). On the other hand, the effects of HIs tend to become negligible when the colloid-colloid attraction increases (for a well depth of $10k_BT$, $\phi_c = 8\%$ with or without HIs). These observations have also huge implications in solving the problem of long computation times that are often required in modeling percolating systems. A good indicator for determining the most appropriate simulation technique is the colloid-colloid attraction strength. For systems with attraction strengths greater than $10k_BT$, the rearrangement process is very slow hence BD should suffice. In contrast, for systems with attraction strengths less than $10k_BT$, SRD-MD is among the fastest approach available that can properly account for HIs. The ϕ_c values calculated in this thesis are in also in good agreement with those estimated by the yield stress model (YODEL) by Flatt and Bowen. This work can be useful, alongside YODEL,

in predicting the yield stress magnitude of ceramic materials.

Another type of external force introduced in this thesis is in the form of an attractive wall. A binary system of colloids described by the Yukawa potential was placed in a simulation box with one attractive surface and is modeled using BD. The behaviour of the binary system in equilibrium is already known from previous studies: for suspensions with a well depth of $9k_BT$, NaCl-type lattices are energetically stable when $\kappa a < 2.55$, where κa describes the inverse range of interaction; and CsCl-type lattices are energetically stable when $\kappa a > 2.55$. This behaviour is altered with the introduction of the wall. It was established that when the wall's attraction strength surpasses the colloid-colloid attraction strength, the NaCl lattices tend to transform to CsCl. The probability of this lattice modification is even higher as the attraction strength of the wall increases. Aside from the wall's attraction strength, the effect of changing the value of κa was also investigated. The results show that smaller values of κa, e.g. $\kappa a = 1.5$ and 1, are more susceptible to lattice changes than higher values of κa, e.g. $\kappa a = 3$ and 2.55. This is because aggregation is more difficult to achieve for $\kappa a \leq 1.5$. By looking at the final structures, it can be seen that the CsCl lattice formation is more favored when the wall is sufficiently strong because it allows for a more compact configuration. In addition to this, it was found that the total energy between the wall and the structure is also lower for the CsCl case than the NaCl case.

Finally, preliminary investigations on shaken suspensions by SRD-MD were conducted. The $10k_BT$-case alumina system, which does not attain proper reorganization, was placed under an oscillating shear with a rate of 10 s^{-1} and a frequency of 20 s^{-1}. This is to check if the ordering of the structure improves. The results show that the suspensions undergoing oscillatory motion reorganize at a faster rate than the suspensions in equilibrium. This technique of agitating the suspension can have a high potential in promoting crystallization and requires a more in-depth study.

Bibliography

Bibliography

[1] T. Ihle and D. M. Kroll, *Phys. Rev. E.*, vol. 67, p. 066705, 2003.

[2] N. Kikuchi, M. Pooley, J. F. Ryder, and J. M. Yeomans, *J. Chem. Phys.*, vol. 119, p. 6388, 2003.

[3] D. R. Foss and J. F. Brady, *J. Rheology*, vol. 44, p. 629, 2000.

[4] J. M. Koelman and P. J. Hoogerbrugge, *Europhys. Lett.*, vol. 21, pp. 363–368, 1993.

[5] P. J. Hoogerbrugge and J. M. V. A. Koelman, *Europhys. Lett.*, vol. 19, pp. 155–160, 1992.

[6] P. N. Segrè, S. P. Meeker, P. N. Pusey, and W. C. K. Poon, *Phys. Rev. Lett.*, vol. 75, no. 5, p. 958, 1995.

[7] J. van der Werff and C. de Kruif, *J. Rheology*, vol. 33, p. 421, 1989.

[8] I. M. Krieger and T. J. Dougherty, *Trans. Soc. Rheol. III*, vol. 1959, p. 137, 1959.

[9] A. Einstein, *Ann. Phys.*, vol. 19, p. 289, 1906.

[10] ——, *Ann. Phys.*, vol. 34, p. 591, 1911.

[11] O. O. Omatete, M. A. Janney, and R. A. Strehlow, *Am. Ceram. Soc. Bull.*, vol. 70, pp. 1641–1649, 1991.

[12] M. Agarwala, A. Bandyopadhyay, and R. van Weerwn, *Am. Ceram. Soc. Bull.*, vol. 75, pp. 60–66, 1996.

[13] J. Cesarano, R. Segalman, and P. Calvert, *Ceram. Ind.*, pp. 94–102, 1998.

[14] M. L. Griffith and J. W. Halloran, *J. Am. Ceram. Soc*, vol. 79, pp. 2601–2608, 1996.

[15] E. Sachs, M. Cima, and P. Williams, *J. Eng. Ind.*, vol. 114, pp. 481–488, 1992.

[16] M. E. Leunissen, C. Christova, A. P. Hynninen, C. P. Royall, A. I. Campbell, A. Imhof, M. Dijkstra, R. van Roij, and A. van Blaaderen, *Nature*, vol. 437, p. 235, 2005.

[17] B. V. Derjaguin and L. D. Landau, *Acta Physicochim. URSS*, vol. 14, p. 63352, 1941.

[18] E. . J. W. Verwey and J. T. G. Overbeek, *Theory of Stability of Lyophobic Colloids*. The Netherlands: Elsevier, 1948.

[19] J. A. Lewis, *J. Am. Ceram. Soc.*, vol. 83, pp. 2341–59, 2000.

Bibliography

[20] C. N. Likos, *Physics Reports*, vol. 348, pp. 267–439, 2001.

[21] M. Stuer and P. Bowen, *Adv. Appl. Ceramics*, vol. 11, pp. 254–261, 2012.

[22] R. Flatt and P. Bowen, *J. Am. Cream. Soc.*, vol. 89, pp. 1244–1256, 2006.

[23] P. Lu, E. Zaccarelli, F. Ciulla, A. Schofield, F. Sciortino, and D. A. Weitz, *Nature*, vol. 453, pp. 499–503, 2008.

[24] B. D'unweg and A. J. C. Ladd, *Advance computer simulation approaches for soft matter sciences III*, 1st ed. Berlin: Springer, 2009, vol. 3, ch. 2, pp. 90–166.

[25] A. Malevanets and R. Kapral, *J. Chem. Phys.*, vol. 1999, p. 8605, 110.

[26] M. Stuer, Z. Zhao, U. Aschauer, and P. Bowen, *J. Eur. Ceram. Soc.*, vol. 30, pp. 1335–1343, 2010.

[27] M. P. Allen and D. J. Tildesley, *Classical Mechanics 2nd ed.* Oxford UK: Addison Wesley, 1980.

[28] Y. Li, Y. Huo, and Y. Zhang, *Colloid Polym. Sci.*, pp. 1–9, 2015.

[29] G. Gompper, T. Ihle, D. M. Kroll, and R. G. Winkler, *Advance computer simulation approaches for soft matter sciences III*, 1st ed. Berlin: Springer, 2009, vol. 3, ch. 1, pp. 1–88.

[30] J. T. Padding and A. A. Louis, *Phys. Rev. E.*, vol. 74, p. 031402, 2006.

[31] M. Hecht, J. Harting, M. Bier, J. Reinshagen, and H. Herrmann, *Phys. Rev. E.*, vol. 74, p. 021403, 2006.

[32] C. Holm and K. Kremer, Eds., *Advance computer simulation approaches for soft matter sciences III*, 1st ed. Berlin: Springer, 2009, vol. 3.

[33] B. J. Alder and T. E. Wainwright, *J. Chem. Phys.*, vol. 31, p. 459, 1959.

[34] ——, *J. Chem. Phys.*, vol. 33, p. 1439, 1960.

[35] B. J. Alder, D. M. Gass, and T. E. Wainwright, *J. Chem. Phys.*, vol. 53, p. 3813, 1970.

[36] D. L. Ermak and A. J. McCammon, *J. Chem. Phys.*, vol. 69, pp. 1352–1360, 1978.

[37] M. Cerbelaud, A. Videcoq, P. Abélard, C. Pagnoux, F. Rossignol, and R. Ferrando, *Langmuir*, vol. 24, pp. 3001–3008, 2008.

[38] M. A. Piechowiak, A. Videcoq, R. Ferrando, D. Bochicchio, C. Pagnoux, and F. Rossignol, *Phys. Chem. Chem. Phys.*, vol. 14, pp. 1431–1439, 2012.

[39] D. Bochicchio, A. Videcoq, and R. Ferrrando, *Phys. Rev. E.*, vol. 87, p. 022304, 2013.

[40] J. Rotne and S. Prager, *J. Chem. Phys.*, vol. 50, p. 4831, 1969.

[41] H. Yamakawa, *J. Chem. Phys.*, vol. 53, pp. 436–443, 1970.

[42] V. Pryamitsyn and V. Ganesan, *J. Chem. Phys.*, vol. 122, p. 104906, 2005.

[43] P. Espaňol and P. Warren, *Euro. Phys. Lett.*, vol. 30, pp. 191–196, 1995.

[44] J. E. Broadwell, *J. Fluid Mech.*, vol. 19, pp. 401–414, 1964.

[45] S. Chen and G. D. Doolen, *Annu. Rev. Fluid Mech.*, vol. 30, pp. 329–364, 1998.

[46] S. Ollila, C. Denniston, M. Karttunen, and T. Ala-Nissila, *J. Chem. Phys.*, vol. 134, p. 064902, 2011.

[47] A. J. C. Ladd, *J. Fluid Mech*, vol. 271, p. 285, 1994.

[48] A. Malevanets and R. Kapral, *J. Chem. Phys.*, vol. 112, p. 7260, 2000.

[49] R. Kapral, *Adv. Chem. Phys.*, vol. 140, p. 89, 2008.

[50] R. G. Winkler and C. C. Huang, *J. Chem. Phys.*, vol. 130, p. 074907, 2009.

[51] H. Goldstein, C. Poole, and J. Safko, *Classical Mechanics.* Oxford UK: Oxford University Press, 1987.

[52] C. C. Huang, A. Chatterji, G. Sutmann, G. Gompper, and R. G. Winkler, *J. Comp. Phys.*, vol. 229, pp. 168–177, 2010.

[53] A. Nikoubashman, N. A. Mahynski, A. H. Pirayandeh, and A. Z. Panagiotopoulos, *J. Chem. Phys.*, vol. 140, p. 094903, 2014.

[54] H. Löwen, *Phys. Rev. E.*, vol. 53, p. R29, 1996.

[55] E. Allahyarov and G. Gommper, *Phys. Rev. E.*, vol. 66, p. 036702, 2002.

[56] A. Lamura, G. Gommper, T. Ihle, and D. M. Kroll, *Europhys. Lett.*, vol. 73, p. 664, 2001.

[57] J. K. Whitmer and E. Luijten, *J. Phys.: Condens. Matt.*, vol. 22, p. 104106, 2010.

[58] A. W. Lees and S. F. Edwards, *J. Phys. C: Solid State Phys.*, vol. 5, pp. 1921–1929, 1972.

[59] P. H. Hünenberger, *Adv. Polym. Sci.*, vol. 173, pp. 105–149, 2005.

[60] H. C. Andersen, *J. Chem. Phys.*, vol. 72, pp. 2384–2393, 1980.

[61] S. Nosé, *J. Chem. Phys.*, vol. 81, p. 511, 1984.

[62] W. G. Hoover, D. J. Evans, R. B. Hickman, A. J. C. Ladd, W. T. Ashurst, and B. Moran, *Physical Review A*, vol. 22, pp. 1690–1697, 1980.

[63] A. Tomilov, A. Videcoq, T. Chartier, T. Ala-Nissilä, and I. Vattulainen, *J. Chem. Phys.*, vol. 137, p. 014503, 2012.

[64] D. M. Heyes, *Chem. Phys.*, vol. 82, pp. 285–301, 1983.

[65] M. Hecht, J. Harting, T. Ihle, and H. Herrmann, *Phys. Rev. E.*, vol. 72, p. 011408, 2005.

[66] H. Noguchi and G. Gompper, *Phys. Rev. E*, vol. 78, p. 016706, 2008.

[67] C. M. Pooley and J. M. Yeomans, *J. Phys. Chem. B*, vol. 109, p. 65015, 2005.

[68] G. Batôt, V. Dahirel, G. Mériguet, A. Louis, and M. Jardat, *Phys. Rev. E.*, vol. 88, p. 043304, 2013.

[69] J. K. Whitmer and E. Luijten, *J. Phys.: Condens. Matter*, vol. 22, p. 104106, 2010.

[70] A. A. Louis, E. Allahyarov, H. Löwen, and R. Roth, *Phys. Rev. E.*, vol. 65, p. 061407, 2002.

[71] J. M. Brader, *J. Phys.*, vol. 22, p. 363101, 2010.

[72] D. B. Genovese, *Advances in Colloid and Interface Science*, vol. 171-172, pp. 1–16, 2012.

[73] R. A. Lionberger and W. B. Russel, *J. Chem. Phys.*, vol. 106, p. 402, 1997.

[74] G. K. Batchelor and J. Green, *J. Fluid Mech.*, vol. 56, p. 401, 1972.

[75] A. Tomilov, A. Videcoq, M. Cerbelaud, M. A. Piechowiak, T. Chartier, T. Ala-Nissilä, D. Bochicchio, and R. Ferrando, *J. Phys. Chem. B*, vol. 117, p. 14509, 2013.

[76] M. S. Green, *J. Chem. Phys.*, vol. 22, p. 398, 1954.

[77] R. Kubo, *J. Phys. Soc. Japan*, vol. 12, pp. 570–586, 1957.

[78] H. Mori, *Prog. Theor. Phys.*, vol. 33, p. 423, 1965.

[79] ——, *Prog. Theor. Phys.*, vol. 34, p. 399, 1965.

[80] R. Zwanzig, *Lectures in Theoretical Physics.* New York: Wiley, 1961, vol. 3.

[81] S. Mueller, E. W. Llewellin, and H. M. Mader, *Proc. R. Soc. A.*, vol. 466, pp. 1201–1228, 2010.

[82] D. G. Thomas, *J. Colloid Sci.*, vol. 20, pp. 267–277, 1965.

[83] I. R. Rutgers, *Rheol. Acta*, vol. 2, pp. 202–210, 1962.

[84] ——, *Rheol. Acta*, vol. 2, pp. 305–348, 1962.

[85] E. Guth and O. Gold, *Phys. Rev.*, vol. 53, p. 322, 1938.

[86] V. Vand, *J. Phys. Colloid Chem.*, vol. 52, pp. 277–299, 1948.

[87] R. S. J. Manley and S. G. Mason, *Can J. Chem.*, vol. 33, pp. 733–763, 1955.

[88] J. T. Padding and A. A. Louis, *Phys. Rev. Lett.*, vol. 93, p. 220601, 2004.

[89] W. K. Poon, E. R. Weeks, and C. P. Royall, *Soft Matter*, vol. 8, pp. 21–30, 2012.

[90] A. Laganapan, A. Videcoq, M. Bienia, T. Ala-Nissila, D. Bochicchio, and R. Ferrando, *J. Chem. Phys.*, vol. 142, p. 144101, 2015.

[91] D. M. Heyes and J. R. Melrose, *J. Non-Newtonian Fluid Mech.*, vol. 46, pp. 1–28, 1993.

[92] J. F. Brady and J. F. Morris, *J. Fluid Mech.*, vol. 348, pp. 103–139, 1997.

[93] D. Quemada and C. Berli, *Adv. Colloid and Interface Sci.*, vol. 98, pp. 51–85, 2002.

[94] F. Y. Castillo, R. Socher, B. Krause, R. Headrick, B. P. Grady, R. Prada-Silvy, and P. Pötschke, *Polymer*, vol. 52, pp. 3835–3845, 2011.

[95] A. Coniglio, L. D. Arcangelis, E. D. Gado, A. Fierro, and N. Sator, *J. Phys.: Condens. Matt.*, vol. 16, pp. 4831–4839, 2004.

[96] M. E. Helgeson, Y. Gao, S. E. Moran, J. Lee, M. Godfrin, A. Tripathi, A. Bose, and P. S. Doyle, *Soft Matter*, vol. 17, pp. 3122–33, 2014.

[97] J. Bergenholtz and M. Fuchs, *Phys. Rev. E.*, vol. 59, pp. 5706–5715, 1999.

[98] A. Coniglio, J. J. Arenzon, A. Fierro, and M. Sellito, *Eur. Phys. J. Special Topics*, vol. 223, pp. 2297–2306, 2014.

[99] S. R. Broadbent and J. M. Hammersley, *Proc. Camb. Philos. Soc.*, vol. 53, pp. 629–641, 1957.

[100] Z. Zhou, M. J. Solomon, P. J. Scales, and D. V. Boger, *J. Rheology*, vol. 43, pp. 651–671, 1999.

[101] I. Lesov, S. Tcholakova, and N. Denkov, *J. Colloid and Interface Science*, vol. 426, pp. 9–21, 2014.

[102] R. M. Guillermic, A. Salonen, J. Emile, and A. Saint-Jalmes, *Soft Matter*, vol. 5, pp. 4975–4982, 2009.

[103] M. Strauss, T. Ring, A. Bleier, and H. K. Bowen, *J. App. Phys.*, vol. 58, p. 3871, 1985.

[104] P. C. Kapur, P. J. Scales, D. V. Boger, and T. W. Healy, *AIChe. J.*, vol. 43, pp. 1171–1179, 1997.

[105] P. J. Scales, T. W. H. S. B. Johnson, and P. C. Kapur, *AIChe. J.*, vol. 44, pp. 538–544, 1998.

[106] A. Moncho-Jordá, A. A. Louis, and J. T. Padding, *Phys. Rev. Lett.*, vol. 104, p. 068301, 2010.

[107] H. Tanaka and T. Araki, *Phys. Rev. Lett.*, vol. 85, pp. 1338–1341, 2000.

[108] I. M. Jánosi, T. Tél, D. E. Wolf, and J. A. C. Gallas, *Phys. Rev. E.*, vol. 56, pp. 2858–2867, 1997.

[109] R. Yamamoto, K. Kim, Y. Nakayama, K. Miyazaki, and D. Reichman, *J. Phys. Soc. Japan*, vol. 77, p. 084804, 2008.

[110] J. Whitmer and E. Luijten, *J. Phys. Chem. B*, vol. 115, pp. 7294–7300, 2011.

[111] A. Laganapan, M. Mouas, A. Videcoq, M. Cerbelaud, M. Bienia, P. Bowen, and R. Ferrando, *J. Colloids and Interface Science*, vol. 458, pp. 241–246, 2015.

[112] L. Bergström, *Adv. Colloid Interface Sci*, vol. 70, p. 125, 1997.

[113] D. Bochicchio, A. Videcoq, A. R. Studart, and R. Ferrrando, *J. Colloid Interface Sci.*, vol. 440, pp. 198–203, 2015.

[114] M. Cerbelaud, R. Ferrando, and A. Videcoq, *J. Chem. Phys.*, vol. 132, p. 084701, 2010.

[115] A. Larsen and D. Grier, *Nature*, vol. 385, pp. 230–233, 1997.

[116] M. Buerger, *Phase Transformations in Solids.* New York: Wiley, 1951.

[117] D. Zahn, O. Hochrein, and S. Leoni, *Phys. Rev. B*, vol. 72, p. 094106, 2005.

[118] P. Gonzáles-Mozuelos, M. Medina-Noyola, B. D'Aguanno, J. M. Méndez-Alcaraz, and R. Klein, *J. Chem. Phys.*, vol. 95, p. 3, 1991.

[119] M. Oberholzer, N. J. Wagner, and A. M. Lenhoff, *J. Chem. Phys.*, vol. 107, p. 9157, 1997.

[120] A. Penkova, W. Pan, F. Hodjaoglu, and P. G. Vekilov, *Ann. N. Y. Acad. Sci.*, vol. 214, p. 1077, 2006.

[121] A. Yethiraj and A. A. van Blaaderen, *Nature*, vol. 421, pp. 513–517, 2003.

[122] W. K. Kegel and A. van Blaaderen, *Science*, vol. 287, pp. 290–293, 2000.

[123] M. Malmsten, *J. Colloid and Interface Sci.*, vol. 207, pp. 186–199, 1998.

[124] C. A. Haynes and W. Norde, *Colloids Surf.*, vol. 2, p. 517, 1994.

[125] Y. F. Missirlis and W. Lemm, *Modern Aspects of Protein Adsorption on Biomaterials.* Boston: Kluwer Academic, 1991.

[126] K. P. Velikov, C. G. Christova, R. P. A. Dullens, and A. van Blaanderen, *Science*, vol. 296, pp. 106–109, 2002.

[127] E. C. M. Vermolen, A. Kuijk, L. C. Filion, M. Hermes, J. H. J. Thijssen, M. Dijkstra, and A. van Blaaderen, *Proc Natl Acad Sci U S A*, vol. 106, pp. 16 063–16 067, 2009.

[128] D. Bochicchio, A. Videcoq, and R. Ferrrando, *J. Chem. Phys.*, vol. 140, p. 024911, 2014.

[129] D. van der Spoel, E. Lindahl, B. Hess, G. Groenhof, A. E. Mark, and H. J. C. Berendsen, *J. Comput. Chem*, vol. 26, p. 1701, 2005.

[130] D. Li and R. B. Kaner, *J. Am. Chem. Soc.*, vol. 128, pp. 968–975, 2005.

[131] J. Vermant and M. J. Solomon, *J. Phys.: Condens. Matter*, vol. 17, pp. R187–R216, 2005.

[132] J. J. Cerdà, T. Cintes, C. Holm, C. M. Sorensen, and A. Chakrabali, *Phys. Rev. E.*, vol. 78, p. 031403, 2008.

[133] P. Vekilov, B. R. Thomas, and F. Rosenberger, *J. Phys. Chem.*, vol. 102, pp. 5208–5216, 1998.

[134] A. Mokshin and J. L. Barrat, *Phys. Rev. E.*, vol. 82, p. 021505, 2010.

[135] J. F. Brady, *Chem. Eng. Sci.*, vol. 56, pp. 2921–2926, 2001.